A Validation Infrastructure for Non-Ideal Compressible Fluid Dynamics

with applications to ORC Turbines

Riccardo Vello

TU Delft

A Validation Infrastructure for Non-Ideal Compressible Fluid Dynamics

with applications to ORC Turbines

by

Riccardo Vello

to obtain the degree of Master of Science
at the Delft University of Technology,
to be defended publicly on 28 May 2021 at 09:00.

Student number:	4560353	
Project duration:	August 31, 2020 – May 10, 2021	
Thesis committee:	Professor P. Colonna,	TU Delft, Chair
	Assistant Prof. R. P. Dwight,	TU Delft, Examiner
	Assistant Prof. M. Pini,	TU Delft, Responsible supervisor
	A. J. Head,	TU Delft, Daily Supervisor

This thesis is confidential and cannot be made public until 1 May 2024.

An electronic version of this thesis is available at `http://repository.tudelft.nl/`.

TU Delft

Abstract

The objective of this thesis was to further the validation effort on the SU2 flow solver for non-ideal compressible flows. To do so, an uncertainty quantification infrastructure based on the V&V20 validation standard was developed. To determine whether a model error was present, the different sources of uncertainty were combined and then compared to the error between the SU2 simulations and the experiments. A variety of paradigmatic test cases were proposed which, together, would constitute a robust validation of the SU2 flow solver. Two paradigmatic unit test cases were analyzed; namely, a supersonic inviscid flow and a Mach 2.0 flow over a 2.5 degree wedge. The operating conditions of the experiments were as follows: an inlet total temperature and pressure of $T_0 = 252°C$ and $P_0 = 18.4$ bara, and a back pressure of $P_{out} = 2.1$ bara, for the first case, and $T_0 = 180°C$, $P_0 = 3.5$ bara and $P_{out} = 1.0$ bara, for the second. The solver is able to predict the shock wave angle accurately. This step towards the validation was successful because the calculated total expanded uncertainty of 1.79% is higher the comparison error of 0.57%.

In the second part of the thesis, the uncertainty quantification infrastructure was adapted to a test case constituted by more complicated flow features; namely, a supersonic flow through a 5-channel blade row. The computed uncertainties were on the same order of magnitude as in the supersonic inviscid flow test case. The simulations were verified with state-of-the-art CFD software for the quantities pressure and the Mach number. The positive result of the validation represents a step forward in the validation of the flow solver for non-ideal turbomachinery cases. The adaptation of the infrastructure to the cascade blade row paves the way for complex cases and for system response quantities of interest in industrial applications of CFD software, such as efficiency, to be assessed.

Title image: Visualisation of the Mach field in a supersonic cascade blade row with Siloxane MM, generated with SU2. In the red coloured region the flow is supersonic. The dark red lines represent the expansion waves which propagate and are reflected at the walls. The yellow lines are the wakes generated by each airfoil.

Acknowledgements

I would like to first thank the members of my thesis committee for taking the time to assess my work. I would like to thank Matteo Pini for his input to upgrade my report. Secondly, Adam Head, my daily supervisor, for all his time and suggestions for improvement.

In addition, I would like to thank my family for keeping in touch from far away in the last two years. Finally my most heartfelt thanks to Uthra, who provided stimulating discussions as well as happy distractions to rest my mind outside of my research.

Riccardo Vello
Delft, May 2021

Contents

List of Figures

List of Tables

Glossary

Acronyms

ASME American Society Of Mechanical Engineers. 17, 30
CFD Computational Fluid Dynamics. 1, 15, 59
CLOWT Closed Loop Organic Wind Tunnel. 20
DRQ Direct Response Quantities. 41
EOS Equation Of State. 38, 75
IPRSV Improved Peng-Robinson EoS Modified By Stryjek And Vera. 13, 23, 38, 75
JANNAF Joint Army Navy NASA And Air Force. 14
JST Jameson-Schmidt-Turkel. 24, 41
MM Hexamethyldisiloxane. 2, 5
MUSCL Monotonic Upstream-centered Scheme For Conservation Laws. 24
NICFD Non-ideal Compressible Fluid Dynamics. 1, 5, 23
NPARC National Project For Application-oriented Research In CFD. 17, 35
ORC Organic Rankine Cycle. 1, 5
ORCHID Organic Rankine Cycle Hybrid Integrated Device. 2, 20
PDF Probability Distribution Function. 19
PRSV Peng-Robinson EoS Modified By Stryjek And Vera. 13
RANS Reynolds-Averaged Navier-Stokes. 16, 23, 41
RMS Root Mean Square. 39, 63
SA Spalart–Allmaras Turbulence Model. 16
SC Stochastic Collocation. 31, 32, 46
SRQ System Response Quantities. 59
SST Menter's Shear Stress Transport Turbulence Model. 16
SU2 SU2 Multiphysics Simulation And Design Software. 1, 12, 23, 36
TROVA Test-Rig For Organic VApours. 2, 20
UQ Uncertainty Quantification. 2, 32, 41
VBD Variance Based Decomposition. 32
VR Volumetric Flow Ratio. 29

Notation

Speed of sound	c	[m/s].	9
Isobaric heat capacity	C_p	[kJ /kg.K].	14
Comparison error	E	[-].	18
Body force	f	[N].	15
Enthalpy	h	[kJ/kg].	10
Thermal conductivity	k	[-].	15
Molecular mass	MW	[kg/mol].	5
Mach number	M	[-].	9
Pressure	p	[Pa].	6, 13
Heat flux density	q	[-].	15
Universal gas constant	R_u	[J /K.mol].	13
Temperature	T	[C].	6, 13, 14
Specific volume	v	[m^3/kg].	6
Velocity component	u	[m/s].	9, 15
Velocity	$\vec{U}$	[m/s].	23
Compressibility factor	Z	[-].	6, 7
Molar helmholtz energy	a	[kJ/kg].	14
Specific gas constant	R	[J /kg.K].	6, 14

Reduced pressure	p_r	[-].	6
Reduced temperature	T_r	[-].	6, 13
Molar volume	V_m	[m^3/mol].	13
True value	T	[-].	18
Experimental value	D	[-].	18
Simulation value	S	[-].	18
Shock wave angle	β	[deg].	11
Isothermal compressibility	β_T	[-].	8
Ideal specific heat ratio	γ	[-].	8
Polytropic exponent	γ_{PV}	[-].	8
Thermodynamic constant	κ	[-].	13
Fundamental derivative	Γ	[-].	8
Flow turning angle	θ	[deg].	11
Shear stress	τ	[kg/(m s^2)].	15
Density	ρ	[kg/m^3].	14
Expansion angle	μ	[deg].	12
Viscosity	μ^v	[kg/(m s)].	15
Acentric factor	ω	[-].	6, 13
Density ratio	ν	[-].	87

Subscripts

Critical	cr	13	**Property before shock**	1	10
Directional index	i	15	**Property after shock**	2	10
Directional index 2	j	15	**Normal component**	n	11
Saturation	sat	6	**X-component**	x	15

1 Introduction

The energy needs in modern society are rapidly growing. In the last 50 years, technologies such as gas turbines have reached very high efficiency levels. However, the pace of improvement has slowed down in recent years due to the maturity of the technology which makes further increases in performance more difficult to achieve. Moreover, the stringent regulations in term of greenhouse gases require the emissions of all power plants to decrease further in the coming decades. This means that a look at new technologies which can lead to an increased energy conversion efficiency, and lower emissions output, is needed.

Novel systems are being studied which would allow to harvest waste heat from sources currently inaccessible by combining them with existing technologies. These systems, for the power output range of interest, usually limited to a few MW_e, are practical only when using organic fluids. These components often operate in the domain of non-ideal compressible fluid dynamics (NICFD), where the ideal gas law is no longer accurate [18]. Despite the wealth of scientific knowledge in this area, the number of facilities dedicated to the assessment of computational fluid dynamics (CFD) tools is scarce. For this reason software, such as the SU2 multiphysics simulation and design software (SU2), are still not validated to simulate flows in this domain. This represents a strong limitation to designing and optimizing components such as heat exchangers and turbines. These issues need to be overcome before widespread adoption of this technology can be achieved.

1.1. Motivation

In this context, the organic Rankine cycle (ORC) is a viable way to harvest wasted energy. This process is a Rankine cycle in which an organic molecule is used as the working fluid. The advantage is due to the different molecular properties, such as the higher molar mass with respect to water, which allows the organic fluid to be chosen specifically for a given source and output temperature. For instance, the cycle can be adapted to extract power from low temperature industrial waste heat where the use of water would be unpractical. These sources are important to consider because they make up a large portion of the industrial energy waste. Another potential use are mini-ORCs, which would be able to extract power from the high temperature exhaust of various engines. From a thermodynamic point of view, using organic fluids allow for one more degree of freedom in the design of a power cycle in the form of the molecule related properties, as described by Colonna et al. [18].

The realization of mini-ORCs turbines, in the order of tens of kW of power delivered, is challenging given the low mass flow rate which, for instance, leads to high heat losses [20]. This could be overcome with properly validated tools to be used for rapid prototyping and virtual testing which would lead to a faster maturity of the technology [57]. Currently, there exists an extended literature spanning 100 years on the performance of turbomachinery components operating with air and other commonly used fluids, such as steam [22, 48]. This empirical knowledge was used to validate CFD flow solvers so that now there is a high confidence that a simulation will correctly predict the flow in the real machine. This knowledge is missing for turbomachinery operating with organic fluids in non-ideal conditions. This represents an important limitation to the design capabilities since the simulations cannot yet be trusted to be accurate. It is then necessary to validate and calibrate more complicated models before the predictions made by the solver can be considered accurate.

An increasingly used flow solver for NICFD computations is the open-source SU2 software [53]. It is a CFD tool currently being developed by several universities. One of the most active teams working on it is the

Propulsion and Power group at TU Delft, where, in particular, the assessment of NICFD flows is ongoing. The number of facilities which can provide experimental data on organic fluids are limited. Currently the state-of-the-art facility is the organic Rankine cycle hybrid integrated device (ORCHID) which was commissioned specifically to address this issue. It operates with hexamethyldisiloxane (MM), a non-toxic organosilicon, which during supersonic expansions operate in the NICFD regime. The results will then be used to validate the flow solver of SU2.

1.2. Knowledge Gap

The validation for simulations of flow operating in the NICFD regime was started only recently for SU2. Until 2015 no facility dedicated for this purpose was available. Since then, several have been built. Some initial evaluations of the solver accuracy were done at the Test-Rig for Organic VApours (TROVA) in Milan Polytechnic [28], but not at the level required to be considered a validation according to the ASME V&V Standard [5] which demands for the experiments to be reproducible. Tools have since been developed by Beltrame [7] and Bills [9] to evaluate the error and uncertainties of SU2 fluid dynamic simulations and ORCHID experiments, a standard procedure has been outlined based on their work to systematically validate the SU2 flow solver for NICFD. A simple unit case was run to assess the thermodynamic model for a unique operating condition. That case was the first step in the validation campaign and it was necessary to determine the suitability of the thermodynamic model. The conclusions from that assessment need to be generalized for a wider range of operating conditions. A rigorous hierarchy of cases to be executed to validate the flow solver for the physics in an ORC turbine needs to be defined. The cases should be executed to investigate each sub-model of the flow solver, including more complex ones through which the interaction between the sub-models can be studied.

To fill the knowledge gap, in this thesis different thermodynamic models will be compared to a reference model to determine their accuracy for a wide operational range. A detailed list of cases to be executed in order validate each sub-model, and the interaction between them, will be defined. The next unit case that will be performed is the generation of a shock wave with a wedge. The uncertainty quantification (UQ) infrastructure will be adapted for the first complex case, a linear cascade. This will pave the way for the assessment of the accuracy of important parameters for engineering design applications, such as efficiency. With this thesis the effort to validate the SU2 flow solver will move forward.

1.3. Objective

The objective of this thesis is to determine if the SU2 flow solver can adequately predict NICFD flows in the presence of shock waves and to adapt the infrastructure for the assessments of complex cases, such as a linear cascade. This will be achieved through the comparison of experimental data generated with the ORCHID to numerical simulations. The uncertainties will also be calculated to determine the quality of the validation. The specific research questions to answer are listed in this section.

1.3.1. Research Questions

The research question formulated is

> *Can the SU2 flow solver accurately predict complex flow structures in the NICFD regime?*

The primary research question can be split into several sub-questions listed below:

1. What is the domain of applicability of the Peng-Robinson equation of state?
2. How accurately can SU2 predict shock-wave angles and is it possible to characterize the associated uncertainties?
3. Is the flow solver able to predict the physics of the flow around more complicated shapes, such as a blade row?

1.3.2. Deliverables

The deliverables produced to answer the research questions are the following:

- Updated hierarchy of the paradigmatic test cases to be executed to validate a flow solver for the simulation of the flow physics in an ORC turbine;

- A series of operating maps which describes the accuracy of the Peng-Robinson equation of state;
- Generation of experimental data, from the ORCHID and from SU2 simulations, and their comparison to validate the code for two paradigmatic test cases; and,
- Initial evaluation of a linear cascade with SU2 simulations with recommendations for the future experiments.

1.4. Scope

This project will assess the SU2 flow solver, both with already acquired and with newly generated experiments. The older experiments were performed by Head [34]. The uncertainties, from the experiments and the simulations, will be quantified to calculate the validation metrics. The flow quantities for which the assessment will be performed are: the Mach number along the center line of the nozzle, the static pressure at the nozzle wall and the shock wave angle generated by a wedge. The validation does not include data extrapolation and it will be conducted only for the cases for which experimental data exists. A numerical assessment of a linear cascade will be performed but not compared to experiments.

1.5. Elements of Originality

In this section are listed the contributions made by this thesis.

- Definition of a detailed list of cases to be executed in order to validate a flow solver for simulating the flow physics in an ORC turbine;
- A series of operating maps showing the applicability range of different thermodynamic models; and,
- Measure of a shock wave generated with a wedge in a de Laval nozzle.

1.6. Overview

The thesis is structured in six chapters. In Chap. 2 the background knowledge required to understand the work performed is presented. There, each instrument and model used will be described. In Chap. 3, SU2 and the validation infrastructure will be explained in detail, then the first research question will be addressed and the concept of an operating map for thermodynamic equations of state will be introduced. In Chap. 4, the simulations and the experiments with a wedge will be presented, leading to the answer of the second research question. In Chap. 5, the initial numerical evaluation of a linear cascade is made, thus answering the final research question. In Chap. 6, the conclusions and recommendations are presented.

2

Background Knowledge

The study of organic fluids at high velocity, as they occur in ORC machines, is part of the classical NICFD branch of fluid dynamics. This regime is characterised by the density not being constant and by the non applicability of the ideal gas law. From a gas dynamics point of view, ideality is defined as a flow in which the speed of sound increases proportionally with the pressure. In this chapter the various theories and knowledge necessary to characterize this behaviour will be described.

Initially, the definition of organic fluids and the way to model them is presented. In Sec. 2.2 and 2.3, the characterization of non-ideal flows and of the shock phenomena which occurs in compressible flows will be described. A comprehensive description of the thermo-physical models used in the simulations is made in Sec. 2.4. Then, in Sec. 2.5, the mathematical formulation of the flow equations is introduced. It follows in Sec. 2.6, the description of the validation metrics which will be used. In the last section, the current state of the validation effort and the facilities in use are presented.

2.1. Organic Fluids

The organic Rankine cycle differs from a traditional Rankine cycle because of the use of organic fluids, which are defined by Seager and Slabaugh [63] as molecule with at least a carbon atom. In this validation campaign the fluid which will be used is siloxane MM. This molecule is part of a class called organosilicon which is characterised by the Si – O – Si bond.

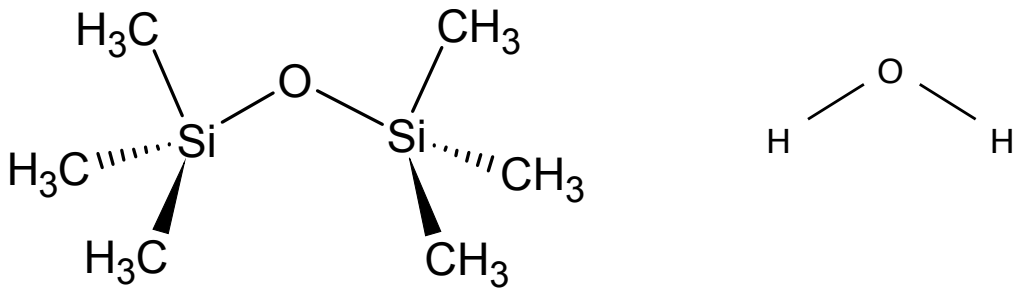

(a) (b)

Figure 2.1: Comparison of **a)** the Siloxane MM ($C_6H_{18}OSi_2$) molecule with **b)** water (H_2O). The difference in complexity and molecular mass can be clearly noticed.

As it can be seen in Fig. 2.1, the siloxane molecule is far more complex than a water molecule. Its molecular mass of 162.4 g/mol is also high, roughly 9 times heavier than H_2O. Heavy organic molecules deviate from ideal conditions. From the molecular complexity the shape of the slope of the saturation vapour curve can be predicted [44]. These differences allow to change several physical parameters which could not be chosen when only steam is considered. The choice of the fluid allows for one more degree freedom when designing the power plant [18]. Some of the most important parameters which characterize a fluid are the

vapor-liquid critical point, the saturation line and the specific heat. These are critical parameters to choose when a certain heat sources and sink are fixed.

To account for the different behaviour with respect to a simple spherical molecule, the acentric factor was defined by Pitzer et al. [54]. It stems from the principle of corresponding states which says that fluids at the same reduced pressure, temperature and volume have the same compressibility factor and so they similarly deviate from the ideal gas law. The reduced properties are the pressure and the temperature divided by the fluid's critical pressure and temperature. The principle works well with monoatomic and simple molecule, which all have a compressibility factor at the critical point Z_{cr} close to 0.3, but deviate as they get more complex. The deviation can be correlated with the acentric factor.

The acentric factor ω is defined as

$$\omega = -\log p_r^{sat} - 1, \tag{2.1}$$

with p_r being the reduced pressure, sat indicates that the value is taken at saturation, for a reduced temperature T_r of 0.7 [8]. For spherical molecules the value is close to 0, Siloxane MM has a value of 0.419 [62].

Phase changes are also of paramount importance in a Rankine cycle since they occur in the heating and cooling phase. Figure 2.2 shows the typical shape of a $T-s$ phase diagram is shown with the points of interest highlighted. A characteristic of organic fluids is that the liquid-vapor saturation curve has a positive slope with respect to temperature, unlike water. The part in white, where the flow is in liquid-vapor phase, is called the dome.

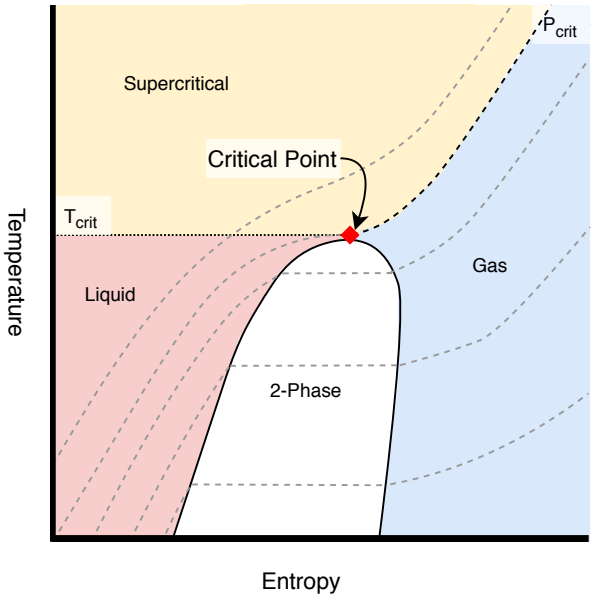

Figure 2.2: $T-s$ diagram showing the different phases of Siloxane and the critical isobar. Taken from Bills [9].

The expansions studied in this thesis occur in the superheated area, to the right of the dome. The zone close to the critical point and around the dome is where the non-ideality reach the maximum value. The supercritical zone is characterized by the fluid behaving non-ideally, where no distinction between gas and liquid is present.

2.2. Quantification of Non-Ideal Behaviour

A fluid is defined by Luder [42] as ideal if it behaves according to the ideal gas equation of state,

$$pv = RT, \tag{2.2}$$

where p is the pressure, v is the specific volume, R is the specific gas constant ($R = R_u/MW$) and T is the absolute temperature.

An ideal fluid is non-existent in nature, this equation assumes no volume occupied by the particles and no intermolecular forces present. Nonetheless it represents an acceptable approximation in cases where the temperature is high and the pressure is low.

As a gas departs from these conditions it deviates from ideality due to:

- compressibility effects;
- variable specific heat capacity;
- van der Waals forces;
- non-equilibrium thermodynamic effects; and,
- issues with molecular dissociation and elementary reactions with variable composition.

Compressibility effects are very important, particularly in the region close to the critical point and will be discussed in the rest of this section. The specific heat capacity, when deemed not constant, can be related to other properties such as the temperature. Van der Waals forces represent the interactions between molecules which in the ideal model is assumed to be nil due to the low pressure assumption. Modified equations of state can be chosen to account for this effect. Non-equilibrium thermodynamic effects are concerned with transport processes which are not relevant in this analysis due to the presence of only one molecule and no reactions. The last assumption is deemed valid in this thesis since the fluids of interest are operated far below their dissociation temperature.

Several parameters have been defined to describe the level of non-ideality of a flow. The most relevant for this study are described in the next sections.

2.2.1. Compressibility Factor

The compressibility factor Z can be used as a measure of thermodynamic ideality. It is defined as

$$Z = \frac{p}{\rho R T}, \tag{2.3}$$

with $Z = 1$ being the case of an ideal gas, per definition. At high pressure Z tends to be > 1 as the molecules collide often and this determine repulsive forces. On the opposite case, when the pressure is low, $Z < 1$ and attractive forces are present. The compressibility factor deviates from one as the critical point is approached [10]. A common way to visualize it is by plotting the reduced pressure and temperature against Z, since, as per the principle of corresponding states, for all gases it should theoretically show the same curves. In Fig. 2.3 the relation between reduced pressure and temperature with respect to the compressibility factor is shown for air. The shape for other ideal gases is very similar.

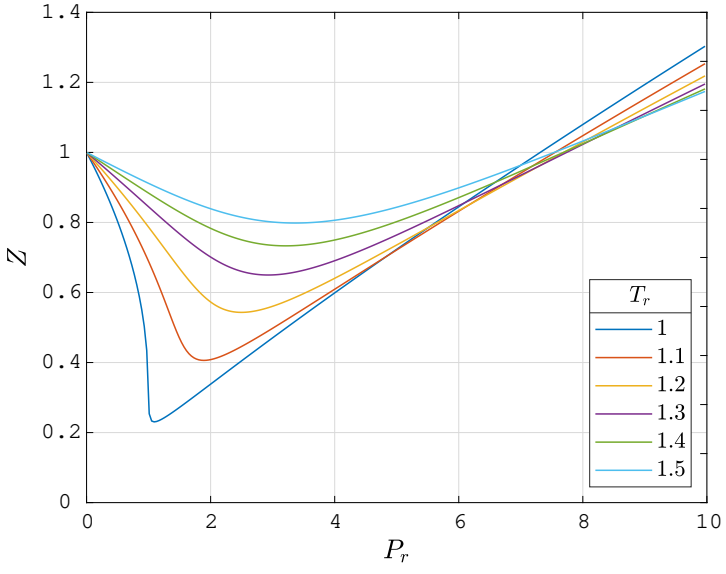

Figure 2.3: Reduced pressure and temperature against Z for air. Taken from Bills [9].

The compressibility factor is easy to calculate and it is useful to understanding how far from the volumetric ideal condition a fluid is. Yet, it is not very useful in the performance analysis of turbomachinery process. For those studies other parameters are preferred.

2.2.2. Isothermal Compressibility

Compressibility for an infinitesimal volume is defined as the variation in volume for a given change in pressure [4]

$$\tau = -\frac{1}{v}\frac{\partial v}{\partial p}. \tag{2.4}$$

Since the compression process can occur with varying ambient conditions, it is defined as isothermal compressibility the process when the temperature is kept constant

$$\tau_{\mathrm{T}} = -\frac{1}{v}\left(\frac{\partial v}{\partial p}\right)_T. \tag{2.5}$$

A different form related to Z can be used, so that it becomes

$$\tau_{\mathrm{T}} = \frac{1}{p} + \frac{1}{Z}\left(\frac{\partial Z}{\partial p}\right)_T, \tag{2.6}$$

clearly, for an ideal gas, the derivative is always equal to zero, which leads to $\tau_{\mathrm{T}} = \frac{1}{p}$.

2.2.3. Polytropic Exponent

An important parameter used in turbomachinery to describe the efficiency of a process is the polytropic exponent [75]. This coefficient, depending on its value, can be used to describe any thermodynamic process. A special case is an isentropic process, when entropy remains constant. In this case the exponent is equal to the heat capacity ratio and can be used in the form of $pv^{\gamma} = \text{const}$.

When used to describe a real process, its value would be larger that the isentropic case. If represented on a $T-s$ diagram, the entropy will increase. The polytropic exponent can also be described as

$$\gamma_{\mathrm{pv}} = -\frac{v}{p}\left(\frac{\delta p}{\delta v}\right)_s, \tag{2.7}$$

its relation with the ideal specific heat ratio is

$$\gamma_{\mathrm{pv}} = \frac{\gamma}{\tau_{\mathrm{T}} p}. \tag{2.8}$$

2.2.4. Fundamental Derivative of Gas Dynamics

A parameter used to characterize non-ideal flows is the fundamental derivative of gas dynamics derived by Thompson [74]. This thermodynamic quantity is defined by Nederstigt [50] as the change in sound velocity with pressure or density at constant entropy. It can be written as

$$\Gamma = 1 - \frac{c}{v}\left(\frac{\partial c}{\partial v}\right)_s \text{ or} \tag{2.9}$$

$$\Gamma = 1 + \frac{c}{v}\left(\frac{\partial c}{\partial P}\right)_s. \tag{2.10}$$

In Tab. 2.1 three possible cases are identified. When Γ is higher than one, the speed of sound is positively correlated with the density, which is what happens in classical ideal theory. On the other hand, if $0 < \Gamma < 1$, the behaviour is considered non-ideal. The case $\Gamma < 0$ is defined non-classical and it is not relevant for this study.

$\Gamma > 1$	$\left(\frac{\partial c}{\partial v}\right)_s < 0$	Classical ideal behaviour
$0 < \Gamma < 1$	$0 < \left(\frac{\partial c}{\partial v}\right)_s < \frac{c}{v}$	Classical non-ideal behaviour
$\Gamma < 0$	$\left(\frac{\partial c}{\partial v}\right)_s > \frac{c}{v}$	Non-classical behaviour

Table 2.1: Classical and non-classical behaviour relation with Γ.

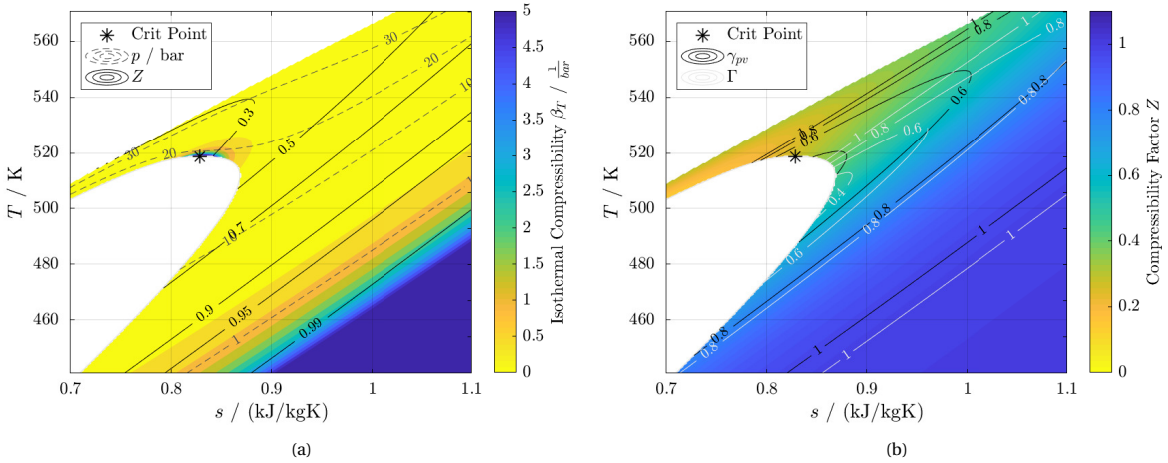

Figure 2.4: $T-s$ Diagrams of Siloxane MM comparing the various index of non-ideality. **a)** The colours show the isothermal compressibility while the continuous lines indicates the compressibility factor Z. **b)** The colours show the compressibility factor, the black lines indicate γ_{pv} while the light one Γ. Taken from Bills [9].

2.2.5. Synthesis

The metrics defined serve different purposes. The fundamental derivative is used to characterize the gas dynamic non-ideality, while the compressibility factor characterizes the thermodynamic non-ideality. Nonetheless, as shown in Fig. 2.4, all the metrics previously examined show a similar trend in the direction of the non-ideality. The closer the working point is to the critical point, the higher will be the deviation from ideality. Since it can be calculated more easily, the compressibility Z will also be used extensively.

The ideal gas region can be recognized with all the parameters and can be identified as the area where $Z > 0.99$ and $\Gamma > 1$. The main difference between all the indicators is in the magnitude. Near the critical point, the compressibility factor Z has a much sharper decrease than Γ and γ_{pv}, which might be misleading when evaluating the non-ideality. Γ and γ_{pv} have a much closer match, although with an offset, so they can both be considered good indicators of non-ideality. The latter is particularly useful for performance evaluation in turbomachinery.

2.3. Compressible Flow Phenomena

A flow in which the density is not constant is defined as compressible. The most used parameter to decide whether the density can be considered constant is the Mach number. It is defined as $M = \frac{u}{c}$, where M is the Mach number, u is the speed of the flow and c is the local speed of sound. A rough limit to consider the flow incompressible is $M = 0.3$, since at this threshold the error in the computation if the density is kept constant is lower than 5% [4]. Compressible flows are unavoidable in high speed vapour expansions which occur in the stator of ORC turbines.

A characteristic of supersonic flows are shock waves. These are defined by Anderson Jr [4] as "an extremely thin region across which the flow properties can change drastically". They can be separated in two forms, normal and oblique. The first case can occur, for instance, in an overexpanded supersonic nozzle, the second case is the most common and occurs when a shock makes an oblique angle with the flow, such as around a wedge or a cone. The former is the simplest case which can be used to study shock waves. The two types are shown in Fig. 2.5.

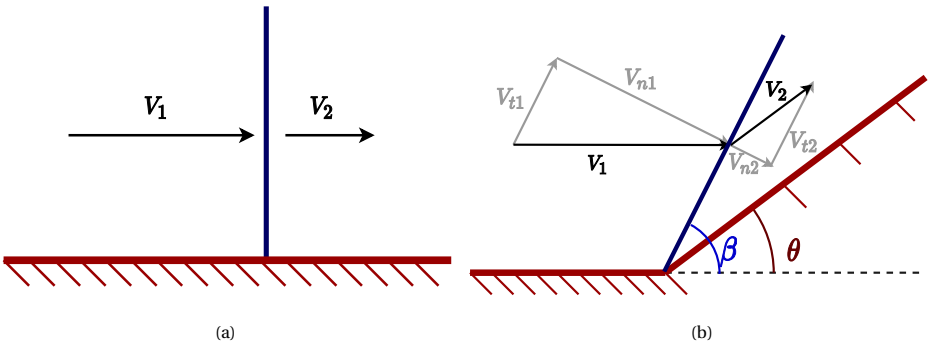

Figure 2.5: Comparison between **a)** a normal and **b)** an oblique shocks. Shown are also the velocity vectors. Taken from Bills [9].

2.3.1. Shock Waves

The normal shock wave case is described first since it can be considered as a sub-case of the oblique shock. The main objective of the normal shock wave analysis is to determine the flow properties downstream of the shock given the flow properties upstream of the wave. Since there exists a discontinuity in the flow, the preferred way to perform the study is through a control volume.

The three conservation equations, for mass, momentum and energy, are used. It is assumed that the gas is ideal so that the enthalpy-temperature relation and the ideal equation of state can be used. The relations here defined can be generalized and applied to both ideal gas and non-ideal gas cases, see App. D.1 and Grossman [30].

The equations used are the following

$$\rho_1 u_1 = \rho_2 u_2, \tag{2.11}$$

$$p_1 + \rho_1 u_1^2 = p_2 + \rho_2 u_2^2, \tag{2.12}$$

$$h_1 + \frac{u_1^2}{2} = h_2 + \frac{u_2^2}{2}, \tag{2.13}$$

$$h_2 = c_p T_2, \tag{2.14}$$

$$p_2 = \rho_2 R T_2, \tag{2.15}$$

where subscript 1 indicates a value before the shock and subscript 2 indicates a value after the shock. h is the enthalpy.

Since there are five unknowns and five equations, the system can be solved. Including the definition of Mach number, the properties of interest can be calculated with the following equations

$$M_2^2 = \frac{1 + [(\gamma-1)/2] M_1^2}{\gamma M_1^2 - (\gamma-1)/2}, \tag{2.16}$$

$$\frac{\rho_2}{\rho_1} = \frac{u_1}{u_2} = \frac{(\gamma+1) M_1^2}{2 + (\gamma-1) M_1^2}, \tag{2.17}$$

$$\frac{p_2}{p_1} = 1 + \frac{2\gamma}{\gamma+1}\left(M_1^2 - 1\right), \tag{2.18}$$

$$\frac{T_2}{T_1} = \frac{h_2}{h_1} = \left[1 + \frac{2\gamma}{\gamma+1}\left(M_1^2 - 1\right)\right] \frac{2 + (\gamma-1) M_1^2}{(\gamma+1) M_1^2}. \tag{2.19}$$

It is interesting to see that the final conditions only depends on the specific heat capacity ratio, which is a fluid property, and the initial Mach number. These kind of waves are characterized by a non-isentropic increase in pressure, temperature and density. The Mach number after the shock is always lower than one.

Oblique shock waves occur when a supersonic flow makes an oblique angle with the downstream flow. In case the flow encounters a concave corner, so that the flow is turned into itself, the pressure after the shock is non-isentropically increased. This case is shown in Fig. 2.6a.

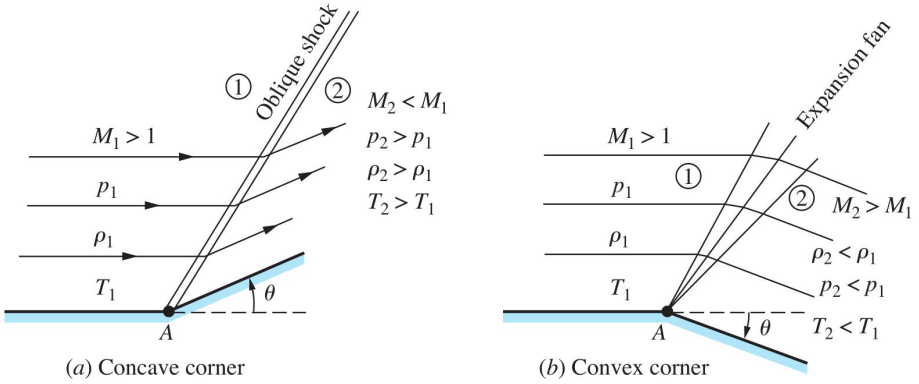

Figure 2.6: **a)** shows an oblique shock wave. **b)** shows an expansion fan. Taken from Anderson Jr [4].

To solve for the flow properties after the shock, a similar approach to the normal shock wave case is applied. A control volume is taken and the velocity vectors are divided in parallel w and orthogonal u components with respect to the shock wave, as shown in Fig. 2.7.

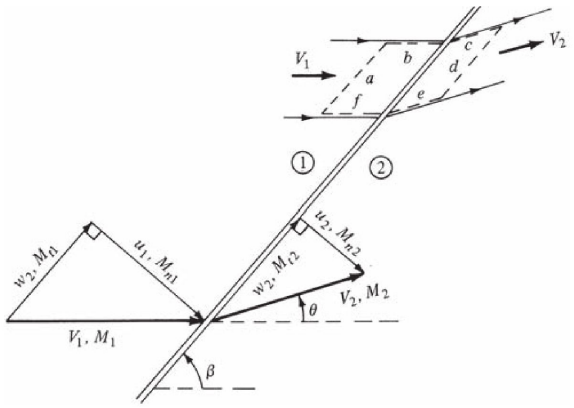

Figure 2.7: Control volume used to evaluate the shock characteristics. Taken from Anderson Jr [4].

Combining the continuity and the momentum conservation equation for the tangential direction, it is possible to determine that the tangential component of the flow velocity remains constant. Instead, the conservation equations for the orthogonal components are the same as the one used for normal shock waves. So, it is possible to consider the same relations while using the normal Mach number $M_{\mathrm{n},1}$ as the initial Mach number. $M_{\mathrm{n},1}$ is defined as

$$M_{\mathrm{n},1} = M_1 \cdot \sin\beta, \tag{2.20}$$

where β is the shock wave angle with respect to the initial flow direction and the subscript n indicates the normal component of the Mach. Through geometric relations it is possible to define the Mach number after the shock as

$$M_2 = \frac{M_{\mathrm{n},2}}{\sin(\beta-\theta)}, \tag{2.21}$$

θ represents the deflection angle, which is the angle made by the obstacle which is causing the shock with respect to the flow direction. Using geometrical arrangement, the $\theta-\beta-M$ relation is found

$$\tan\theta = 2\cot\beta \frac{M_1^2\sin^2\beta - 1}{M_1^2(\gamma+\cos 2\beta)+2}. \tag{2.22}$$

This equation is important since it allows to compute the shock angle when the flow deflection angle and the Mach number are known. When two out of three parameters are known, the third is fixed. It is often found in graphic form for a specific gas. The plot for siloxane is visible in Fig. 2.8. For each combination two solutions are possible, one called strong, since it leads to a subsonic flow and higher losses, while the second is weak, and it is the common one in nature. All oblique shock waves are weak [4].

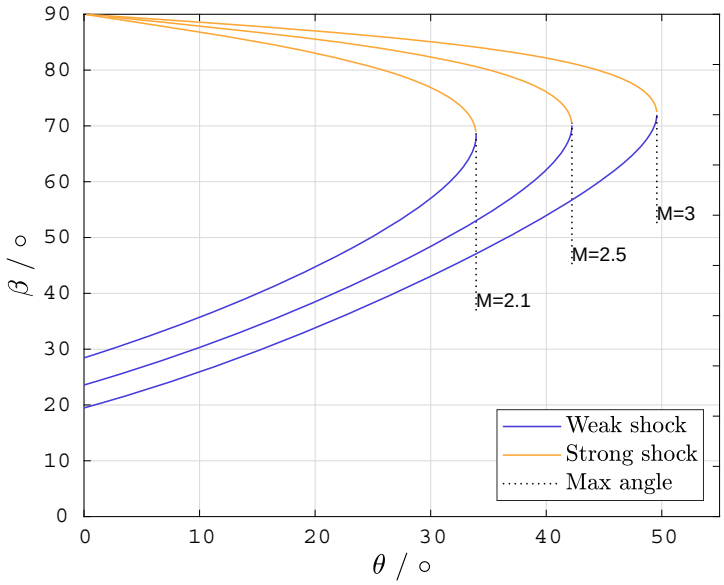

Figure 2.8: $\theta - \beta - M$ plot for Siloxane MM. Adapted from Bills [9].

2.3.2. Expansion Fan

The opposite case of the oblique shock is the expansion fan. This occurs when a convex corner is present. In this case there exists a continuous isentropic expansion process where the pressure decreases. These are common for instance in the supersonic part of a nozzle.

As it can be seen in Fig. 2.6b, two Mach lines can be identified, the forward and the rearward one. For an ideal flow, the angles are related to the Mach number through: $\mu_1 = \arcsin 1/M_1$ and $\mu_2 = \arcsin 1/M_2$. Where μ indicates expansion wave angles. Between these lines there will be an infinite series of isentropic expansions.

2.4. Thermo-Physical Models

In this section the various models necessary to describe non-ideal flows are presented. These are the equation of state, the heat capacity, the departure functions and the transport models.

The equation of state is examined thoroughly given that it is the first equation to be assessed in this initial phase of the validation campaign. The options included in SU2 are examined. The multiparameters equation of state is also included since it can provide a much higher accuracy with respect to the other options and so it is preferred choice outside the applicability range of the cubic equations of state.

2.4.1. Equations of State

To correctly describe a fluid outside the ideal gas region various models have been developed, each with varying degree of fidelity and computational cost.

The Van der Waals equation is the simplest cubic model in use. Its improvement over the ideal model is due to the introduction of factors to account for the volume occupied by the molecules and for the attractive or repulsive intermolecular forces. It is presented here since it allows to easily understand how these factors influence the ideal equation of state.

The Van der Waals EoS can be written in the following form

$$\left(p + a\frac{1}{V_m^2}\right)(V_m - b) = R_u T, \tag{2.23}$$

where a and b are gas dependent factors used to account for non-ideal behaviour, V_m is the ideal volume occupied by a mole of molecules, p is the pressure, T is the temperature and R_u is the universal gas constant [10]. This model does not offer an adequate precision in zones close to the critical point, so it is not used in this thesis.

An improvement over the Van der Waals model is the Peng-Robinson equation. It has a similar form to the previous one, but adopt an improved intermolecular force model and a corrective value to a related to the acentric factor. It was developed in order to improve the predictions close to the critical point and it was required to only be related to the critical properties and the acentric factor [52]. It can be written in the following way

$$\left(p + \frac{a\alpha}{{V_\mathrm{m}}^2 + 2bV_\mathrm{m} - b^2}\right)(V_\mathrm{m} - b) = R_\mathrm{u} T. \tag{2.24}$$

Factors a and b are given by the following formulas

$$a \approx 0.45724 \frac{R_\mathrm{u}^2 T_\mathrm{cr}^2}{p_\mathrm{cr}} \quad \text{and}$$
$$b \approx 0.07780 \frac{R_\mathrm{u} T_\mathrm{cr}}{p_\mathrm{cr}}.$$

The subscript cr indicates a property at the critical point. These parameters are defined only by the critical temperature T_cr and the critical pressure p_cr. The factors are an improvement over the ones used in the Van der Waals EoS and they stem from the theorem of corresponding states, which says that the curve of the compressibility factor with respect to the critical properties are similar in all simple gases. Since alone they are not accurate enough when complex molecules are used, two further parameters are used in the Peng-Robinson equation: α and κ. They are related to the acentric factor ω to account for the residual difference. They are defined in the following form

$$\alpha = \left(1 + \kappa\left(1 - T_r^{\frac{1}{2}}\right)\right)^2, \tag{2.25}$$

$$\kappa \approx 0.37464 + 1.54226\omega - 0.26992\omega^2, \tag{2.26}$$

$$T_\mathrm{r} = \frac{T}{T_\mathrm{cr}}. \tag{2.27}$$

The final cubic model used in this thesis is the improved Peng-Robinson EoS modified by Stryjek and Vera (iPRSV) equation of state. The Peng-Robinson EoS modified by Stryjek and Vera (PRSV) model, of which the iPRSV is a refinement, is itself an improvement of the original Peng-Robinson equation. Its main objective was to increase the accuracy of the acentric factor fit and to introduce a pure component parameter related to the critical temperature [72]. The equation used in the PRSV model is the same as the Peng-Robinson EoS, what differs is the definition of κ,

$$\kappa = \kappa_0 + \kappa_1\left(1 + T_\mathrm{r}^{\frac{1}{2}}\right)(0.7 - T_\mathrm{r}), \tag{2.28}$$

$$\kappa_0 = 0.378893 + 1.4897153\omega - 0.17131848\omega^2 + 0.0196554\omega^3, \tag{2.29}$$

the authors suggest to keep κ_1 equal to zero when T_r is above 0.7. The problem introduced by the pure component is a discontinuity when κ_1 differs from zero.

van der Stelt et al. [76] worked to fix this problem with the iPRSV. The equation they proposed is the following

$$\kappa = \kappa_0 + \kappa_1\left\{\sqrt{|\,A - D(T_\mathrm{r} + B)]^2 + E} + A - D(T_\mathrm{r} + B)\right\}\sqrt{T_r + C}, \tag{2.30}$$

where κ_0 and κ_1 are the same as in the original equation, while A, B, C, D and E are constant which are provided in the same paper.

The equations of state previously defined provide very good prediction in many cases of interest for non-ideal gases. Nonetheless, due to the inherent limitations of a cubic fit, they might not be accurate enough in highly non-ideal conditions, especially very close to the critical point [16].

Models developed to be as accurate as the experimental data are the multiparameters equation of state. This type of EoS are defined as empirical since they are not modeled to relate to a physical phenomena but to fit well the available data Span [66].

Many formulations are possible. The one preferred in modern application are in term of the reduced Helmholtz energy, since this property is continuous across all the domain. The equation in this form are divided in two components, one describing the ideal behaviour of the gas at a given point, the other describing the residual behaviour of the non-ideal flow [67].

The equation is then written in the following form

$$\frac{a(T,\rho)}{RT} = \frac{a^{\circ}(T,\rho) + a^{\mathrm{r}}(T,\rho)}{R,T} = \alpha^{\circ}(\tau,\delta) + \alpha^{\mathrm{r}}(\tau,\delta), \tag{2.31}$$

a represents the specific or molar Helmholtz energy, R is the gas constant, T the temperature, ρ the density, τ the inverse reduced temperature, and δ the reduced density. The superscript $^{\circ}$ indicates the ideal component, while the r the residual part.

The advantage of using the Helmholtz energy is that it is only a function of the density and the temperature. When these are known, all the other properties can be found by taking the derivative of the function. The relations are available in the paper by Span and Wagner [67]. As an example, the derivative to find pressure is presented

$$p(T,\rho) = -(\partial a/\partial v)_{\mathrm{T}}, \tag{2.32}$$

$$\frac{p}{\rho RT} = 1 + \delta\alpha^{\mathrm{r}}_{\delta}, \tag{2.33}$$

$$\alpha^{\mathrm{r}}_{\delta} = \left(\frac{\partial\alpha^{\mathrm{r}}}{\partial\delta}\right)_{\tau}. \tag{2.34}$$

To find α^0, the heat capacity function, which is known precisely for a large number of molecules, needs to be integrated. The complex part is determining the coefficients of α^{r}, which are found through interpolation of experimental data [67]. For each fluid a number of parameters are chosen, often 12, which describes the residual Helmholtz energy.

2.4.2. Heat Capacity

When a constant heat capacity assumption is not deemed acceptable, a polynomial function of the temperature is used. This data can be found for instance in the joint army navy NASA and air force (JANNAF) database [49] and in RefProp, where the coefficient of the polynomials for different fluids are present in the following form

$$c_p = \eta_1 + \eta_2 T + \eta_3 T^2 + \eta_4 T^3 + \eta_5 T^4, \tag{2.35}$$

where C_{p} is the heat capacity at constant pressure, the various η are determined experimentally and are specific for each gas, T is the temperature.

2.4.3. Departure Functions

The departure function is defined for a thermodynamic property as the difference between the real and the ideal value of the property [55]. Of interest are usually the departure function for enthalpy and entropy. The formulas for both of them are provided

$$\frac{H^{\mathrm{ig}} - H}{RT} = \int_V^{\infty}\left[T\left(\frac{\partial Z}{\partial T}\right)_V\right]\frac{\mathrm{d}V}{V} + 1 - Z, \tag{2.36}$$

$$\frac{S^{\mathrm{ig}} - S}{R} = \int_V^{\infty}\left[T\left(\frac{\partial Z}{\partial T}\right)_V - 1 + Z\right]\frac{\mathrm{d}V}{V} - \ln Z, \tag{2.37}$$

where Z is the compressibility factor, H and S are the enthalphy and the entropy.

A version of this equation to be used with the Peng-Robinson EoS is available, which only requires the critical properties of the gas, the compressibility factor and the acentric factor to determine the departure.

State properties are used since only the difference between the points in question is important and not their exact value. This allows the process to take any path, as long as the initial and final state are the same as the one in analysis. For instance, it is possible to reduce the pressure to zero through an isothermal process, to have an ideal gas. Then heat is added, and finally the pressure restored, to account for intermolecular forces.

2.4.4. Transport Models

The final equations used to describe the flow are the ones describing transport of heat and of momentum. The two relations are similar since they are both proportional to the gradient, respectively, of temperature and velocity,

$$q_x = -k\frac{\partial T}{\partial x}, \tag{2.38}$$

$$\tau_x = \mu^{\nu}\frac{\partial u}{\partial y}, \tag{2.39}$$

where q and τ are the heat flux density and the shear stress in the x direction. k is the thermal conductivity, μ^{ν} is the viscosity of the fluid and u is the velocity.

μ^{ν} can either be constant or be given by Sutherland's law [41]. This relation is simple and usually provide a good approximation. It relates the viscosity to the temperature

$$\mu^{\nu} = \mu^{\nu}_{\text{ref}}\left(\frac{T}{T_{\text{ref}}}\right)^{3/2}\frac{T_{\text{ref}}+S}{T+S}, \tag{2.40}$$

μ_{ref} and S are determined experimentally, while T_{ref} is the reference temperature.

A more sophisticated model that can be used to determine both the viscosity and the heat transfer coefficient was defined by Chung et al. [11]. It takes into account acentric factor, the dipole moment and the association parameter [12].

2.5. Mathematical Representation of NICFD

The principle behind CFD is to divide the domain into very small cells which exchange mass, momentum and heat provided some boundary conditions. Depending on the flow in analysis, different set of conservation equations should be used. In this thesis the flow studied is always compressible and in some cases viscosity is relevant, so the Navier-Stokes equations are used. When viscosity can be neglected the Euler equations are used.

2.5.1. Navier-Stokes Equations

The exact conservation equations required to describe a flow are the Navier-Stokes equations,

$$\frac{\delta\rho}{\delta t} + \nabla\cdot(\rho\vec{U}) = 0, \tag{2.41}$$

$$\frac{\delta(\rho u_j)}{\delta t} + \frac{\delta\rho u_i u_j}{\delta x_i} + \frac{\delta p}{\delta x_j} - \frac{\delta\tau_{ij}}{\delta x_i} - f_j = 0, \tag{2.42}$$

$$\frac{\delta(\rho e)}{\delta t} + \frac{\delta(u_i\rho e)}{\delta x_i} + \frac{\delta(u_i p)}{\delta x_i} - \frac{\delta u_i\tau_{ij}}{\delta x_i} + \frac{\delta q_i}{\delta x_i} - u_i\rho f_i = 0, \tag{2.43}$$

u represent the velocity vector for a given direction, τ_{ij} is the i, j component of the stress tensor, f represent the body forces applied and q is the term for heat transfer.

The Euler equations can be seen as particular Navier–Stokes equations with zero viscosity and zero thermal conductivity. For some problems, such as an expansion in a nozzle, a solution of the Euler equations provides a good model of reality.

2.5.2. Simplified Conservation Equations

Since a direct numerical simulation using the Navier-Stokes equations would be prohibitively expensive, simplifications are introduced in most flow solvers. A commonly used set of equations are the Reynolds-Averaged Navier-Stokes (RANS) equations. In this framework only the average value over time of each cell is considered, disregarding fluctuations. This allows to avoid calculating many parameters, but it also leaves one parameter to be modeled, the Reynolds stress tensor. This can be defined in different ways, but usually requires one or more additional transport equation.

The available turbulence models in SU2 are the Menter's Shear Stress Transport turbulence model (SST) and the Spalart–Allmaras turbulence model (SA). The SST model blends the $k-\omega$ with $k-\epsilon$ family of turbulence solver and it is known for its quality when used with low Reynolds internal flows. For further details on this model see Menter [46]. The SA model was initially developed to deal with aerodynamics applications. It is used for the simulation of internal flows since it gives good convergence behaviour [3].

2.6. CFD Solvers Validation

After a model is conceptualized and implemented, two important steps remain to be done, verification and validation. These tasks are not merely the comparison between the experimental results and the simulation predictions, but more complex tasks which have to be performed according to standards. Verification is defined by Roache [58] as "a purely mathematical exercise that intends to show that we are solving the equations right". Verification usually involves a code check to determine whether the solution can be generated without errors. This activity is not part of this thesis and it is assumed to be completed already. Validation instead is the comparison of experimental and simulation of data and their uncertainties. In this section three validation models will be presented, the V&V 20 standard [5], the Real Space metric [60] and the Hills [35] model.

2.6.1. Methodology

Validation is defined by the American Institute American Institute of Aeronautics and Astronautics (AIAA) [2] as: "the process of determining the degree to which a model is an accurate representation of the real world from the perspective of the intended uses of the model". This activity requires a series of physical experimental data and their uncertainties to be compared with simulations using the model to be validated.

The strategy devised to validate the SU2 flow solver stems from a paper by Oberkampf and Trucano [51]. There, the optimal way to validate a complex system is identified in the definition of a tiered hierarchy. Figure 2.9 shows the hierarchy devised to validate the flow solver to simulate the flow physics in an ORC Power Plant. The division made is in sub-systems, benchmark cases and unit tests. The latter has to have only a single model validated independently of the others to clearly define the error source. Going up the hierarchy, the geometry complexity and the coupling effect of different physical phenomenon increase. The system level represents the actual component which the model should represent, at this level it is usually expensive to make experiments and it is difficult to determine the sources of error. Usually, particularly in industry, the interest at this level is on the output of engineering responses, such as efficiency. The sub-system tier involves only a part of the complete model and two or three physical domains coupled. Similar difficulties are present with respect to the previous level. At the the benchmark layer, usually a simplified component is used, and different phenomena of the same physical domain are studied. In the unit tests a single model or equation is studied, making it possible to keep the uncertainty to a minimum [51].

The current focus is on the turbine, due to the importance on the overall efficiency of the system, for which the benchmark and unit levels are developed in Fig. 2.9. The isentropic expansion was the first case run [33, 71]. The next unit test to be studied is the shock wave generation. These unit tests are designed to only involve the equation of state, since no turbulence or viscous effect is present. The shapes used are very simple, respectively a supersonic nozzle and a wedge. A more complex study, already at the benchmark level, is the cascade blade row. In this case multiple complex shapes, the blades, interact with each other through their shock waves. Turbulence and viscosity are relevant because the entropy generated in the boundary layers decrease the efficiency, this loss source can make up one third of the total losses in turbomachines [21].

2.6.2. Modern Design of Experiment

The modern design of experiment consists in a series of improvements to a traditional experiment procedure with the objective of decreasing the variance without increasing the number of simulations required or to determine which independent input influences the output the most. For instance, it is possible to lower

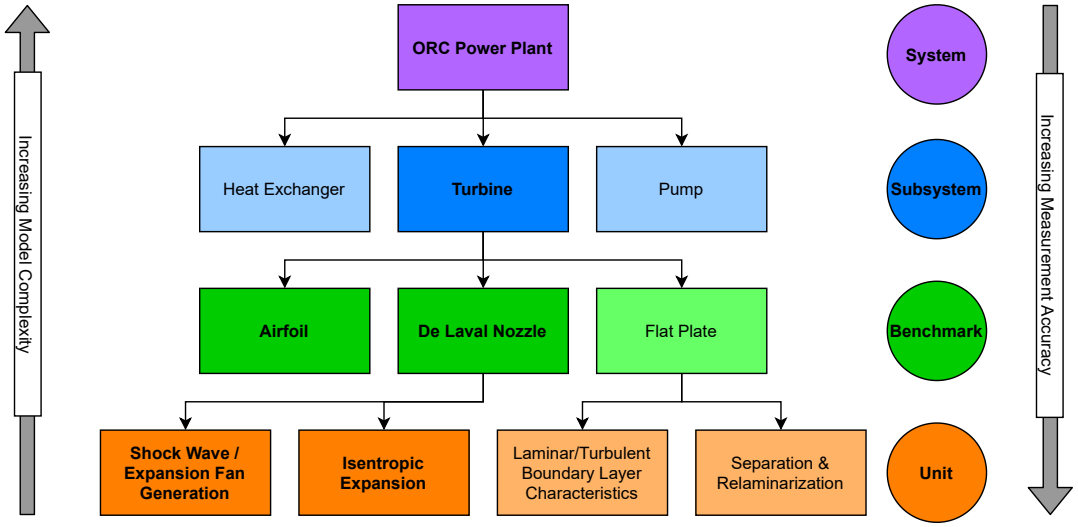

Figure 2.9: Subdivision in hierarchical cases to be performed to validate the flow solver for the flow physics of a complete ORC Power Plant. The dark orange boxes represent the unit cases analysed in this thesis.

the number of simulations by combining different input in few non-dimensional ones. To determine the influence of each input a stochastic simulation can be run. Examples are provided in Mehta et al. [45].

The final objective of the validation effort is to produce a database of test cases with the experiments and the simulations for which the design of experiment principles are applied. The way to achieve this is to use a validation model which not only consider the deterministic responses, but also all the sources of uncertainty. The inspiration for the test cases chosen is the *National Project for Application-oriented Research in CFD (NPARC) Alliance Verification and Validation Archive* by NASA [64].

2.6.3. V&V 20 Validation Standard

There exists different standards defined with CFD validation in mind. The metric currently in use for this research is the American Society of Mechanical Engineers (ASME) V&V 20 [5]. The idea behind it is to compare the uncertainty of the simulations and the experiments at a given point to identify whether the model error is small enough or absent.

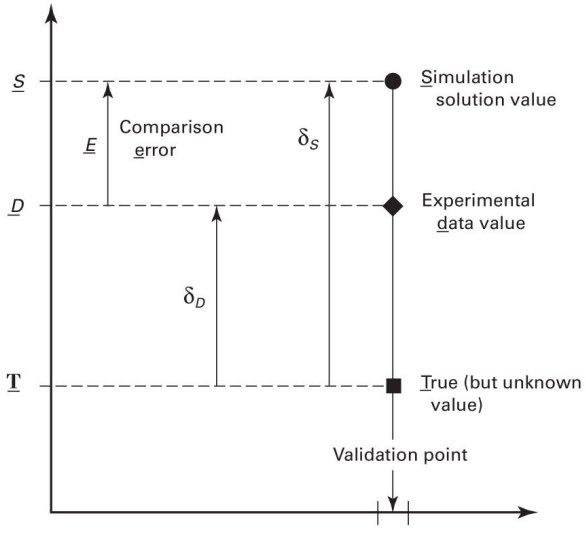

Figure 2.10: Relation between the true, but unknown, value with the simulation and experimental ones for a given validation point. Taken from ASME [5].

Consider now the situation in Fig. 2.10. It is assumed that at each evaluated point there is a true, but

unknown, value T. From the experiments, another value D is recorded. Finally, with a simulation a third point S is determined. The comparison error E is then defined as

$$E = S - D, \tag{2.44}$$

and it can be calculated with the data available. Next, are defined the simulation error δ_S and the experimental error δ_D in the following way

$$\delta_S = S - T, \tag{2.45}$$

$$\delta_D = D - T, \tag{2.46}$$

combining these equations together

$$E = S - D = (T + \delta_S) - (T + \delta_D) = \delta_S - \delta_D, \tag{2.47}$$

this relation shows that the comparison error is a combination of the experimental and the simulation error. The simulation error δ_S can then be decomposed in three components:

1. δ_{model}, due to modeling assumptions and approximations;
2. δ_{num}, due to the numerical solution of the equations; and,
3. δ_{input}, due to the errors in the simulation input parameters.

The comparison error can now be written in this form

$$E = \delta_{\text{model}} + \delta_{\text{num}} + \delta_{\text{input}} - \delta_D. \tag{2.48}$$

Since the objective of the analysis is the evaluation of the modeling error, the previous relation can be rewritten in this way

$$\delta_{\text{model}} = E - \left(\delta_{\text{num}} + \delta_{\text{input}} - \delta_D\right), \tag{2.49}$$

E is known, the other errors need to be calculated. A validation standard uncertainty can be defined as u_{val}, which is a value that combine all the uncertainties of the factors previously defined. If the error sources are independent of each others the validation uncertainty can be calculated with the following formula

$$u_{\text{val}} = \sqrt{u_{\text{num}}^2 + u_{\text{input}}^2 + u_{\text{d}}^2}. \tag{2.50}$$

The case found is then

$$\delta_{\text{model}} = E \pm u_{\text{val}}, \tag{2.51}$$

the conclusion that can be drawn is that the model error must be contained in the interval defined by this relation. If $u_{\text{val}} > E$, then it can be said that the model error is inside the uncertainty band of the experimental set-up, so it is either not be present or, if present, it is not possible to define it with the uncertainty of the current set-up. On the other hand, if $u_{\text{val}} < E$ an error is surely present.

This method is straightforward and already well tested. Its main drawback is that it only provide a yes-no answer to the validation question which makes it difficult to understand the source of the error. Furthermore, it can lead to flawed conclusions since an increase in experimental error can hide the modeling error inside the uncertainty band, which would make the model validated in the case where the measurement has a large uncertainty.

2.6.4. Real Space Model

The Real Space metric [60] separates the contributions of the experimental and simulation uncertainties to clearly identify the sources of uncertainty. The uncertainties are associated to the mean of the experiments and the simulations. Romero defines four possible outcomes of the assessment:

- Zero order validity, when the uncertainty bands of the simulation completely enclose the uncertainty of the experiments. All the possible reality is simulated;
- Dubious validity, when the simulation uncertainty is contained in the experimental one or the uncertainty bands partially overlap. Only a portion of reality is captured; and,
- Invalid case, when the uncertainty bands do not overlap.

2.6.5. Hills Validation Model

An alternative method, which can provide a global grade of validation, was made by Hills [35]. In this model, a multidimensional space is imagined, with each measure performed increasing the dimension of the space by one. The value of the experiment and the simulation is then positioned in this space, with their probability distribution function (PDF) due to their uncertainties. If both uncertainties are combined in a single iso-PDF around the prediction point, where each contour has the same probability, it is possible to determine the probability that the measure is accurate. The case is shown in Fig. 2.11. It is suggested by the author to consider a model valid if the measure is within the 95% confidence level.

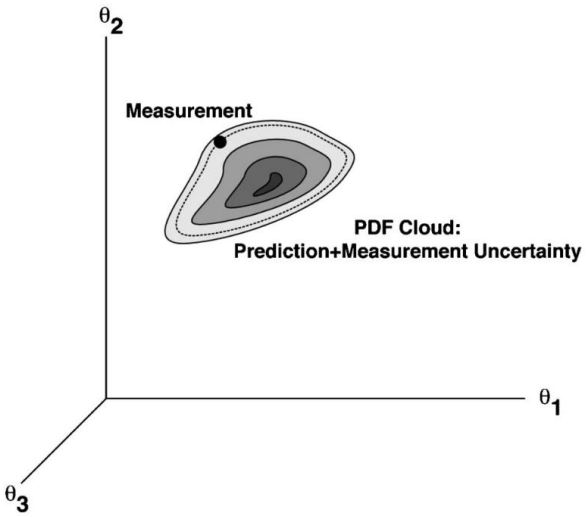

Figure 2.11: Probability density function of the combined uncertainty in a three dimensional space. Taken from Hills [35].

The metric used to calculate the position in the iso-PDF is based on the weighted least squares r^2. The formula to calculate it is the following

$$r^2 = \left(\mathbf{X}_{\text{model}} - \mathbf{X}_{\text{exp}}\right)^{\mathrm{T}} \left[\mathbf{cov}^{-1}\left(\mathbf{X}_{\text{model}} - \mathbf{X}_{\text{exp}}\right)\right] \left(\mathbf{X}_{\text{model}} - \mathbf{X}_{\text{exp}}\right), \tag{2.52}$$

where $\mathbf{X}_{\text{model}}$ is the vector of the model predictions and $\mathbf{X}_{\text{exp}}$ is the vector of the experimental observations. The **cov** operator is used to calculate the covariance of the differences between model and experimental observations. The comparison that can be made can include different properties or experimental conditions.

To calculate the covariance matrix, Hills proposed a first order sensitivity analysis based on an approximation around the mean. Since an equivalent infrastructure to calculated the input uncertainty already exists, those steps will not be necessary. In the next section the procedure used will be presented.

The metric compares the radius of the hyper-ellipse r defined by the set of points considered with a reference radius r_{ref} for a corresponding normal distribution. For a result lower than one, the comparison errors outside the normal distribution are less than expected for the normal distribution with the given number of points, and so it can be considered valid. If the value is higher than one, the case is not valid since the comparison errors outside the normal distribution are more than expected.

This model allows to define a probability that the assessment is valid, which is an improvement with respect to the output of the V&V 20 Model. This increased precision comes at a cost in term of calculation complexity. Furthermore, the concern of the previous model, the validation with large experimental uncertainty, is not addressed, since with this model a large experimental uncertainty would just extend the PDF cloud size.

2.6.6. Uncertainty Quantification

When the metric is defined, it is necessary to collect all the data required to find the model error. In the evaluation of the total uncertainty are not only important the numerical and experimental uncertainties, but also those caused by uncertainty in the input.

In simple calculations, the uncertainties can usually be added or related in some ways. But when a large number of input values are involved, with their relation generally unknown, the analytical estimation of the uncertainty is complicated. For these cases the Monte Carlo method is often used. It consists in a large number of simulations where in each one random combinations of input parameters are run to determine their influence on the output. The input are chosen in their uncertainty band, the large number of simulations allow to determine the uncertainty of the output responses. ASME [5] recommends the use of Latin Hypercube Sampling for this task. This method is similar to the Monte Carlo, but it usually requires less iterations to produce the same results since equal probability zones are defined to avoid the concentration of the samples close to each others.

Alternative methods are the stochastic simulations. These type of simulations consists in a series of model run which provide a mean and a standard deviation of the output. The most commonly used way to use this model is through Polynomial Chaos, a variant of stochastic collocation, in which a surrogate model is prepared with the same statistical behaviour of the original one, but computationally faster, since it only require polynomials to be solved [19].

A way to quantify the relative influence of the input on the final output is through the Sobol Index. The sources of uncertainty are found through a variance based decomposition sensitivity study. This allows for some parameter to be considered exact, and their uncertainties discarded, if the influence on the output is low. A Sobol Index for an input equal to one indicates that the parameter is the only one influencing the output, viceversa a index of zero indicates no influence on the uncertainty [65].

2.7. Facilities for the Research of Non-Ideal flows

Studying non-ideal flows requires dedicated facilities which are limited in number. The main ones currently in operations are the TROVA in Milan Polytechnic, the Closed Loop Organic Wind Tunnel (CLOWT) in the University of Münster and the ORCHID in TU Delft.

In this section the state of NICFD validation will be presented. The first part deals with the experiments at the TROVA facility, while the second with the ones at the ORCHID.

2.7.1. TROVA

The TROVA is a blow down wind tunnel using siloxane MDM as working fluid. It can reach pressure of up to 50bar and temperature of 400°C [68]. This type of facility does not allow for extended period of operations since they need a vacuum at the outlet to be maintained, for this reason steady state conditions are more difficult to achieve or have to be assumed as such. Pressure, temperature and the flow field in a given section can be recorded. Schlieren imaging is also used to visualize the density and the flow shocks [69].

An assessment of the SU2 flow solver was first made by Gori et al. [28]. In this paper a supersonic expansion and the shock waves generated with a diamond shaped airfoil are assessed. It is shown that the predictions and the experiments are in good agreement, but no uncertainty estimation is made. This does not match the requirements of the V&V 20 standard, so it cannot be considered a true validation. A second campaign, with uncertainty considered, was presented in Gori et al. [29]. The positive evaluation of the SU2 flow solver is confirmed, but the metrics are still not up to the standards available.

Further information on the tests and the facilities are available in Spinelli et al. [70] and Spinelli et al. [71].

2.7.2. ORCHID

The ORCHID is currently the state-of-the-art facility for the investigation of NICFD flows. It is designed to simulate a complete ORC power plant, the current focus is on the turbine and the heat exchanger. The preliminary design was presented in Head et al. [32]. Of interest for the validation to be performed in this thesis

is supersonic nozzle section. There, Siloxane MM can be expanded up to Mach 2.1 in steady-state condition. The envelope of operation of the machine is dependant on the fluid and for MM it is set as a pressure of 25 bar, temperature of 300°C and a thermal power supply of 400 kWth. Measurement devices are available to gauge the static pressure at 16 points along the mid-plane of the nozzle. A window is also available to visualize the flow with a schlieren set-up. Figure 2.12 show the facility, in the foreground the nozzle test section can be seen.

Figure 2.12: The ORCHID, in the bottom-right of the picture can be seen the nozzle window. Taken from Head [34].

The validation infrastructure currently in use is described by Head et al. [33]. The metric Head identified to validate the SU2 flow solver is the V&V 20 standard, which was described in the previous Sec. 2.6.3. The envisaged experiments are aimed at validating a complete ORC turbine.

For the assessment of the validation infrastructure, Head compared pseudo-experimental data generated with Ansys CFX with SU2 simulations. The results were encouraging, and worth to further develop in the current validation campaign. The validation campaign was started in 2019 by Bills [9] and Beltrame [7]. They refined the validation infrastructure to the current state and they performed the first validation of isentropic supersonic expansions.

3

Technical Approach

In this chapter a methodology to perform the validation of a NICFD solver is described. More specifically, a series of paradigmatic test cases are proposed for the critical validation assessment of non-ideal flow solvers such as SU2. Initially, the computational submodels of the SU2 flow solver, including the numerical infrastructure, will be presented. Section 3.3 shows a series of operating maps which displays the deviation of thermodynamic properties on the $T-s$ and the $P-T$ diagram for different Thermodynamic models. This task is performed to highlight the most suitable set of boundary conditions for conducting experiments where the thermodynamic model is under investigation. Section 3.4 summarizes the steps of the procedure used in the validation.

3.1. SU2: The Open-Source NICFD Solver

This section describes the SU2 flow solver and the features implemented which are used for NICFD applications. Economon et al. [26] developed the open source flow solver in 2015, and in 2017 it was configured and verified for NICFD simulations by Pini et al. [53], and for turbomachinery design optimisation by Vitale et al. [78]. The SU2 flow solver is designed to solve the RANS equations in the form of

$$\frac{\delta \vec{B}}{\delta t} + \nabla \cdot F^c - \nabla \cdot F^v = Q \text{ in } \Omega,\ t > 0. \tag{3.1}$$

where $\vec{B}$ is the conservative variable vector, ie. $\vec{B} = \left\{\rho, \rho\vec{U}, \rho E\right\}^{\mathrm{T}}$. ρ is the fluid density, $\vec{U}$ is the fluid velocity vector in the Cartesian coordinate system, and E is the total energy by unit mass. The F terms in Eqn. 3.1 are the convective and viscous fluxes, and Q is a vector of source terms.

The convective and viscous fluxes from Eqn. 3.1 are represented as:

$$F^c = \begin{Bmatrix} \rho\vec{U} \\ \rho\vec{U} \times \vec{U} + \bar{I}p \\ \rho\vec{U}H \end{Bmatrix}, F^v = \begin{Bmatrix} \cdot \\ \bar{\tau} \\ \bar{\tau} \cdot \vec{U} + \kappa_{\text{tot}} \nabla T \end{Bmatrix} \tag{3.2}$$

with p as the static pressure, T as the temperature, H as the total enthalpy, and $\bar{I}$ representing an identity matrix. The viscous stress tensor, $\bar{\tau}$, is a function of the velocity derivatives and fluid viscosity, where μ is the laminar and λ is the turbulent component. The term κ_{tot} represents the total thermal conductivity, which contains a laminar and turbulent contribution. The laminar contribution is a fluid property, κ, while the Prandtl number, specific heat capacity at constant pressure c_p, and turbulent viscosity λ, are used to calculate the turbulent thermal conductivity.

Closing the RANS equations requires the transport, turbulence and thermodynamic models to be defined. A theoretical description is presented in Sec. 2.4. Two EoS available in SU2 to deal with non-ideal flows are the polytropic Van der Waals equation and the polytropic Peng-Robinson equation [53]. Polytropic indicates that the internal energy is dependent on the temperature, in a non-polytropic model instead the two are independent of each other. FluidProp can also be interfaced with SU2 to provide access to other more complex models. This program is a library of thermodynamic models for various fluids. Of interest for non ideal flows are the iPRSV and the multiparameter equations of state [17] for Siloxane MM, both are non-polytropic. The

latter is available from the RefProp library and it is considered the best approximation available with respect to the non-ideal thermodynamic behaviour of the fluid.

The division of the domain in cells which exchange mass, momentum and energy require the conservation equations to be discretized through a numerical scheme. Two of these are examined in this thesis: the ROE scheme and the Jameson-Schmidt-Turkel (JST) scheme. They are both suitable schemes for solving the Navier-Stokes and the Euler equations for compressible high-Reynolds flows. They can capture shocks in the flow. The ROE scheme was developed in 1981 by Philip Roe as an approximate solver of the Riemann problem [59], it is an upwind 1st order scheme. The only parameter that needs to be set in SU2 is the entropy fix coefficient which puts a lower bound on dissipation by limiting the minimum convective Eigenvalue to a fraction of the speed of sound. The Monotonic Upstream-centered Scheme for Conservation Laws (MUSCL) scheme [77] together with the Van Albada slope limiter is used to refine the solution. It offers increased accuracy in discontinuities such as shocks while keeping the solution free from the spurious oscillations typical of high order schemes. It allows upwind schemes to converge to 2nd order accuracy.

The JST scheme was developed in 1981 with the objective of being an efficient scheme for complex aerodynamics problems [39]. It is a central difference scheme. As a 2nd order scheme it should converge faster than an equivalent upwind scheme, but can be unstable at very high Reynolds. It does not require limiters and it includes a dissipation coefficient. In SU2 the second and fourth order dissipation coefficients can be chosen, the default and most commonly used values are 0.5 and 0.12, respectively.

This section has presented the many settings and submodels which must be selected to run the SU2 flow solver. To validate SU2 for modelling turbines in ORC systems it is necessary to subdivide the system and isolate the submodels, thermophysical, turbulence, numerical schemes and boundary conditions, and study them separately [51]. The hierarchy devised is presented in the next section.

3.2. Paradigmatic Validation Cases

To validate a complex model, a hierarchy of cases need to be defined. Starting from simple cases, where a single submodel is validated, it is possible to go up the hierarchy to more complex ones where also the interface between the components of the model can be assessed.

Figure 3.1 shows the hierarchy devised to validate the flow solver for the flow physics of an ORC turbine. The two main benchmark cases examined in this thesis are the de Laval nozzle and the cascade blade row. The first case includes a series of unit cases in which various expansions are run in a supersonic nozzle. This benchmark case was defined in order to assess the applicability and accuracy of the thermodynamic model in operating conditions where viscous effects are expected to be negligible. The most basic unit case is the supersonic inviscid isentropic expansion, the more complex ones add various types of shock phenomena. The second benchmark case, the cascade blade row, includes significant effects due to turbulence and interaction between shock waves. The case verified in this thesis is the supersonic flow through a 5-channel blade row, for which an initial assessment with direct response quantities will be performed. This case will allow the study of system response quantities important in engineering applications such as the efficiency. Future unit test cases which should be used to validate the flow solver include an optimized cascade and the flow through a rotor.

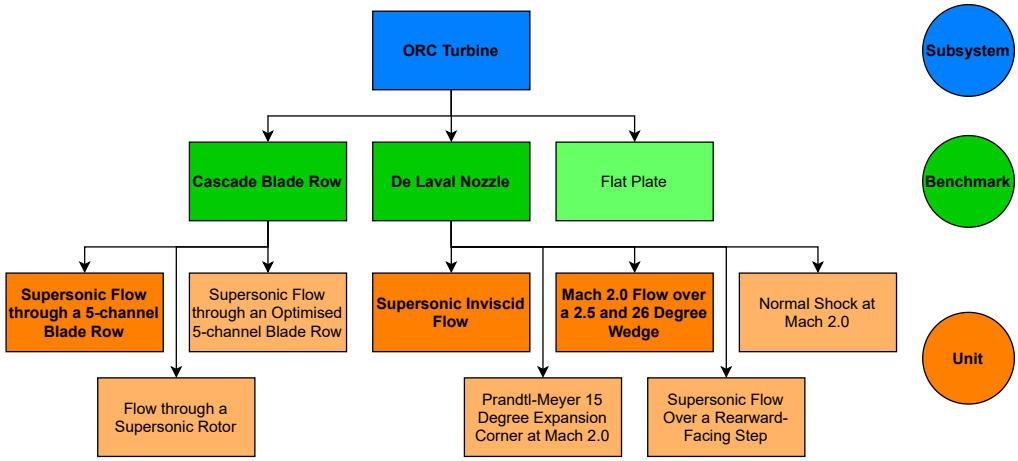

Figure 3.1: List of benchmark and unit cases envisioned to validate the flow solver for the prediction of the flow physics of an ORC turbine. The dark orange boxes represent the unit cases analysed in this thesis.

3.3. Applicability of the Thermodynamic Model

The section documents the procedure used to generate the operating maps which specifies the applicability range of different equations of state, including the effect of using polytropic and non-polytropic models, in the $T-s$ and the $P-T$ diagram and the main take-aways of the study.

Defining a set of operating conditions, shown graphically on a thermodynamic diagram, is critical for the validation exercises performed in this thesis. It is necessary to identify the region where the cubic equations of state differs considerably from reference models, such as the multiparameter ones, to choose the operating conditions for the experiments to be conducted. Using a cubic EoS in place of a multiparameter models is necessary since the latter are too computationally expensive for design of experiment studies and for use in design optimization studies. The assessment to determine the suitability of the thermodynamic model to close the conservation equations is done by means of gas dynamic experiments. This process constitutes a first step in the validation of a CFD software.

3.3.1. Procedure

This section presents the procedure used to compare the cubic equations of state to a reference model in order to determine their accuracy across a thermodynamic region. The reference model used is RefProp, this software has implemented a multi-parameter equation of state which is designed to provide a very accurate characterization of the thermodynamic behaviour even in highly non-linear conditions such as close to the critical point. An operating map will be generated to show the deviation of the density in the superheated region on the $T-s$ and the $P-T$ diagrams. The $P-T$ diagram is a less commonly used representation, partly because isentropes are no longer vertical lines. It has the advantage that both the pressure and the temperature, which are the usual boundary conditions in a CFD simulation, can be directly provided as input without any intermediate passage.

Figure 3.2 shows the procedure defined to calculate the deviation in the density. The process can be generalized to any EoS and for different thermodynamic properties, e.g., p, Z. Figure 3.2a presents the steps for the $T-s$ diagram case. A grid of temperature and entropy combinations, for a bounded region which is relevant for ORC applications, is made. The RefProp model receives the temperature and the entropy at each point of the grid and provides as output the density. Since the relation between the entropy and the thermodynamic properties differs for the various models considered, the entropy is first converted to the pressure of the point. The inputs provided to the cubic equation (StanMix) model are the temperature and the pressure calculate through RefProp, the output is the density. The density deviation between RefProp and the cubic model can then be calculated. For the $P-T$ representation, a grid of pressure and temperature combinations is prepared. Figure 3.2b shows the procedure used for this case, the two models receive as input the pressure and the temperature and provides as the output the density. The deviation between the two is then calculated.

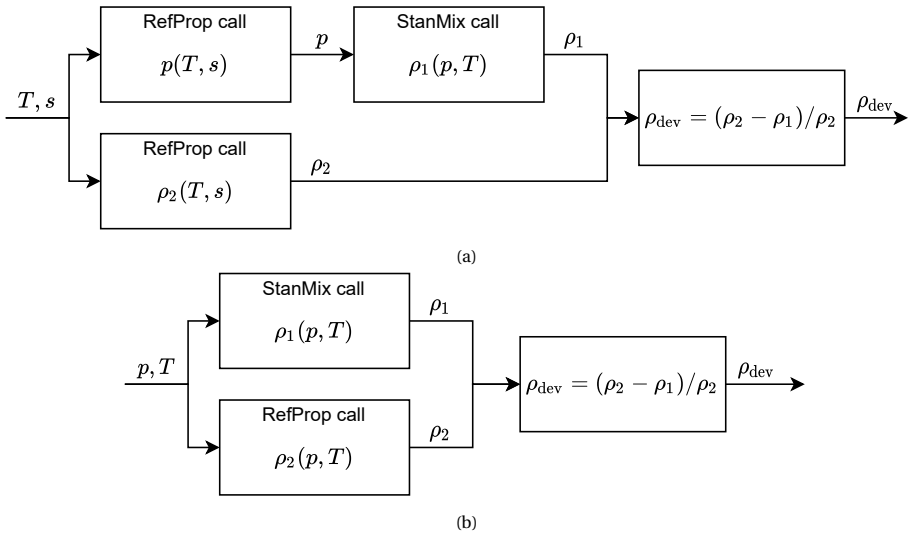

Figure 3.2: Procedure used to calculate the deviation in the density between the RefProp and the cubic (StanMix) models. **a)** $T-s$ diagram case. **b)** $P-T$ diagram case.

3.3.2. Operating Maps

In this section the predictions of density and speed of sound from two cubic EoS, the iPRSV and the Peng-Robinson EoS, will be compared against those resulting from RefProp. The cases chosen are presented in Tab. 3.1.

Table 3.1: List of EoS comparisons performed.

Case	**First Model**	**Second Model**
A	iPRSV (StanMix)	RefProp
B	Peng-Robinson (Ref. [6])	RefProp
C	iPRSV (StanMix)	Peng-Robinson (Ref. [6])

Figure 3.3 shows $T-s$ and $P-T$ thermodynamic charts with deviation contours of density. The deviations are calculated with the results from cases A, B and C. Figures 3.3a and 3.3b shows case A, the maximum deviation in the density is reached in the liquid and in the supercritical region close to the critical point, with a peak of around 20%, from there it decreases in all directions. In the vapour region, the maximum deviation is of 7%. The area just right of the vapour saturation line presents a very low deviation, this is probably due to the saturation line being chosen as the point of minimal error when the Peng-Robinson EoS was modelled. In the superheated region of the $P-T$ diagram, as the temperature is increased the mismatch become higher. The deviation is probably due to the different functional form of the equation used by RefProp and by the iPRSV EoS to describe the thermodynamic properties [73]. Case B was not shown graphically since the results were equivalent to the ones of case A. Considering the results of the density comparison, the cubic EoS are a suitable candidate to close the conservation equations.

Since the iPRSV EoS is an improvement of the Peng-Robinson EoS at the critical point region, the two were not expected to differ considerably. To verify this, case C was devised. The density comparison is plotted in Fig. 3.3c. As expected, the deviation between the two models is very low, no more than 0.1% in most of the thermodynamic region considered. The only exception is in the region adjacent of the critical point, where the deviation between the two reaches a peak slightly higher than 1%. The blue region around the saturation curve is non-physical and probably due to limitations in the Peng-Robinson EoS code [6]. Nonetheless, the predictions in the vapor region have been extensively verified and are the conditions of interest in this thesis.

To quantify the effect of using a polytropic and a non-polytropic model further studies were performed. A polytropic model uses a direct relation between the specific heat capacity and the temperature, while in a non-polytropic one the two are independent of each other. A property strongly influenced by this model choice is the speed of sound c, which is defined for a non-ideal gas as

$$c^2 = \gamma_{Pv} ZRT \tag{3.3}$$

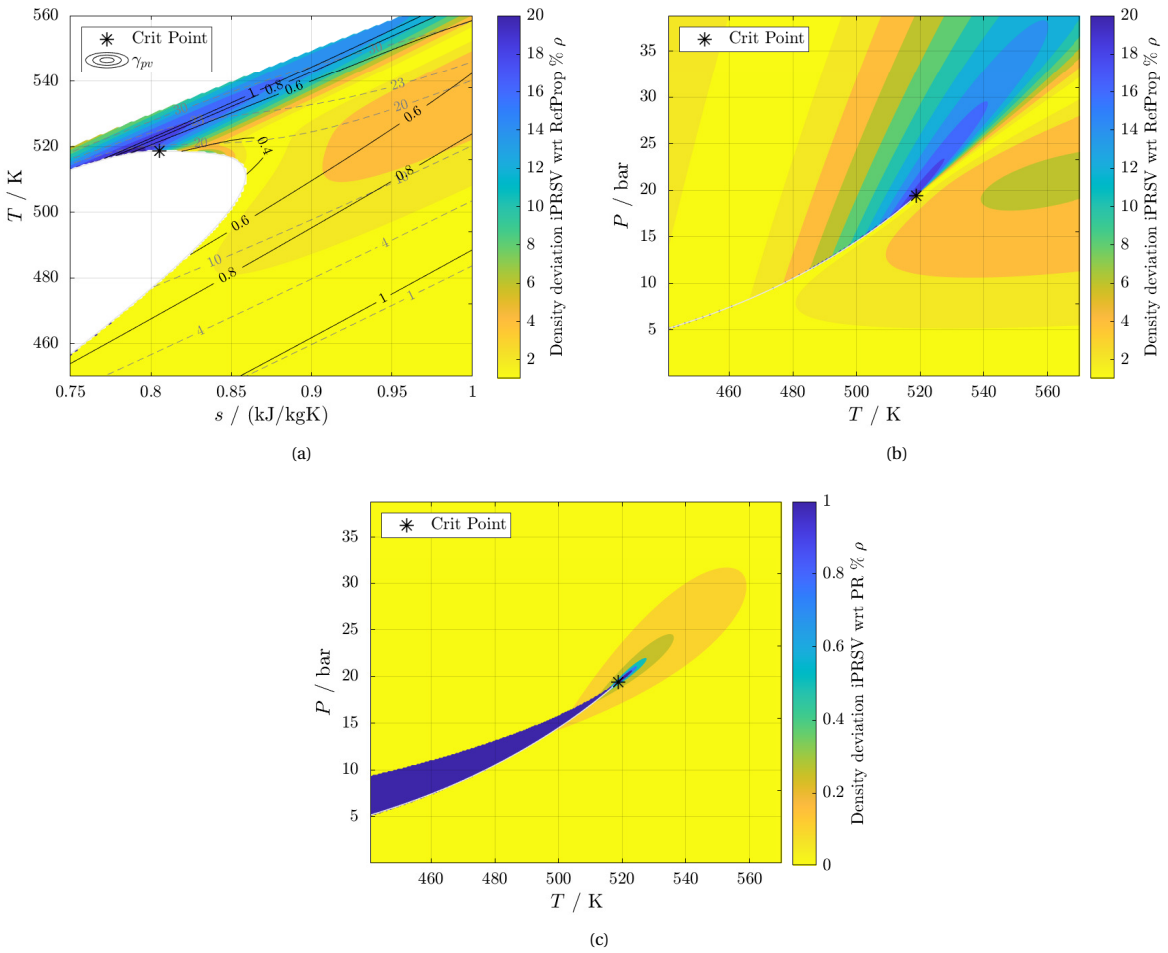

Figure 3.3: $T-s$ and $P-T$ diagrams showing the deviation in the density prediction of the iPRSV non-polytropic model with respect to the RefProp and the Peng-Robinson polytropic models for Siloxane MM. **a)** $T-s$ diagram showing the relative deviation of the density between the iPRSV and the RefProp models (Case A). **b)** $P-T$ diagram showing the relative deviation of the density between the iPRSV and the RefProp model. The two phase region is not present in a $P-T$ since the temperature remains constant during the phase transition (Case A). **c)** Deviation of the density between the iPRSV and Peng-Robinson model (Case C).

where γ_{Pv} is the pressure-volume isentropic exponent, defined as $\gamma_{Pv} = -\frac{v}{P}\frac{c_p}{c_v}\left(\frac{\partial P}{\partial v}\right)_T$. Case A and C were repeated, but comparing the speed of sound instead of the density. Figure 3.4 shows the deviation of non-polytropic iPRSV with Refprop and polytropic Peng-Robinson. Figure 3.4a shows case A, for the iPRSV with respect to RefProp a large deviation exists in the liquid and in the supercritical region, larger than the deviation in the density. Instead, in the vapour region the deviation remains below 5%, lower than the density deviation. Case B, the comparison between the Peng-Robinson and the RefProp model, was not plotted since it is almost a perfect match with the results of case A. Case C, shown in Fig. 3.4b, presents the comparison between iPRSV and the Peng-Robinson EoS that, similarly to the density case, indicates a low deviation across all the domain with the exception to the region of the critical point.

Considering Eqn. 3.3, R is constant for a fluid and T is a common input of the models, this leaves Z and γ_{Pv} as the only factors influencing the speed of sound. Z encompasses the deviation in density due to volumetric non-ideality, its impact should be low since both the iPRSV and the Peng-Robinson EoS are cubic. γ_{Pv} includes the specific heat capacity ratio and a factor to account for thermodynamic non-ideality, so it is dependent on the choice between a polytropic and a non-polytropic model. The results suggest that in the region considered, possibly because of the small range of temperatures considered, the specific heat capacity ratio does not vary considerably between the two models.

The main take-aways of the study are

- The largest density deviation between the RefProp model and the cubic equations of state compared,

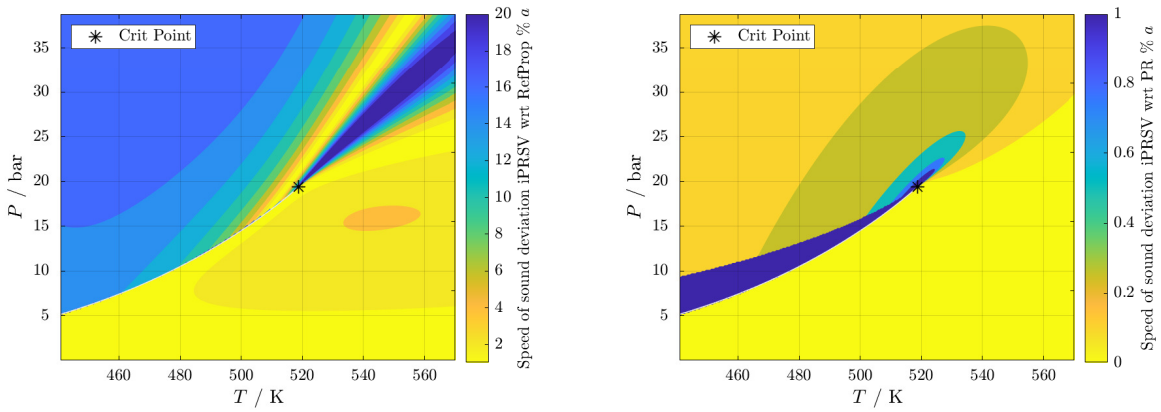

Figure 3.4: $P-T$ diagrams showing the deviation in the speed of sound prediction using the Peng-Robinson polytropic and the iPRSV non-polytropic models with respect to the RefProp model for Siloxane MM. **a)** $P-T$ diagram showing the relative deviation of the speed of sound between the iPRSV non-polytropic and the RefProp model (Case A). **b)** Deviation between the speed of sound of the iPRSV non-polytropic and of the Peng-Robinson polytropic EoS (Case C).

iPRSV non-polytropic and Peng-Robinson polytropic EoS, is in the liquid region;

- In the superheated region, the density deviation between the RefProp model and the cubic EoS does not exceed 7%;
- The density deviation between the iPRSV and the Peng-Robinson EoS only exceeds 1% around the critical point;
- The comparison of the speed of sound between the RefProp model and the iPRSV non-polytropic EoS shows a large deviation in the liquid and in the supercritical region, while in the superheated one the deviation is limited to 5%; and,
- The deviation of the speed of sound between the iPRSV non-polytropic and Peng-Robinson polytropic EoS indicates that the it is again less than 1% across the domain considered, with the exception of the points close to the critical point.

3.3.3. Choice of the Isentropes

Regions of interest in the thermodynamic diagrams have been identified. Two experiments which could be used to assess the accuracy of the thermodynamic model are the isentropic expansion and the shock wave generated in a de Laval nozzle, which are described in Chap. 4. Properties such as pressure, temperature and density, could be compared at every location of interest to determine the best suited thermodynamic model to be used in various thermodynamic states.

To define a suitable isentrope to run the experiments, the limitations of the test section must be taken into account. The operating envelope of the ORCHID is defined by four limits:

- Maximum evaporation pressure of 25 bar;
- Maximum evaporation temperature of 573.15 K;
- Maximum thermal power generated of 400 kWth; and,
- The two phase region, to avoid droplet formation.

At a pressure of 25 bar in the region close to the critical point, the isobars are at a much lower temperature than the temperature limit so the second constraint can be discarded. Considering that the value of Γ at a pressure of 22 bar is above one, which indicates a flow behaving ideally, this pressure represents a good choice for the inlet condition. To verify whether the thermal power required for a given condition can be supplied, Head [34] prepared a dedicated MATLAB code. He identified the four variables which needs to be

chosen to define a case: the total inlet pressure p_1, the total inlet temperature T_1, the outlet pressure p_2 and the throat area A_{th}. To determine the power requirement the following equation can be used

$$\dot{Q}_{in} = \dot{m}_{WF}(h_1 - h_8) \propto \dot{m}_{WF} h_1 = A_{th}\rho_{th} v_{th} h_1, \tag{3.4}$$

in which the throat area A_{th} is known and fixed, the density ρ_{th} and the speed of sound v_{th} at the throat can be calculated from the boundary conditions and the inlet enthalpy h_1 is proportional to the chosen inlet total temperature. At the inlet conditions the isobars are approximately flat, it is then possible to use the highest temperature which is expected to be reached at 25 bar, in this case 535 K, to determine the maximum expected power requirement. At that pressure and temperature the thermal power required is 250 kWth, enough to maintain a steady-state expansion.

The last limitation that needs to be considered is the distance from the two-phase region. This verification is necessary since two-phase expansions are outside the scope of this thesis and the experiments were not designed to be operated there. Since the uncertainty in the temperature is around 0.5 K, the safety margin adopted to avoid crossing the two phases region is 1 K. The expansion occurs along a specific isentrope, so it is necessary to transform the temperature margin in a horizontal shift to the right of the dome. To do so, the point at 22 bar isentropic with the right-most value of the dome is considered. Defined that point's temperature, it is possible to shift one degree Kelvin to the right. The safety distance is related to the inlet pressure since the isobars have a slightly different slope for a given temperature change. With an inlet pressure between 18 and 22 bar, the minimum entropy range is between 0.87 and 0.88 kJ/Kkg.

To keep the different expansions comparable the Volumetric flow Ratio (VR) is kept constant between the different experiments. The procedure to calculate VR and to define the boundary conditions of the simulations is described in App. D.2.

Table 3.2 lists a series of test cases which could be performed in the ORCHID test section. The design case, shown in Fig. 3.5, was chosen where the volumetric non-ideality was large and the deviation with respect to the RefProp model was the highest. Further experiments should be run left of the design case where the non-ideality increases further. Considering the design case of the nozzle, as the farthest isentrope of interest from the critical point, two series of test of interest are identified. The candidate isentropes are shown in Fig. 3.5. The first is a series of expansions with inlet pressure of 22 bar. At the inlet, Z is below 0.5, indicating a large volumetric non-ideality. Γ is above one at the inlet and it quickly decreases with the expansion, so the gas dynamic non-ideality would also be captured completely. The second region is the low pressure zone under the two phase region. The inlet pressure would follow the shape of the dome, since there a strong non-ideality is still present.

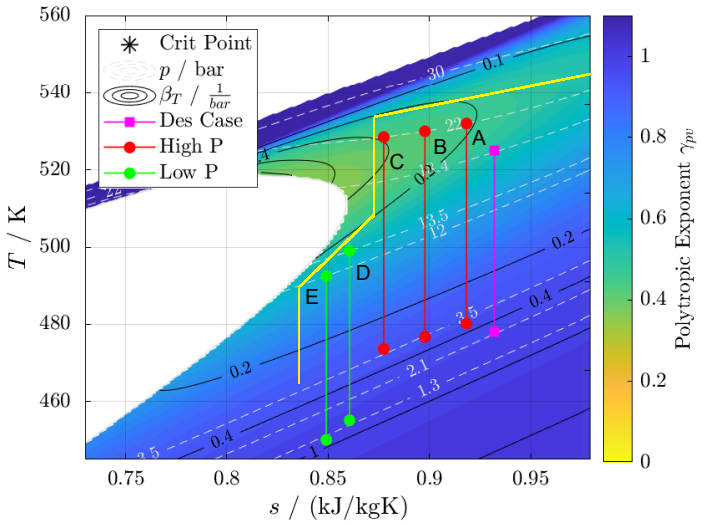

Figure 3.5: $T-s$ diagram showing the position of the high and low pressure candidate isentropes to be investigated and the design case of the nozzle. The yellow lines define the operating bounds of the ORCHID.

Together with the experiments, the isentropes defined in Tab. 3.2 should be simulated. Each case will be run both with RefProp and the Peng-Robinson equations using a common mesh and the same boundary conditions. This way the deviation of each property and the propagation of the error in an expansion can be

Table 3.2: Boundary conditions and location in the $T-s$ diagram of the isentropic expansions plotted in Fig. 3.5.

Case	Entropy	Inlet Total Pressure	Inlet Total Temperature	Outlet Static Pressure
Design case	0.932 kJ/kgK	18.4 bara	252°C	2.1 bara
A	0.918 kJ/kgK	22.0 bara	259°C	3.1 bara
B	0.898 kJ/kgK	22.0 bara	257°C	3.4 bara
C	0.877 kJ/kgK	22.0 bara	255°C	3.8 bara
D	0.861 kJ/kgK	13.5 bara	226°C	1.4 bara
E	0.849 kJ/kgK	12.0 bara	219°C	1.2 bara

studied. The pressure, temperature and density could be compared. Subsequently, a plot of the error with respect to the temperature can be made to show the deviation. Figure 3.6 shows an example made with the Van der Waals EoS in place of RefProp to show how the results could be visualized. The deviation is plotted against the temperature instead of the x-coordinate because this allows for a better correspondence with the position in the $T-s$ diagram and because the initial and the final part of the nozzle are mostly uniform in properties.

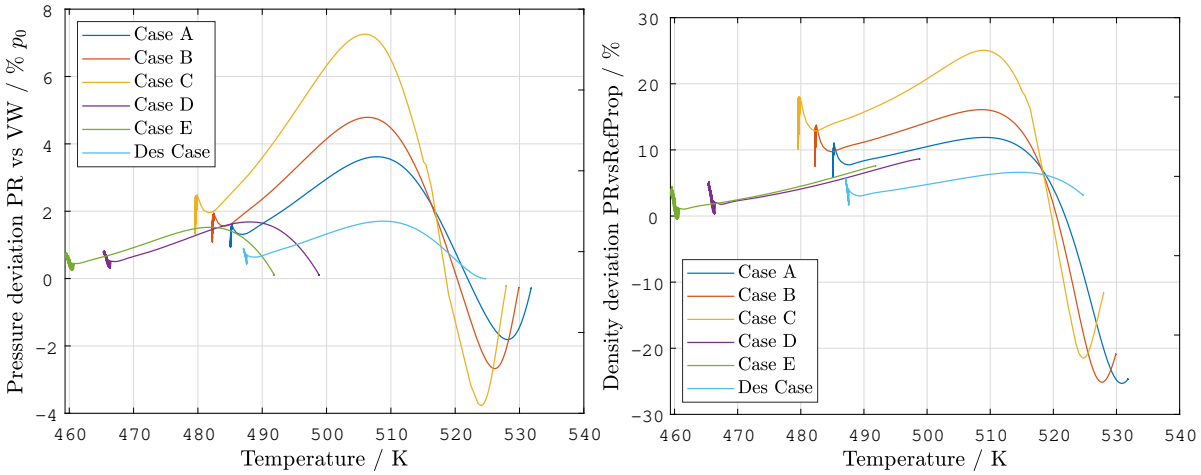

Figure 3.6: Proof of concept with pseudo-experimental data (Van der Waals (VW) EoS used in place of RefProp) showing how the pressure and the density deviation between SU2 with LUT and SU2 with the Peng-Robinson EoS can be visualized. In the X-axis the temperature is used since it can more easily be translated to the corresponding isentrope in the $T-s$ diagram. **a)** The deviation of the pressure along the nozzle is plotted for the five isentropes of Fig. 3.5. **b)** The deviation of the density along the nozzle is plotted for the five isentropes of Fig. 3.5.

3.4. Validation Method and Uncertainty Characterisation

This section describes how the validation study for the SU2 flow solver for one case was done. The method is based on the ASME V&V20 'Standard for Verification and Validation in Computational Fluid Dynamics and Heat Transfer' and supplemented with established statistical methods to determine the uncertainty of a CFD simulation, both due to numerical methods and variable model inputs. The final determination of validity for the SU2 solver was determined using the metric defined in the ASME V&V 20 [5] method which was described in Sec. 2.6.3.

3.4.1. Numerical Uncertainty

The numerical portion of the simulation uncertainty, u_{num}, encompasses all the approximations which must be made during a computational assessment; this includes approximations in the discretisation, truncation, and iteration of a simulation. Discretisation uncertainty arises since discrete value must be assigned to each cell in a mesh even though in true physics the value may be continuous over the domain. Truncation is the removal of digits at the end of a number due to the bit limit in a computer, and iteration refers to uncertainty from taking a solution from an iterative process which may not be converged to the final solution.

The iteration and discretisation uncertainties in this study was calculated using Richardson Extrapolation as described by Eça and Hoekstra [25]. This method uses the solutions of the same simulation over sequentially finer grids to approximate the total uncertainty level due to discrete errors at a given grid density. This process has been automated with a tool from ReFRESCO [43] which required the input of simulation results and provided the approximate uncertainties of each output variable through use of the method proposed by Eça and Hoekstra [25].

This tool requires a minimum of four grids. Both structured and unstructured grid can be compared. An advantage of using a structured grid is that it is possible to iteratively halve the cell size to increase the mesh density. For an unstructured one each mesh region should be proportionally scaled with the same value when generating the mesh. A requirement of the tool is that the round-off and iterative error are negligible with respect to the discretization error. The first can be considered insignificant since double precision is used. The latter assumption is verified in Sec. 4.3.4 and 5.3.3.

3.4.2. Forward Propagation of Input Uncertainty

The input portion of simulation uncertainty, u_{in}, is the result of input parameter uncertainties being forward propagated through the model to the outputs. Constant values in the simulation, for example boundary conditions or fluid properties, are not exact. The boundary conditions and closure coefficients of the thermodynamic sub-models are determined through experimentation where there are uncertainties in the measurements over time, and instruments have limited resolutions. Any possible change in the model inputs will have an impact on the final model responses. Evaluating the value of forward propagated input uncertainty can be done in a structured fashion through the Monte Carlo method. In this type of study the input at each iteration are chosen randomly within the provided uncertainty range. It provides optimal results when a very large number of iterations are run. There are more efficient methods which have been established for NICFD. Cinnella et al. [13, 14] have used stochastic collocation (SC) uncertainty quantification techniques to establish the uncertainty of dense organic gas flows. Additional methods created for NICFD solvers in ORC component design have been presented by Congedo [19].

In stochastic collocation (SC) a surrogate model which has the same statistical behaviour of the outputs of the real model is created. This allows for faster computations of the output system response quantities. The concept of stochastic expansion methods is that a PDF of any shape can be represented as a series of polynomials, similar to how any function can be represented by a Taylor series. Notably, the coefficients of the polynomial indicate the statistical moments. The first coefficient is the mean, the second coefficient is the standard deviation, and the third is the skewness of the output variable [47]. The surrogate model is constructed by taking a set of samples from the original model, and evaluating the statistical moments of the input parameters. Once the surrogate is constructed it can be sampled thousands of times and solved at the speed of a simple polynomial. The sampling of the original model is based on quadrature methods.

To represent this mathematically consider the stochastic differential equation:

$$L(\mathbf{x}, \theta, \phi) = f(x, \theta), \tag{3.5}$$

where L is a non linear spatial differential operator which depends on a random vector θ (whose dimension depends on the number of uncertain parameters in the problem) and ϕ represents the solution of the function. $f(x,\theta)$ is a source term depending on the position vector $\mathbf{x}$ and on the θ.

The stochastic process can be approximated as a spectral expansion through a series of polynomials. ϕ can be expressed as

$$\phi(\mathbf{x}, \theta) = \sum_{i=0}^{\infty} \phi_i(\mathbf{x}, t)\Psi_i(\xi(\theta)), \tag{3.6}$$

where the factor $\phi_i(\mathbf{x}, t)$ represent the deterministic part and $\Psi_i(\xi(\theta))$ the stochastic one. In practice the infinite sum is truncated up to a certain order. The polynomial can then be substituted in the initial stochastic differential equation. The two classes of surrogate model used are the Polynomial Chaos Expansion and the Stochastic Collocation. They differ in relation to the type of interpolation used, with the latter using multidimensional Lagrange interpolation polynomials.

The mean and standard deviation of the model output is thus as follows:

$$\mu_\phi(\mathbf{x}) = \phi_0(\mathbf{x}) \tag{3.7}$$

$$\sigma_{\phi}^{2}(\mathbf{x}) = \sum_{i=1}^{N} \phi_{i}^{2}(\mathbf{x}) \left\langle \Psi^{2} \right\rangle \tag{3.8}$$

From the results of the stochastic collocation study the input uncertainty is calculated through:

$$U_{\text{in}} = 2\sigma \tag{3.9}$$

In addition to quantifying the magnitude of output uncertainty, the relative importance of each uncertain model input parameter is also useful for validation analysis. The relative importance of input uncertainties can be identified using a variance based decomposition (VBD) sensitivity study, or extracted from the results of a SC. The sensitivity of a parameter in this thesis is represented by the Sobol Index, where each index is the variation of the system response due to the variation of the input parameter of interest, divided by the total variation of the system response. The primary sobol index,

$$S_i = \frac{\text{Var}_{x_i}[E(Y|_{x_i})]}{\text{Var}(Y)}, \tag{3.10}$$

where $\text{Var}_{x_i}[E(Y \mid x_i)]$ is the conditional probability that the variance is due to the x_i input and $\text{Var}(Y)$ is the total variance, represents the effect of an input parameter independently of all other parameters. The total sobol index

$$T_i = \frac{\text{Var}(Y) - \text{Var}[E(Y|_{x_{-i}})]}{\text{Var}(Y)}, \tag{3.11}$$

where $x_{-i} = (x_1, \ldots, x_{i-1}, x_{i+1}, \ldots, x_m)$, represents the effect of an input parameter independently and in combination with other parameters. A value of one in a Sobol index indicates that the parameter is the only one which influences the system output, while a value of zero implies no effect of the parameter uncertainty on the variation of the system response. For a well converged UQ, the sum of the primary Sobol numbers is equal to one, while for the total Sobol numbers the sum is always more than one, the only exception is if the system input are additive, in that case there are no interactions and the sum is equal to one [37].

3.4.3. Computational framework for UQ studies

The implemented method to calculate the SU2 flow solver output uncertainty is a third order SC method with Smolyak sparse grid sampling, done using Dakota [1] on a Linux operating system. These programs are wrapped within a series of Python and MATLAB scripts, written by Bills [9], to interface them with the SU2 simulations and results. Figure 3.7 presents a top level flow chart of the input uncertainty calculation infrastructure [9, Pg. 43].

Python is used as the interfacing language between Dakota and SU2 with calls to a MATLAB shock wave calculator developed by Head et al. [33], Iyer [38]. It is based on the jump conditions for a steady shock wave. The code is developed especially for SU2 in Linux and can be reused to asses the uncertainty of different test cases. The code also provides Sobol indices for the responses of interest to identify the sources of uncertainty.

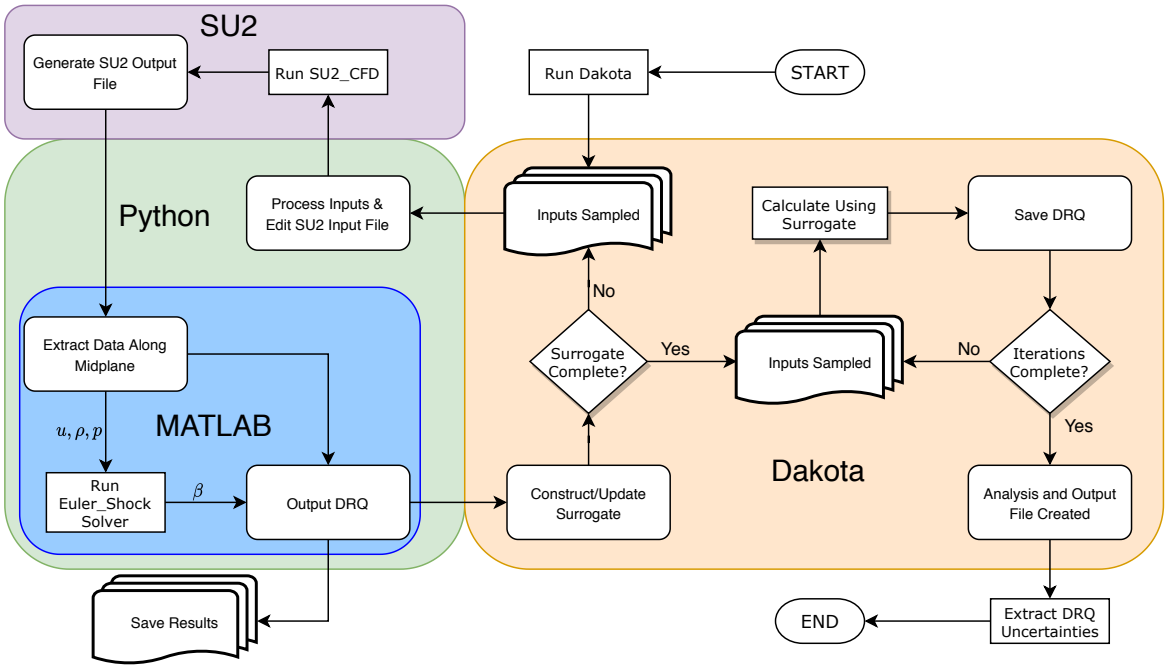

Figure 3.7: Applied framework to implement a sparse grid stochastic collocation UQ for SU2. The code, implemented in Linux, accepts PDFs of SU2 model inputs and evaluates the uncertainties of the DRQ along with the Sobol indices for the given configuration of SU2. Taken from Bills [9].

4

Validation of the SU2 Flow Solver for Non-ideal compressible flows

In this chapter several of the paradigmatic unit cases defined in Chap. 3 are used to validate the SU2 flow solver. This study will verify the suitability of the thermodynamic model to close the conservation equations. A de Laval nozzle was chosen as the most simple benchmark component to facilitate various unit test cases for the validation exercise. It is the most suitable because it allows to decouple the influence of the solver's submodels; namely, thermodynamic, turbulence, and transport submodels on the flow physics. Cases that can isolate the core flow of the nozzle, which can be considered adiabatic and inviscid, are candidate experiments to determine the most suitable candidate thermodynamic model to close the conservation equations and to subsequently validate the flow solver. The following four direct response quantities were chosen to facilitate the validation: the static pressure at the nozzle upper and lower walls, the Mach number at the center line, the shock wave angle generated by a wedge and the mass flow rate.

In the first section the validation hierarchy for the de Laval nozzle is presented. In Sec. 4.2, the test case and the response quantities are defined. In Sec. 4.3 the thermodynamic model and the numerical scheme will be chosen. The assumptions used will also be verified. The mesh generation and the choice of the convergence threshold are presented in Sec. 4.3.3 and 4.3.4. The characterization of the uncertainties is described in Sec. 4.4. The experimental procedure, the operating conditions and the data gathered in the experiments are presented in Sec. 4.5, 4.6 and 4.7. Finally, the validation assessment is performed in Sec. 4.8.

4.1. Validation Hierarchy

A selection of cases to be executed in the nozzle is presented in Fig. 4.1. They were chosen from the *NPARC Alliance Verification and Validation Archive* [64] by NASA as the most relevant cases which can be performed in a de Laval nozzle. Together, these cases allow the inviscid expansion and various shock phenomena to be characterized independently. This will pave the way for benchmark level cases, such as a blade cascade, to be executed.

The two cases which will be described in this chapter are the supersonic inviscid flow expansion and the generation of a shock wave with a 2.5 degree wedge. The first case aims at assessing the flow of inviscid, non-heat-conducting siloxane through a converging-diverging nozzle. The second aims at verifying the code ability to capture shock waves. Generation of shocks within an isentropic flow presents an interesting test case because shock phenomena are sensitive to perturbations in the model inputs. The other three cases, to be run in the future, aim at verifying flow behaviour in the presence of: a steady normal shock wave, a Prandtl-Meyer expansion and a rearward-facing step.

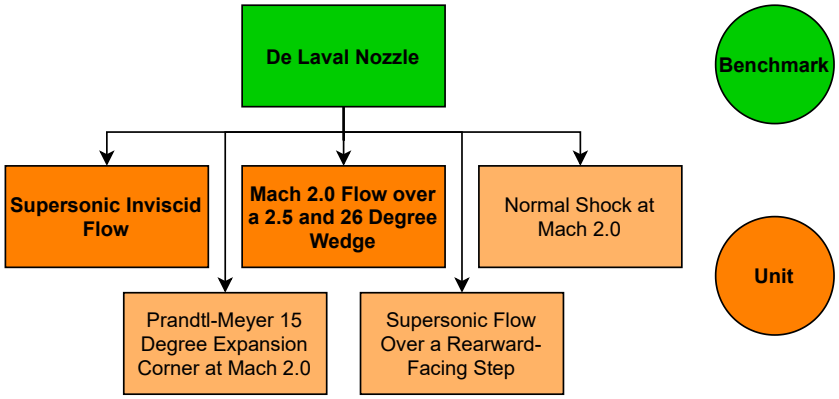

Figure 4.1: List of unit cases envisioned to assess flow in the de Laval nozzle. The dark orange boxes represent the unit cases analysed in this thesis.

4.2. Design of Experiments

The validation method here described stems from the solver validation procedure defined in Chap. 3. Looking at Fig. 4.1, the two experiments to be performed are both unit tests. The former consists in an isentropic expansion in a nozzle, the latter, in addition to the expansion, includes a shock waves generated by a wedge. They are aimed at assessing the Peng-Robinson equation of state implementation in SU2. To experimentally represent these flows the ORCHID nozzle test section is used.

4.2.1. Test Section

The nozzle is designed to accelerate a flow of siloxane MM at the conditions presented in Tab. 4.1. The inlet conditions of the fluid correspond to a compressibility factor of $Z = 0.58$ and the design outlet Mach number is 2.0. The rectangular cross section nozzle is 86 mm long with a throat height of 7.5 mm and a constant width of 20 mm. See Fig. 4.3 for an illustration of the nozzle geometry.

Table 4.1: Design conditions of the nozzle.

Condition	**Value**
Inlet Total Pressure	18.40 bara
Inlet Total Temperature	252°C
Outlet Static Pressure	2.10 bara

The flow in the divergent part of supersonic nozzle presents different zones of interest. The features are highlighted in Fig. 4.2. The area after the throat, where the top wall curvature is positive, is the kernel region. There the expansion waves are approximately orthogonal with respect to the flow direction. After the curvature becomes negative, the reflex region begins. Finally, if the nozzle is symmetric, when the opposite waves meet they cancel each other out and the uniform zone begins, there the flow properties no longer varies and the flow is free of waves.

When in use, the wedge is positioned at the outlet, as shown in Fig. 4.3. This choice was made because, even though the flow is ideal in that region, the shock wave angle is sensitive to the model input properties. Furthermore, in that location the jump conditions requirement for the flow to be uniform is respected. Finally, by placing the wedge at the outlet, the risk of blockage is decreased.

4.2.2. Response Quantities

The flow response quantities compared in the isentropic expansion are extracted in two regions: at the nozzle wall and at the center line. The properties extracted only at the center line are: 1. the Mach number, 2. the expansion wave angles, 3. γ_{pv} and 4. the shock wave angles. The responses extracted both at the wall and at the center line are: 1. the static pressure, 2. the density, 3. the temperature and 4. the x-velocity. In addition to these, the mass flow rate is also calculated at the throat using the mass conservation equation and assuming 1D flow. Velocity, density and area are extracted at the throat mid-plane and multiplied together

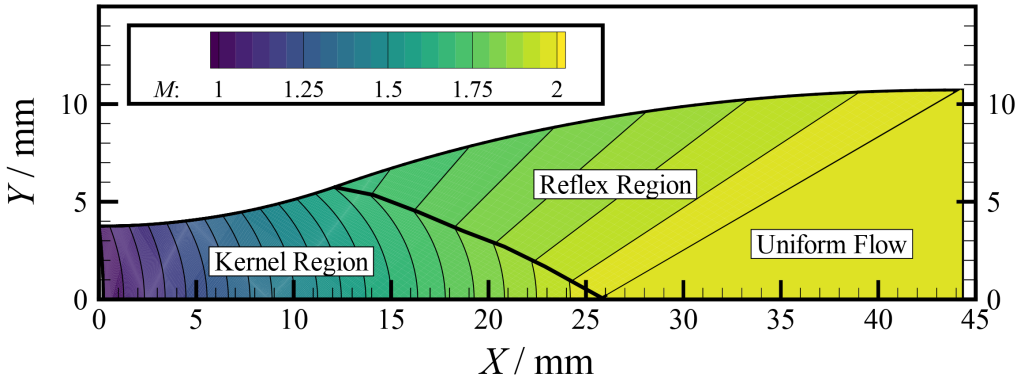

Figure 4.2: Location of kernel, reflex and uniform region along a convergent-divergent nozzle for the boundary conditions listed in Tab. 4.1. The design Mach number of the nozzle is 2.1. Taken from Head [34].

$$\dot{m} = \rho \cdot A \cdot u. \tag{4.1}$$

A verification of this method with respect to the integration of the momentum along a plane is presented in App. B.

All the flow quantities are extracted at 15 measuring stations which coincide with the position of the pressure taps in the ORCHID. The exceptions are the expansion wave angles, which are extracted at 100 linearly spaced locations between the throat and the outlet, and the shock wave angles, which are calculated at the outlet. Most of these properties are recorded for future reference since the respective experimental data cannot be generated at the moment.

Currently, by gathering experimental data, the comparison can be performed for: 1. the static pressure at the wall, 2. the Mach number, 3. the shock wave angles and 4. the mass flow rate. In the future it is planned to implement a tool to also extract the density from the experiments through backwards orientated schlieren imaging [34] and chromatic confocal imaging. The static pressure is extracted at 15 different locations, positioned at both the top and bottom side of the nozzle. Three points are symmetrically located on both walls at the inlet, the throat and the outlet of the nozzle. Figure 4.3 shows the location of the taps along the nozzle wall. The pressure is recorded for an extended period of time when steady-state is achieved to record both the average and the standard deviation.

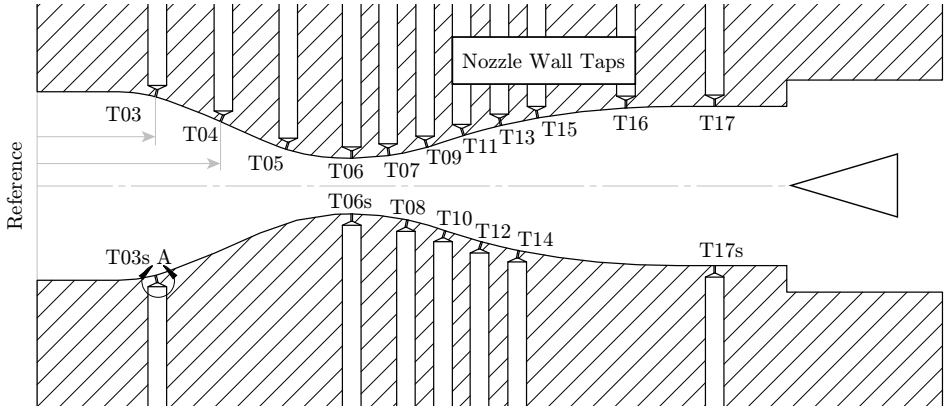

Figure 4.3: Location of the taps along the nozzle and position of the wedge. The inlet height is of 25.4 mm, the throat is 7.5 mm and the outlet is 21.4 mm high. Adapted from Head [34].

The Mach number is calculated from the expansion wave angles, which are extracted through schlieren imaging. With fluids such as air it is usually not possible to record Mach waves at the resolution required to perform a validation, with siloxane instead it is feasible to do so since the dense vapours experience a large change in density during the expansion. A detailed explanation of the process is presented in Sec. 4.5. From a dataset of pictures the average and the uncertainty of the angle of all the expansion waves can be calculated.

The uncertainty on the angle position is also estimated, since the pixels are discrete in space and the wave is often as thin as a single pixel. The results can either be interpolated and compared directly to the Mach angle calculated through the simulations or they can be converted to the equivalent Mach number. The two properties are directly related for an ideal gas, $\mu = \arcsin 1/M$. Finally, the mass flow rate is measured by a dedicated sensor. To calculate γ_{pv} at the center line the following formula is used

$$\gamma_{\mathrm{pv}} = \frac{\rho \cdot u^2}{p \cdot M^2}. \tag{4.2}$$

When the shock wave generator is present, the response quantity studied is the angle of the shock. For this scope several wedge angles were used. The numerical shock waves were not generated with the use of a dedicated mesh, instead the jump conditions were solved from the properties of the uniform region at the clean nozzle outlet. This was done to avoid convergence problems due to the presence of the shock wave and to remove the numerical uncertainty deriving from the mesh discretization. The latter is particularly important since the gradient of the properties through a shock wave is large, so an increase in the mesh density is required at the shock wave location.

The code used to solve the jump conditions follows the procedure proposed by Grossman [30], which is presented in App. D.1. From the converged solution, a point at the center line in the uniform region close to the outlet is chosen. There, the Mach number, the pressure, the density and the velocity are recorded. A series of vectors are then defined, one containing the wedge angles chosen and two with the upper and lower limits of the range of density ratios between before and after the shock wave. Through the preferred thermodynamic model, the enthalpy before the shock wave is calculated. At this point it is possible to calculate the properties after the shock wave. The jump conditions with the density ratio guesses are solved both with $h_2 = h_1 + \left(V_{\mathrm{n}1}^2/2\right)\left(1-\nu^2\right)$ and $\tilde{h}_2 = h\left(p_2, \rho_2\right)$. For the second case, the enthalpy is calculated with the chosen thermodynamic model provided the pressure and the density calculated with the jump conditions. It is then necessary to minimize the difference between the two results. When the density ratio which minimizes the difference between the two results is found, the β angle associated with the input θ angle can be calculated with the following equation

$$\tan\beta = \frac{(1-\nu) \pm \left[(1-\nu)^2 - 4\nu\tan^2\theta\right]^{1/2}}{2\nu\tan\theta}. \tag{4.3}$$

A final check to make sure that the resultant shock is not a strong one is performed. This can be easily done by verifying whether the Mach number after the shock is below one.

4.3. Model Definition

A critical step of any CFD simulation is the generation of a mesh which can accurately capture the flow features of interest. This is an important part of the procedure since it directly affects the numerical uncertainty. The objective is to define a mesh which is an optimal trade-off between the numerical uncertainty due to the mesh quality and the computational cost. Subsequently, a convergence threshold which minimizes the iterative error will be defined.

Solving numerical problems requires simplification with respect to the real case to make the problem tractable. The main assumptions and choices made in this study are: the limited influence of 3D and viscous effects on the response quantities, the choice of the thermodynamic model and the choice of the numerical scheme. A verification of the accuracy of the jump condition solver in predicting the shock wave angle is also made.

4.3.1. Thermodynamic Model

SU2 v. 5.0 allows the choice between the ideal gas, the Van der Waals polytropic and the Peng-Robinson polytropic thermodynamic models. In the deprecated version 3.2.8.3 FluidProp was also connected, this allowed the models implemented to be called, including RefProp and StanMix for the iPRSV. Bills [9] compared the result of an Euler simulation with the Peng-Robinson equation of state (EoS) to a RANS simulation with the iPRSV EoS. He compared the pressure at the wall and the Mach number at the center line, his conclusion was that the differences between the models were minimal for these flow quantities. This conclusion is supported by the operating map presented in Sec. 3.3.2, there the difference between the Peng-Robinson and the iPRSV EoS was found to be minimal. From these considerations and since it is not currently available, only the Peng-Robinson EoS will be used in the validation. In the future FluidProp should be connected again to

the latest version of SU2, at that point a comparison with RefProp could be done to verify whether significant differences arise.

4.3.2. Simulation Set-Up

The simulations were computed using the SU2 v. 5.0. This is the open source CFD software which needs to be validated for NICFD flows. The software does not have an interface, it just needs a configuration file with the case settings and a mesh, which will be described in Sec. 4.3.3. Viscosity is not expected to influence the flow quantities studied, so the simulations were run with a CFD model based on the Euler equations. This claim will be verified in Sec. 4.3.5. The thermophysical properties are computed with the Peng-Robinson model. The advective fluxes are discretized by using the second-order accurate ROE with MUSCL scheme. The total conditions are provided at the inlet, and the static pressure at the outlet. The boundary conditions are of Riemann type. The values provided at the boundaries are the design condition presented in Tab. 4.1. Since the flow is symmetric, only half of the domain is simulated. The centre boundary has a symmetry condition. The top wall is inviscid and adiabatic. The set-up of the stochastic simulation will be presented later on in Sec. 4.4.3. The remaining sub-models, such as the transport one, are provided in the complete configuration file in App. A.1.

4.3.3. Mesh Convergence Study

Choosing a suitable mesh is a critical part of the validation process since an inadequate one will produce inaccurate results. The uncertainty quantification process requires a large number of iterations, so it is necessary to balance the accuracy of the results with the computational cost required to run the cases. In his validation effort, Bills [9] used a uniform mesh made of 10k elements. He noticed that with this mesh quality a large numerical uncertainty for the pressure was present in a few points along the nozzle: close to the throat, along the kernel transition line and in the outlet region. The location of these uncertainties coincide with the position of expansion waves and weak shock waves, this indicates that the numerical uncertainty is present because of the steep gradients of properties which cannot be fully captured by the mesh used. For this reason, he recommended the use of an improved grid in futures studies.

A uniform mesh which represented a balance between computational cost and deviation was chosen. Figure 4.4 shows the relation between the RMS deviation and the number of elements in the mesh. The time to convergence tends to increase linearly as the number of elements increases. The Root mean square (RMS) deviation instead initially decreases exponentially, until it plateaus starting from around 40k elements. With the power currently available, the choice made was to increase the mesh density to 40k elements since further increases would lead to limited gains in the accuracy with respect to the required time-cost increase.

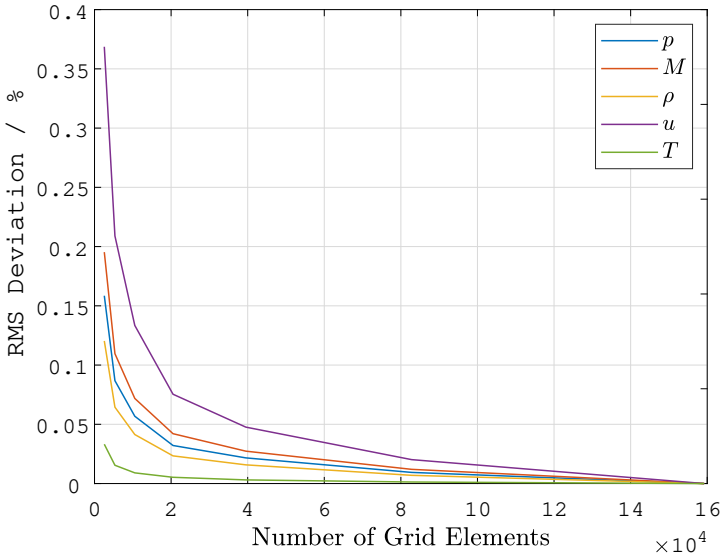

Figure 4.4: Relation between the mesh density and the root mean square of the deviation with respect to the finest mesh for various response quantities.

The influence of the mesh density was also analysed when performing the UQ study, which is defined in

Sec. 4.4.3. The uncertainty propagated from the inputs is insensitive to increases in the mesh density. This change can be considered positive, since it proves that the uncertainty due to the inputs is independent of the mesh density. This result corroborates the finding of Bills [9] and it is not presented in the thesis.

4.3.4. Convergence Threshold

A component of the numerical error is the iterative error. It is often ignored, since it is assumed to be at least one order of magnitude lower than the discretization error. The relevance of the iterative error grows as a finer mesh is used [23]. Since in this study the mesh is denser than in the previous studies, a convergence threshold to limit the iterative error will be defined.

The full theoretical treatment can be found in Eça's papers [23–25]. An implementation of the method was also performed by Liebrand [40], this will be used as the inspiration for the presentation of the results. The procedure devised consists in comparing the value of a property for different residuals thresholds and for different mesh densities. An acceptable iterative error can then be defined in relation to the convergence of the response quantities and the number of iterations required to reach it.

Residuals are commonly used to determine whether convergence is achieved. They are convenient because it is not computationally expensive to calculate them. Unfortunately, they only provide an approximation of the deviation trend. If the convergence history of a response quantity has to be determined, the solution must be computed several times. A script was developed to run a simulation and to calculate the solution at each threshold chosen to then save the property value. The SU2 simulation then restarts from that point until convergence is achieved. The result file can then be used to investigate the convergence trend of each variable at any point of the mesh. For this study, the values are extracted at some specific residual levels, between 10^{-6} and 10^{-13}. The residual considered is rho. The case used in the analysis is the isentropic expansion in a de Laval nozzle. The points for which the comparison is made are positioned at 0.0250 m and 0.1000 m from the inlet of the nozzle. They were chosen to sample both the convergent and the divergent section of the nozzle. Two meshes, with 10k and 40k elements, are compared.

The results are presented in Fig. 4.5. Figure 4.5a shows the Mach number trend of two points in the 40k elements mesh, together with the normalized number of iterations with respect to the lowest residual level. Since the convergence trend of the two meshes is similar, only the denser one is plotted. The main difference between the two is the slightly lower convergence speed of the 40k elements one. It can be seen that the deviation decreases logarithmically. From residual 10^{-9}, both points have reached a value which remain roughly constant. Since the change between different iterations quickly become indistinguishable, the logarithmic deviation between subsequent iterations was plotted in Fig. 4.5b. The trend is close for both points examined. From residual equal to 10^{-12}, the machine accuracy used is reached and no further changes occur.

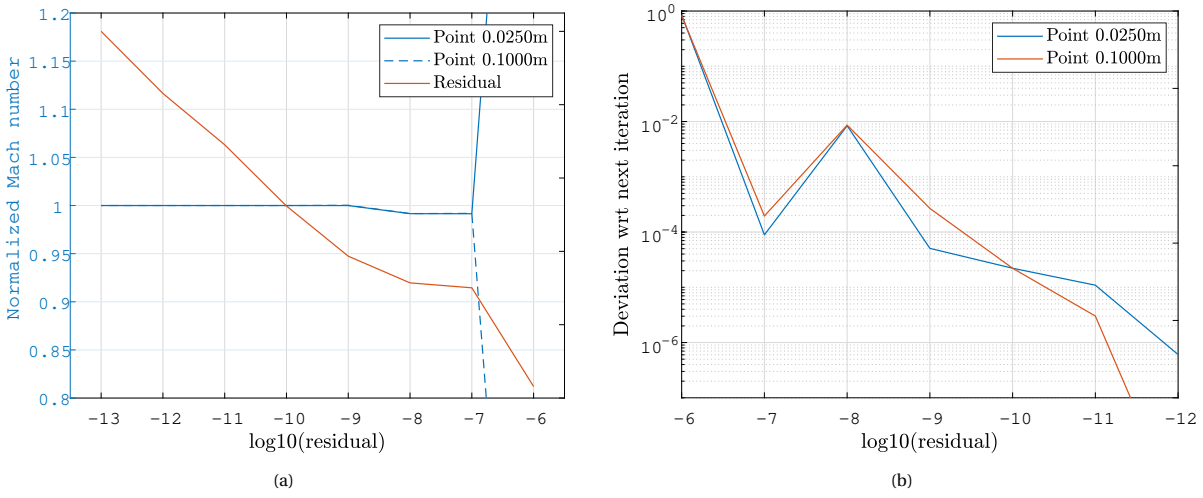

(a) (b)

Figure 4.5: Relation between the residual, the number of iterations and the Mach number for two points in the nozzle. **a)** Evolution of the normalized Mach number with respect to the residual for two points for the 40k elements mesh. **b)** Mach number deviation with respect to the next residual considered, for the 40k elements mesh.

From this data it can be concluded that with a residual equal to 10^{-13}, which is the threshold currently

used, the iterative deviation is minimal or absent, both with the coarse and the fine meshes. Nonetheless, when it is necessary to limit the number of iterations, the results suggest that it is possible to stop at lower residual levels. A comparison with the converged solution of the 160k elements mesh confirmed the results. It showed that the deviation is in the order of 10^{-4}, indicating that the deviation due to the mesh is orders of magnitude higher than the iterative one, so, in accordance with Eça and Hoekstra [24], it can be considered negligible. Recommendations for future studies include the suggestion to evaluate the relation between the deviation of a property and the residuals to make a trade-off with the computational cost required, as presented here. If possible, a bulk quantity should be used, since it is representative of the complete flow instead of a few specific points. Furthermore, in Eça and Hoekstra [25] a detailed strategy is presented to determine how the deviation due to the grid and the convergence change, which allows to more easily understand which mesh and residual threshold should be used to limit the uncertainty.

4.3.5. 3D and Viscous Effects

In the validation campaign, it is assumed that 3D and viscous effects have a negligible influence on the direct response quantities (DRQ). The first assumption is made since the test section has a constant width of 20 mm over all its length. It is necessary to use a 2D domain since the number of elements of the complete model would be too large to conduct stochastic simulations. The second assumption is considered since the short length of the nozzle would prevent a boundary layer to grow and have an influence on the properties measured at the mid-plane. Using the RANS equations would be more computationally expensive than using the Euler ones, and it would require a very dense mesh close to the walls.

To verify whether these assumptions are acceptable a comparison between a 3D RANS, a 2D RANS and a 2D Euler simulations of the nozzle were made. The comparison was performed only for deterministic results, no UQ analysis was done due to the large computational power required. The boundary conditions are the same for all cases and they are the design one.

For the 3D case, an unstructured mesh with boundary layers was created in ICEM. Following a mesh convergence study a final element count of 5 million was selected. However, the property variations close to the throat should be investigated in the future because there were some noticeable convergence issues. The turbulence model used was the SA. For the 2D RANS simulation the same parameters were used. The number of elements in this case were 45k, with 25 prism layers to capture the physics in the boundary layer. Its total thickness was constant and equal to 0.15 mm. The 2D Euler simulation had a uniform unstructured mesh with 40k elements.

The static pressure and the Mach number at the center line were compared. The results are presented in Fig. 4.6. All the simulations show closely matching trends in both the pressure and the Mach number, indicating that 3D effects and viscosity have a negligible influence on the results. Only in Fig. 4.6b, where the pressure deviation is shown, a noticeable difference between the 3D RANS and the 2D Euler simulation can be seen close to the throat. It might be due to the interpolation method used for the 3D case or because of a slight mismatch in the throat position in the mesh. It is absent in the 2D RANS simulation. Nevertheless, the deviation is limited to less than 1.5% of the pressure at the throat.

The mass flow rate at the throat calculated assuming a 1D flow is also showing very close results. As shown in Tab. 4.2, the two 2D cases have a negligible difference, while the 3D RANS case with respect to the Euler deviates by only 0.02%.

Table 4.2: Estimate of the mass flow rate at the throat of the 2D Euler, 2D RANS and 3D RANS cases.

Case	Mass flow rate
2D Euler	1.1651 kg/s
2D RANS	1.1651 kg/s
3D RANS	1.1649 kg/s

4.3.6. Comparison between Upwind and Central-Differencing Schemes for NICFD Flows

Numerical schemes can influence the result of a simulation. To verify whether this is the case for the isentropic expansion in a nozzle, the design case was run both with the JST and the ROE numerical scheme. Then some response quantities along the nozzle were compared. The simulation was converged in both cases to a rho residual equal to 10^{-13}. The mesh is made of 40k elements. The JST scheme dissipation coefficients were the default values, 0.5 and 0.12. Figure 4.7 highlights the results. In Fig. 4.7a, the static pressure is compared,

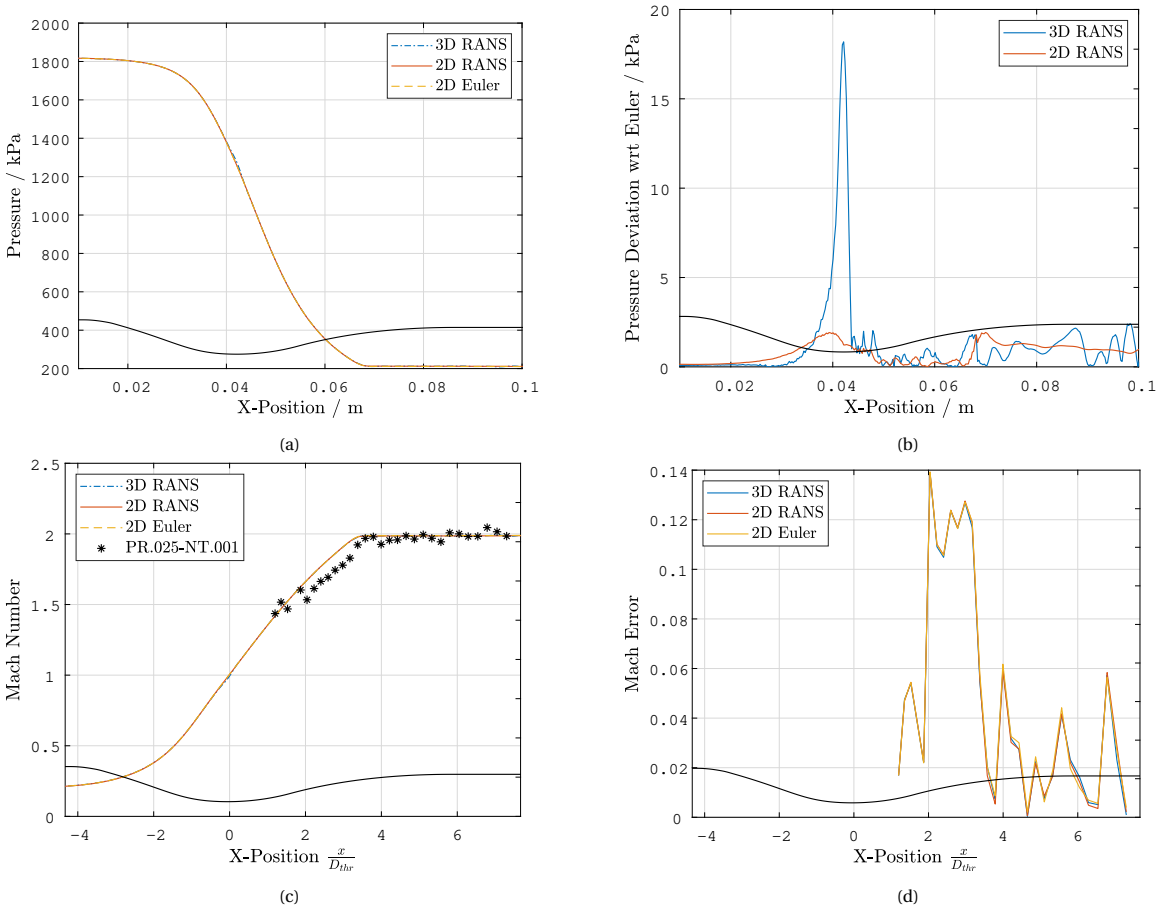

Figure 4.6: Comparison of the static pressure and Mach number along the nozzle for the 3D RANS, 2D RANS and 2D Euler simulations. **a)** Pressure trend along the nozzle center line of the three cases. **b)** Static pressure absolute deviation of the RANS cases with respect to the 2D Euler simulation. **c)** Mach number trend along the nozzle center line of the three cases and the experimental measurements taken from experiment PR.025-NT.001 [34]. **d)** Mach number error of the three models with respect to the experimental data.

no meaningful differences can be noticed. Figure 4.7b presents the relative deviation of the static pressure. The main peaks are in the throat and in the kernel region, suggesting that the largest differences occur in the presence of large gradients. Nonetheless, the maximum deviation is limited to 2 kPa or 0.11% of the pressure at the point. To have a measure of comparison, consider that the maximum deviation of the Euler mesh with respect to the 2D RANS is on the same order of magnitude, see Fig. 4.6. Only the pressure was chosen for comparison since all the other response quantities presented very similar results.

Another comparison was made to determine whether the time required to converge was similar. The JST scheme, while using a variable CFL between 10 and 60, took around 50% more time than the ROE scheme to reach a 2nd order convergence. It was noticed that in some instances the residual in the JST case remained stuck at the same value even for hundreds of iterations.

In conclusion, the deviation in the results calculated with the two numerical schemes is minimal in the case examined. Nonetheless, for more complex cases the deviation could be noticeable in the presence of shock waves or boundary layers due to the large property gradients. The differences are investigated further in the cascade test case presented in Sec. 5.3.5.

4.3.7. Jump Conditions Verification and Wedge Choice

As explained in Sec. 4.2.2, the shock wave angle is not generated with a mesh that includes a wedge, instead it is estimated with a function that solves the jump conditions using as the inputs the flow quantities at the region close to the outlet. The code used to solve the jump conditions was not verified yet. Furthermore, a requirement that needs to be satisfied is the flow uniformity. For these reasons the accuracy of this method was verified by comparing the function output with simulations in SU2. A second objective of this section is to determine if wedges with large angles are suitable to use in the test section or if they lead to flow blockage.

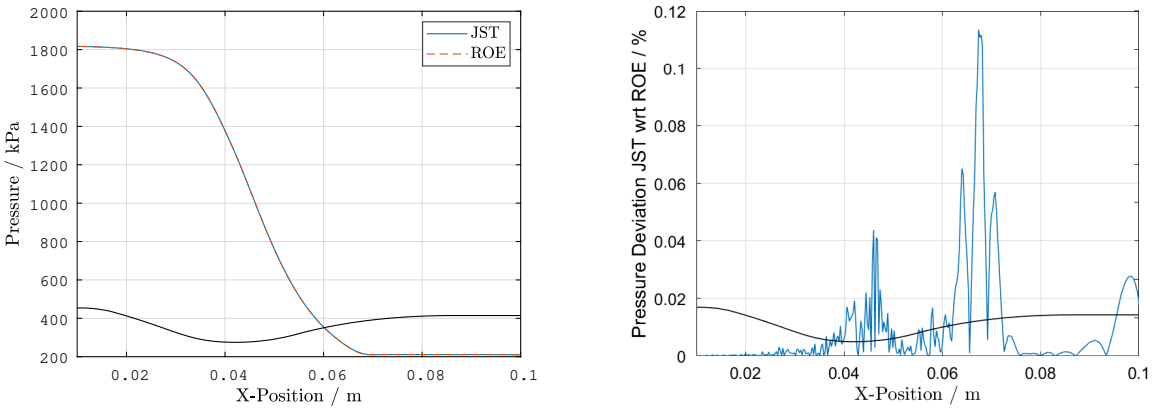

(a) (b)

Figure 4.7: Comparison of static pressure along the nozzle for the JST and the ROE with MUSCL schemes. **a)** Pressure trend along the nozzle center line for JST and ROE with MUSCL schemes. **b)** Static pressure relative deviation between the JST and the ROE with MUSCL scheme.

The comparison was done for the smallest wedge and the two largest ones previously selected to be calculated in the stochastic simulation. The wedges considered are of 2.5°, 26° and 31° half angle. The Euler simulations were run with the mesh of the half nozzle used for the isentropic expansions. The mesh was refined in the region where the shock wave was located to better capture the gradients. The results of the simulations for the 2.5° and the 26° wedges are shown in Fig. 4.8. The wider shock generated with the 26° wedge can be clearly seen in Fig. 4.8b.

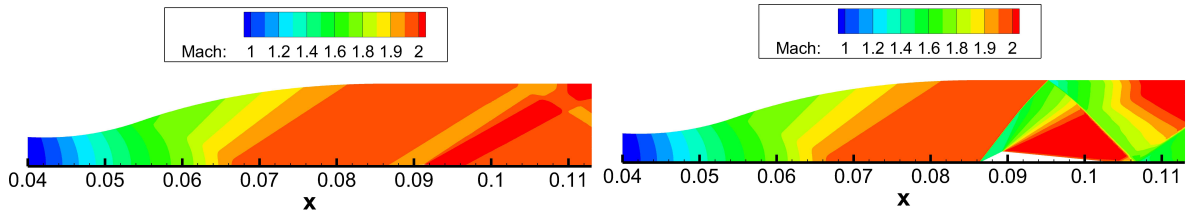

(a) (b)

Figure 4.8: Mach contours obtained from the simulation results of the shock wave generated by **a)** the 2.5° and **b)** the 26° wedge.

Figure 4.9 shows the shock wave generated by the 31° wedge. This wedge angle was discarded since it led to blockage of the flow and to a normal shock wave upstream in the nozzle. Initially the height of the wedge was set to leave 20% more area than the nozzle throat to allow the flow to pass without generating the shock wave. This proved insufficient, so subsequently the available area was progressively increased to 90% and then to 120% of the throat area, these cases are shown in Fig. 4.9a and 4.9b. This was not sufficient, only by leaving 160% of the throat area the shock wave remained attached to the 31° wedge. This case is shown in Fig. 4.9c. Figure 4.9 shows the normal shock wave moving progressively closer to the wedge as its height decreases. The presence of the normal shock wave is due to the wedge choking the flow. This occurs due to the lower density of the flow in the uniform region with respect to the throat which requires a much higher area to satisfy the conservation of mass equation in order to prevent the normal shock.

For the 31° wedge the maximum height allowed to satisfy the area requirement is around 0.9 mm, which makes the wedge difficult to manufacture. As shown in Tab. 4.3, the deviation of this angle with the jump conditions is higher than the other two cases examined, possibly due to the shock wave becoming curve. For these reasons, the 31° should not be used in experiments. The shock angle generated by the 2.5° and the 26° wedges in the Euler simulations matched the prediction of the jump conditions solver, indicating that the code is adequate in calculating the shock wave angle. In the Euler simulation the 26° wedge did not lead to flow blockage, probably because of the lower strength of the shock. An equivalent RANS simulation did not converge, possibly because of flow blockage. The difference with respect to the equivalent Euler case could be due to the lower effective area of the nozzle due to the presence of the boundary layers. The RANS simulation

with the 2.5° wedge did not show blockage problems. It is recommended to use narrower wedges, below 26° half angle, to minimize the risk of flow blockage.

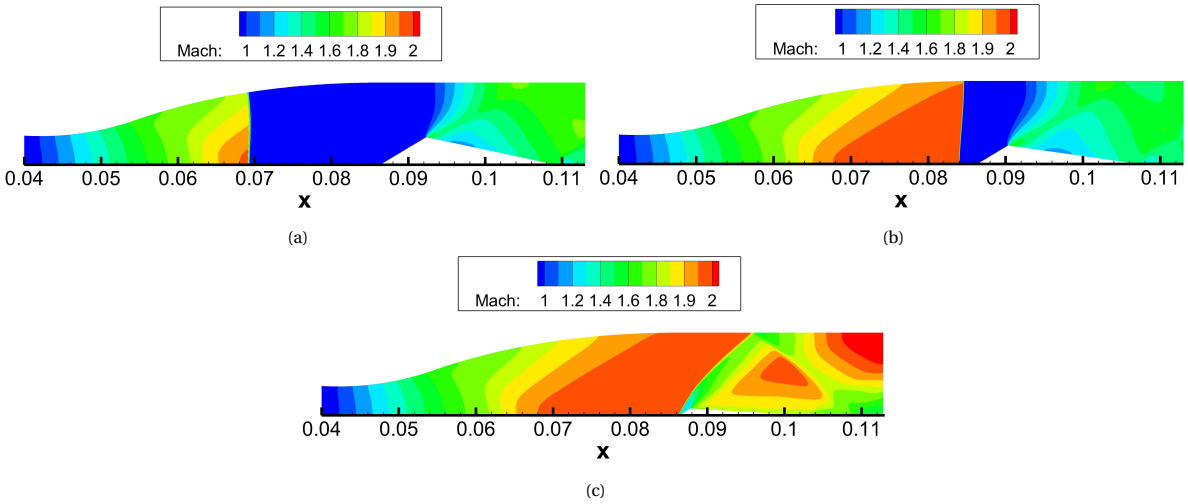

Figure 4.9: SU2 simulations showing the position of the normal shock wave upstream of the 31° wedge with varying wedge height. **a)** Normal shock wave generated by a wedge occupying 34% of the nozzle height. **b)** Normal shock wave generated by a wedge occupying 22% of the nozzle height. **c)** Oblique shock wave generated by a wedge occupying 8.4% of the nozzle height.

Table 4.3: Comparison between the shock wave angles calculated with the jump conditions sovler and measured from Euler simulations for three wedges.

Wedge Angle θ	**Jump Cond.** β	**Euler** β
2.5°	31.87°	$31.5 \pm 0.3°$
26°	52.33°	$52.0 \pm 0.3°$
31°	59.13°	$59.7 \pm 0.3°$

4.4. Characterization of Model Derived Uncertainties

This section presents the simulation expanded uncertainties for the isentropic expansion and for the Mach 2.0 flow over a wedge. The first case was already performed by Bills [9] and Beltrame [7]. Since new sensors are present and some parts of the infrastructure were updated, they will be repeated to provide more accurate results.

4.4.1. Model Definition, Procedure and UQ Infrastructure

The core infrastructure used is mostly unchanged with respect to the one inherited. The most significant updates made since then will be highlighted. The SU2 version was upgraded from V3.2.8.3 "Eagle" to V5.0.0 "Raven" of the turbomachinery branch. This was done to align it to the one currently in use by the Power and Propulsion group at TU Delft. This version provides improved convergence performance, which is useful in particular for the UQ where switching between 1st and 2nd order numerical schemes to help convergence is no longer necessary. `CGNS` meshes have native support, making the generation of 3D meshes easier. For the stochastic simulation, 2 of the 6 inputs, omega and gamma, were removed. This change was made because these two parameters are fitted properties and not input to the system, so they do not have an associated uncertainty. This change allowed to decrease the number of iterations required for the input uncertainty analysis from over 500 to 221. In turn, it was decided to improve the mesh quality from 10k to 40k elements. The influence of the removed inputs was minimal with respect to the other input parameters, so no radical changes are expected in the results.

The procedure used to validate the flow solver consists in the calculation of the total expanded uncertainty of various flow quantities to compare it to the error between the experimental and the average result of the stochastic simulation. Following on the methodology presented in Sec. 3.4, the uncertainties considered are

Table 4.4: Total expanded uncertainty of the input data of the thermodynamic model of MM and of the boundary conditions for the flow simulation. The distribution of the uncertainty is assumed uniform for the fluid model parameters and normal for the boundary conditions of the flow solver.

Parameter	Nominal value	% uncertainty
Peng-Robinson thermodynamic model [14]		
T_{cr} / K	518.7	$\pm 3^{*}$ [61]
P_{cr} / bar	19.40	$\pm 5^{*}$ [61]
Boundary Conditions (BC)		
T_0 / K	525.15	$\pm 0.2^{+}$
P_0 / bar	18.40	$\pm 0.5^{+}$

* Experimental. $^{+}$ Assumed.

the numerical, the input and the experimental ones. The numerical uncertainty is made of the round-off, iterative and discretization uncertainties. The first one is usually negligible when double precision is used, so it will not be considered in this study. The iterative component was described in Sec. 4.3.4, depending on the case it can be either minimized or discarded. The uncertainty due to the discretization error can be calculated by comparing grid with different mesh densities. The mesh generation was described in Sec. 4.3.3. The expanded input uncertainties are calculated by performing a large number of simulations with slightly different input, from the response quantities the effect of their variation can be measured, for more details see Sec. 3.4.2. The experimental uncertainty is determined with the instrumentation as the fluctuation of the values studied over a certain period. The total expanded uncertainty can be calculated by combining these results. Three ways of determining the total uncertainty are used: the V&V 20 method [5], the Real Space method [60] and the Hills model [35].

The case examined is the isentropic expansion at design conditions. The boundary conditions used are an inlet total pressure of 18.4 bara, an inlet total temperature of 525.15 K and an outlet static pressure of 2.1 bara. The uniform unstructured mesh used has 40k elements. The advective fluxes are discretized by using the second-order accurate ROE with MUSCL scheme. The convergence threhsold set is rho residual equal to 10^{-13}.

4.4.2. Expanded Numerical Uncertainty

The expanded uncertainties of the pressure, the Mach number and the shock wave angles due to the numerical uncertainty were computed with Refresco. A series of solutions were generated for a case with the same boundary conditions but mesh made of a different number of elements. The meshes used in this study span from 2500 to 160k elements. The software compares the response quantities at the points of interest to determine the uncertainty associated to the mesh used for the assessment, in this case made of 40k elements. The discretization uncertainty is the only component of the numerical uncertainty since the iterative contribution was demonstrated to be negligible.

Figure 4.10 shows the expanded uncertainty for the pressure along the top wall, for the Mach number at the center line and for the shock wave angles. The points of highest expanded uncertainty in Fig. 4.10a and 4.10b are the throat and at the kernel region. There the maximum expanded uncertainty was still less than 1% of the local static pressure. The peak at the outlet and at the kernel is probably due to the weak shock wave generated when the nozzle wall slope reaches zero. The shock wave angle uncertainty, Fig. 4.10c, increases with the wedge angle, but remains almost constant in relative terms. This is expected since the jump conditions are solved through the flow quantities of a point close to the outlet and wider shock angle becomes more sensitive to the increase in the shock angle.

4.4.3. Expanded Input Uncertainty

The expanded input uncertainties due to the uncertainty in the input are calculated using a UQ framework. The input with an associated uncertainty are four: inlet total temperature, inlet total pressure, critical temperature and critical pressure. The 95% confidence level uncertainties of the input are listed in Tab. 4.4. Through Dakota the statistical moments and the Sobol indices of the input parameters for each response quantities can be gathered.

To verify whether stochastic collocation provides equivalent results with respect to Monte Carlo sampling in CFD applications, the two methods were compared. For the stochastic collocation the number of itera-

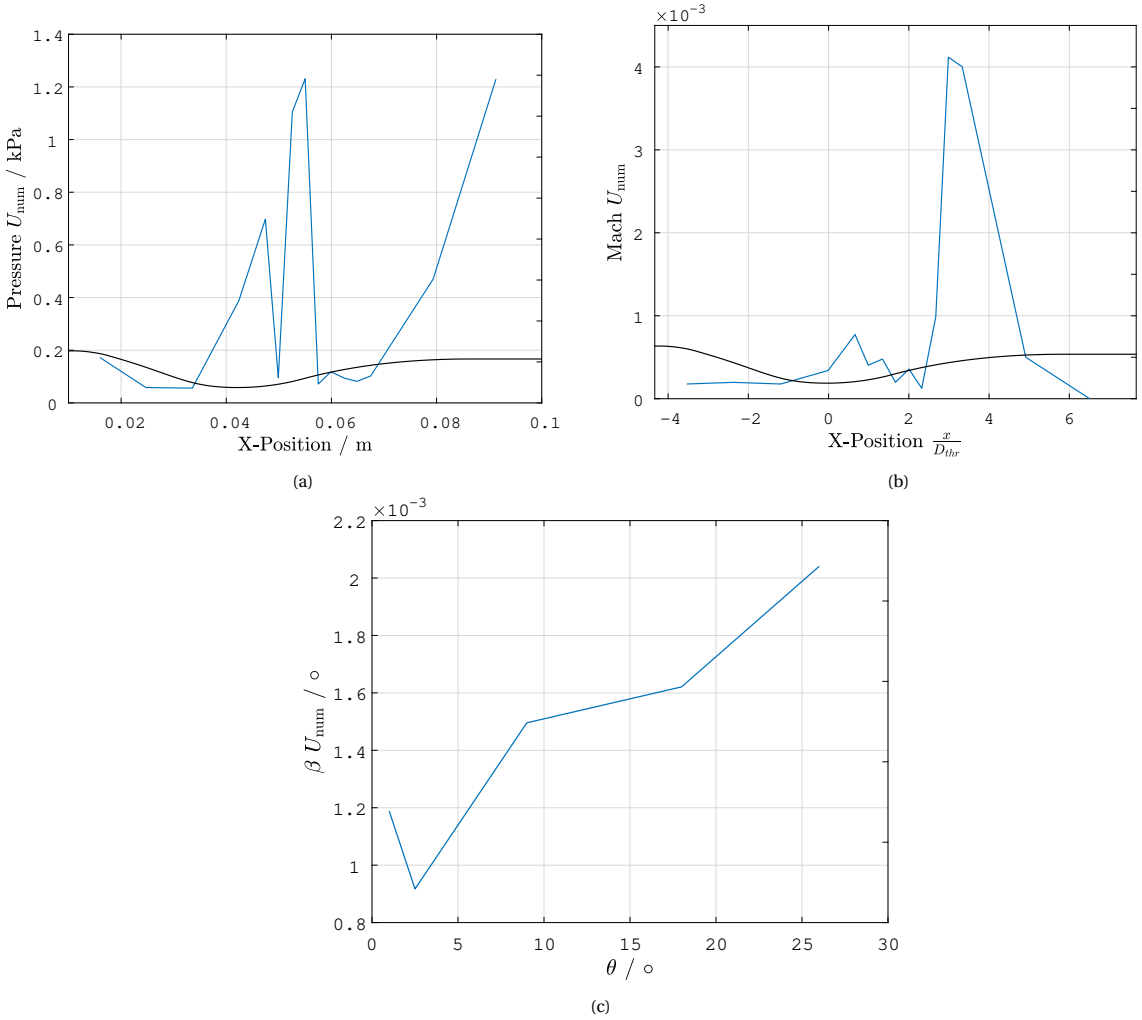

Figure 4.10: Expanded numerical uncertainty U_{num} along the nozzle length for pressure, the Mach number and the shock wave angles. **a)** Absolute static pressure uncertainty along the top wall of the nozzle. **b)** Mach number uncertainty along the center line of the nozzle. **c)** Absolute uncertainty of the shock wave angle for the different wedge angles.

tions to be run depends on the number of input and on the sparse grid level. A higher grid level allows to calculate more statistical moments and to increase the accuracy of the average and of the standard deviation of the response quantities. For this case a level 3 grid was chosen, which requires 221 iterations to be run with the four inputs used. After the surrogate model was complete, the number of simulations executed with the polynomial surrogate were 10000. For the Monte Carlo simulation the convergence of the response quantities mean and standard deviation needs to be verified. This was checked by plotting the evolution of the standard deviation of some response quantities while more simulations were completed to determine whether oscillations were still present. Figure 4.11 shows the convergence history of the pressure and temperature at the throat with their standard deviations. In this study, convergence was reached after around 600 iterations.

Figure 4.12 shows the comparison between the Monte Carlo and the SC simulations. The mean and the standard deviation of the Mach number and the pressure along the nozzle are superimposed. The mean in both figures is very close and the difference between the two is negligible. The standard deviation also shows the same trends, with only minor deviations. In conclusion the two plots are equivalent. Considering that SC requires one third of the number of iterations necessary to converge the equivalent Monte Carlo simulation, it is the preferred choice for this and future UQ studies.

Figure 4.13 shows the two sigma expanded uncertainty due to uncertainty in the input for the static pressure, the Mach number and the shock wave angles. Starting from the pressure case in Fig. 4.13a, the uncertainty is generally low at around 0.6% of the total pressure, and it peaks at less than 2% at the throat, after

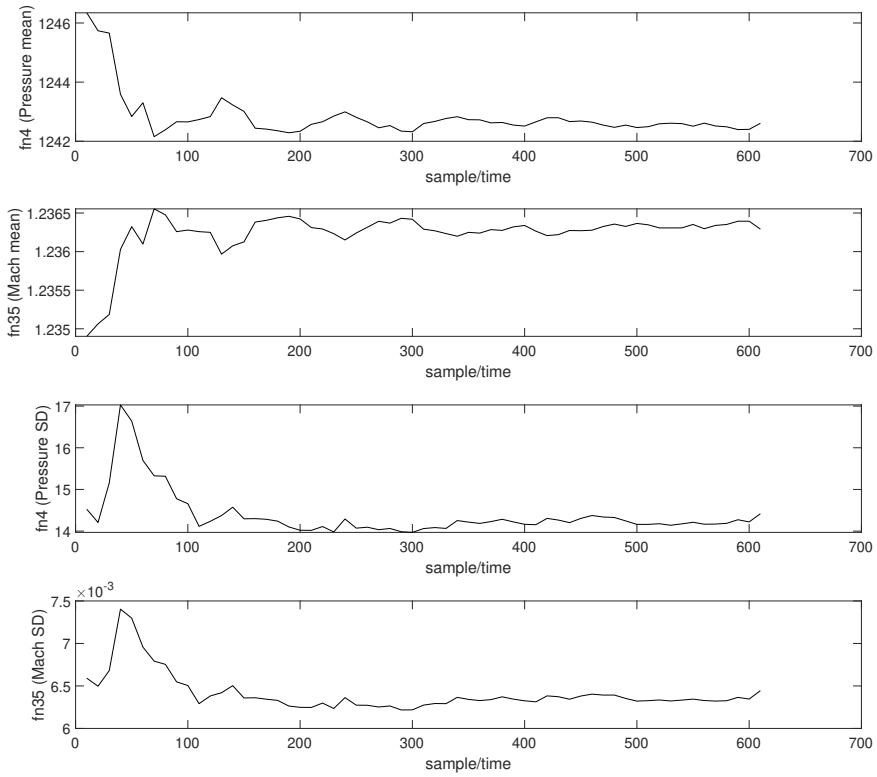

Figure 4.11: Convergence history of the mean and of the standard deviation of pressure and Mach number at the throat.

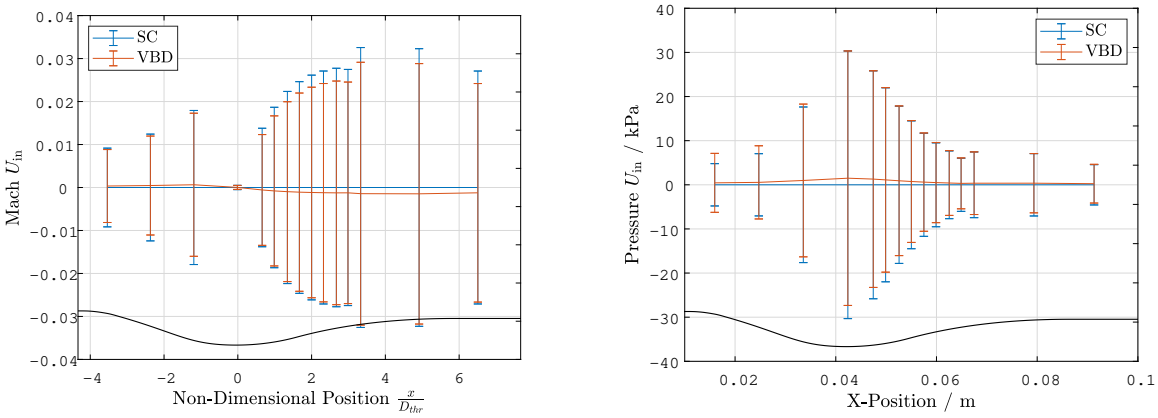

Figure 4.12: Comparison of the Mach number and the pressure response quantities from the UQ calculated with stochastic collocation and the Monte Carlo method. **a)** Deviation of the mean and standard deviation comparison of the Mach number. **b)** Deviation of the mean and standard deviation comparison of the static pressure.

which it decreases. The peak of uncertainty at the throat can be explained by taking into account various factors. There the pressure gradient is high, which leads to a large variation in properties even for a small change in the initial conditions. Furthermore, at the throat the non-ideality is the highest, considering the large influence of the critical properties on the uncertainty, their variation will have the largest effect there. The uncertainty of the Mach number, Fig. 4.13b, follows an opposite trend, it is negligible at the throat where the Mach number is always one, and it increases towards the outlet. Figure 4.13c shows that the absolute

uncertainty of the shock wave angle increases with the wedge angle. This occurs because as the wedge angle increases the shock wave becomes wider, as it can be seen in Fig. 4.22a. The slope of the $\theta - \beta$ function increases when the wedge is wider than 20°, this leads to a higher sensitivity of the shock wave angle to the change of the input.

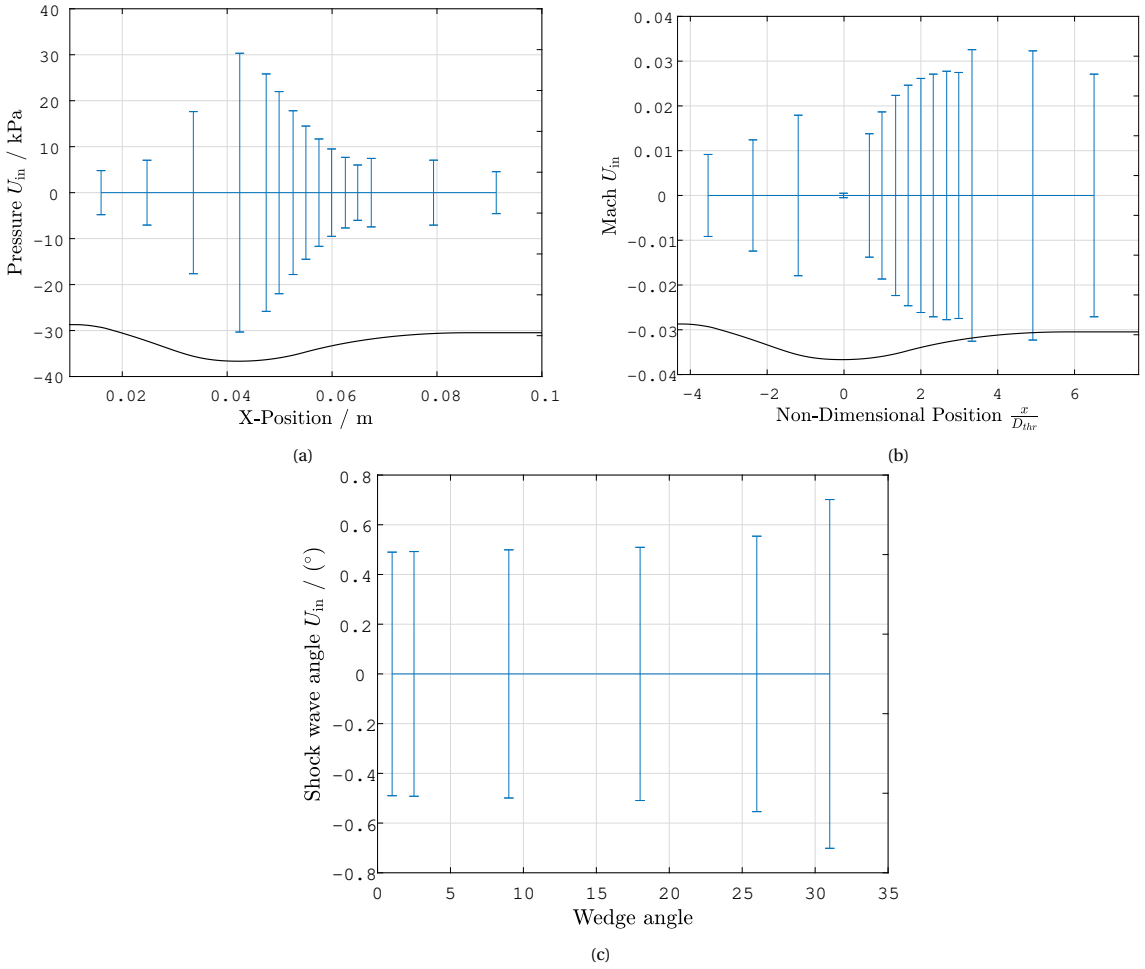

Figure 4.13: Input uncertainty U_{in} along the nozzle for static pressure at the wall, the Mach number at the center line and for the shock wave angles. **a)** Input uncertainty for the static pressure along the top wall. **b)** Input uncertainty for the Mach number along the center line. **c)** Input uncertainty for the shock wave angles for the different wedge angles.

Figure 4.14 shows the Sobol indices for the response quantities assessed. Figures 4.14a and 4.14b show that, in general, the largest influence is due to the critical properties, with an equal share between pressure and temperature. The influence of the total pressure input is only relevant in the convergent part of the nozzle, after which its importance decreases and become negligible. With the response quantities examined, the effect of the inlet total temperature is always negligible. Figure 4.14c shows the shock wave angle Sobol indices for the 26 degree wedge. The Sobol indices are similar to the other response quantities, with the critical properties having the largest share of influence. Only the largest wedge angle is shown since there is no meaningful difference between the various angles. For the shock wave angle also the total Sobol indices are shown. The importance of the critical properties further increases, indicating that a strong coupling between the two exists. The critical temperature contribution is higher than the critical pressure one possibly because the first is elevated at the power of two in the Peng-Robinson EoS, see Eqn. 2.4.1.

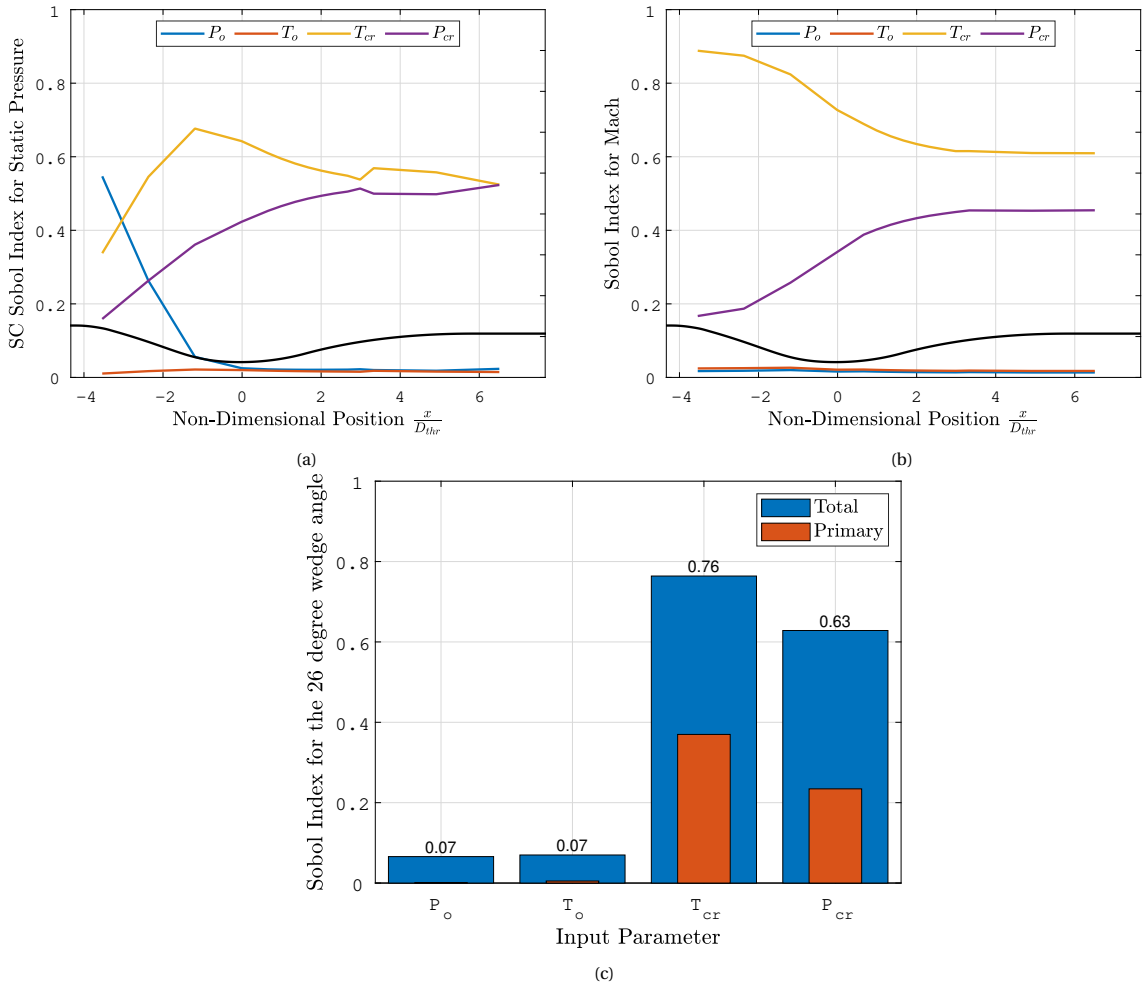

Figure 4.14: Sobol indices along the nozzle for static pressure at the wall, the Mach number at the center line and for the shock wave generated by the 26 degree wedge. **a)** Primary Sobol indices for the static pressure along the top wall. **b)** Primary Sobol indices for the Mach number along the center line. **c)** Primary and total Sobol indices for the shock wave angle of the 26 degree wedge.

4.5. Experimental Procedure

Four types of experimental response quantities are used in the validation process: the static pressure, the mass flow rate, the Mach number and the shock wave angle.

The static pressure is measured at 15 different locations, three of these have a symmetrical tap located on the opposite side of the wall. This was done to ensure that the flow was uniform. Measurements of the pressure should be carried out first since they allow, together with the inlet temperature, to identify whether the target thermodynamic conditions have been achieved. The pressure quantities were not obtained due to issues with the experiment, pseudo-experimental data were used instead.

The mass flow meter is of Coriolis type and it is located before the test section. It directly measures the mass flow rate and the density in the vapour state. The Mach field cannot be directly measured, instead the schlieren technique is used to calculated the expansion waves angles which can be directly related to the Mach number at the location they are extracted. A tool was developed by Beltrame [7] to convert raw schlieren images of the flow field into Mach number measurements with propagated uncertainty. Schlieren imaging is a photography technique which allows to visualize the variation of density in a transparent medium that cannot be seen with the naked eye. This is possible thanks to the change in the refractive index with the density. It is used to study shock waves since the density gradient is large, thus leading to a better contrast. Mach waves, which are very weak, are difficult to visualize for air. On the other hand it is possible for heavier organic molecule such as siloxane MM, since the change in refractive index with the density is much higher [7]. The same schlieren chain set-up is used to extract the shock wave angle, with the advantage of these

having a higher contrast between before and after the shock. A tool to systematically extract the angle from a multiple pictures is not available for the shock waves, the experimental uncertainty is an estimate of the bias introduced by the operator when he manually measures the angle.

The schlieren layout used is shown in Fig. 4.15. It is a z-type two-lens configuration. The LED light source which provides a cold white light is positioned outside the ORCHID. The maximum output is of 2350 mW. A tube is positioned around the light source where at its end a lens with a focal length of 150 mm. The light then passes through a pinhole and it goes once again through a lens before being redirected by a mirror to the test section. The pinhole has a diameter of 2 mm, this parameter can be varied and it determines the set-up sensitivity to the density gradient. The test section presents a window on both of its sides which allows the light to cross the flow from side-to-side. The light then reaches mirror B and then lens C which converges the light to the knife edge. This tool blocks half of the incoming light which is what makes the density gradient visible. Then, the light reaches the camera lenses and its sensor. Two cameras are used, a high frequency LaVision Imager Pro HS4M camera, up to 1279 frames per second, used to assess the start-up phase of the experiment, and a Bobcat IGV-B1610, up to 25 frames per second, to acquire lots of pictures over an extended time period to obtain meaningful statistics.

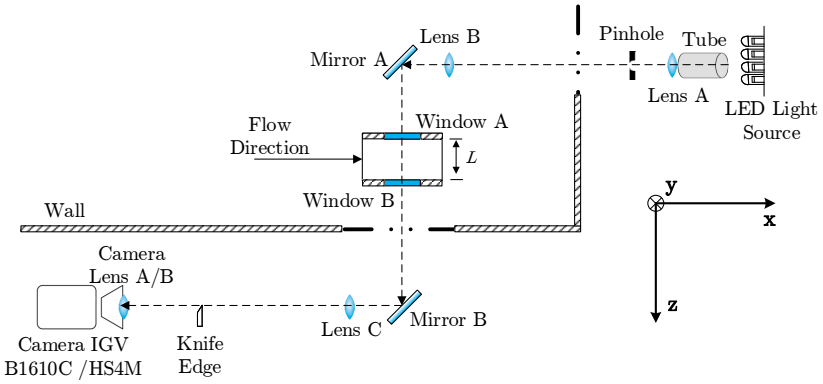

Figure 4.15: Schlieren set-up used to photograph Mach and shock waves. Taken from Head [34].

4.6. Operating Conditions

The experimental data used in this thesis was generated in two experimental campaigns: PR.025 [34, Chap. 6] and PR.028.

The conditions achieved in each session are presented in Tab. 4.5. In PR.025 [34, Chap. 6] the design conditions of the nozzle were reached. In this experiment the Mach number field and the mass flow rate were measured. In PR.028 the design conditions could not be achieved, a lower total pressure and temperature at the inlet were used. In this campaign the shock wave angle generated by a wedge with a 2.5° half angle was photographed.

Table 4.5: Boundary conditions of experiments PR.025 [34, Chap. 6] and PR.028.

Case	Inlet Total Pressure	Inlet Total Temperature	Outlet Static Pressure
PR.025	18.4 bara	252°C	2.1 bara
PR.028	3.50 bara	180°C	1.00 bara

4.7. Results

4.7.1. Mach Field, PR.025

The Mach number along the center line was computed from the Mach waves recorded in the ORCHID in case PR.025-NT.001 and PR.025-NT.002 [34, Chap. 6]. Two series of schlieren photos were taken. In the first the complete divergent section of the nozzle was photographed. Since the kernel region showed a large discrepancy with respect to the simulations, the second series focused on that zone. This allowed to slightly decrease

the expansion wave angle uncertainty and increase the spatial resolution of the angles extracted. The data is visualized in Fig. 4.20 and 4.21. From this campaign the mass flow rate was also measured.

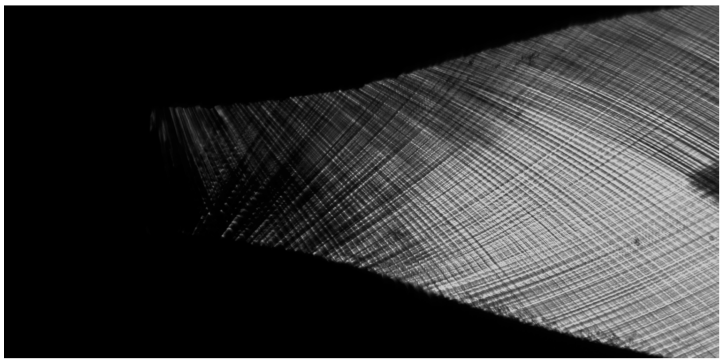

Figure 4.16: Exemplary schlieren image of the supersonic expansion through the ORCHID nozzle taken during the PR.025-NT.002 [34, Chap. 6] process run.

Figure 4.16 shows a schlieren photo of the nozzle divergent section. In this experimental campaign it was noticed that the throat region was too dark to extract the Mach waves. To fix this problem it is recommended to increase the power of the light source to its limit and the exposure time of the camera. Then, to avoid having too bright regions, a graduated neutral density filter can be placed in front of the camera lens. A neutral density lens allows to uniformly decrease the light going through it, the graduated version does so only in half of the lens. The transition is gradual, so it can be regulated as needed.

4.7.2. Shock Wave, PR.028

In this section the new experimental data will be presented. From the most recent campaign, PR.028-NT.001, the shock wave angle generated with the 2.5° half angle wedge was measured.

The case was not performed at design conditions. Since the expansion was isentropic, the shock angle should match the simulation's one at design conditions. This can be demonstrated with Eqn. 2.22, the β angle depends only on θ and the Mach number before the shock wave. The wedge angle θ was unchanged, and so was the Mach number at the outlet since it is only dependent of the nozzle shape. A verification of the Mach number will be performed by measuring an expansion wave in the uniform region of the nozzle. A picture of the shock is shown in Fig. 4.17 with various flow features highlighted. The shock wave is identified by the orange lines, the green ones shows one boundary of the expansion fan at the corner of the nozzle outlet and the purple ones indicate the expansion waves. Using the relation $M = 1/\sin\mu$ with the expansion wave angle shows that the Mach number at the outlet is 2.10 ± 0.05, close to the design conditions value. The uncertainty associated to the Mach number is an estimate of the bias introduced by the human operator while manually measuring the expansion wave angle. The shock wave angle measured as the average between the ones at above and below the wedge, is 32.05°. During experiment the shock angle did not fluctuate. If confirmed by a statistical analysis, this would prove the minimal influence of the inlet boundary conditions on the shock angle.

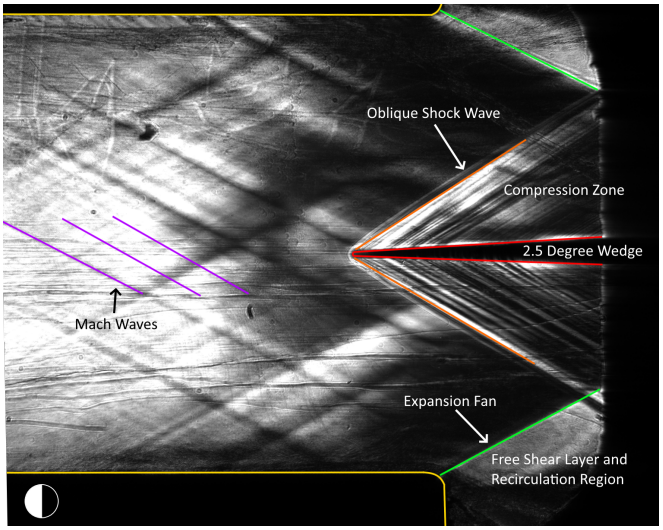

Figure 4.17: Shock wave generated by a 2.5 degrees wedge with highlighted the main flow features. The yellow lines represent the nozzle walls.

4.8. Validation Assessment

In this section the error between experimental data and simulations will be compared to the expanded uncertainty using various methods to determine if a modeling error is present.

Section 2.6 discussed three methods to assess a CFD solver. The first is the ASME V&V20 [5]. It is the most straightforward one, the comparison is made between the total uncertainty and the comparison error leading to a yes-no answer to the validation question. Romero instead developed the real space model [60], with this method the uncertainty of the experiments is separated from the simulation's ones. This way it is possible to determine whether the two uncertainties overlap to confirm validation. Unlike the other two, the Hills model [35] only provides a bulk value to determine whether the validation was successful. It requires a vector containing a series of comparison errors and another containing the associated total uncertainties. The method involves a probabilistic approach. For a result lower than one, the errors outside the normal distribution are less than expected for the normal distribution with the number of response quantities considered, and so it can be considered valid. If the value is higher than one, the case is not valid since the errors outside the normal distribution are more than expected.

The pressure experimental data was generated with the state-of-the-art CFD software based on RANS equations, since pressure measurements at design conditions do not exists. The domain used for the simulation was the 3D half-nozzle with 5 million elements. The SST model was used to solve the turbulent quantities. The thermophysical properties were computed with the RefProp thermodynamic model. The results were sampled at 15 locations coincident with the pressure taps of the ORCHID.

4.8.1. Total Expanded Uncertainties

In this section the total expanded uncertainties are presented. Since it is assumed that each uncertainty source is independent of each other, the following equation can be applied for each response quantity

$$U_{\text{val}} = \sqrt{U_{\text{in}}^2 + U_{\text{num}}^2 + U_{\text{d}}^2}. \tag{4.4}$$

Figure 4.18 shows the total expanded uncertainty for the properties of interest and also the breakdown of its composition. The numerical uncertainty, being at least an order smaller than the other contributions, becomes practically negligible in all conditions. For the pressure and the shock wave angles, shown in Fig. 4.18a and 4.18c, respectively, most of the uncertainty is due to the model inputs. The pressure plot does not have an experimental uncertainty associated since the pseudo-experimental data was generated with a CFD software. The experimental uncertainty of the shock wave angles is an estimate of the bias introduced by the human operator while manually measuring the shock wave angle, it is constant for all angles and equal to 0.4°. This value was chosen by calculating the range of measures for known angles. For the Mach number, shown in Fig. 4.18b, the experimental uncertainty is predominant. This is due to the resolution of

the schlieren set-up used. The peak total uncertainty of the pressure is in the throat and at the kernel region. The Mach number and the shock wave angle total uncertainty is roughly constant.

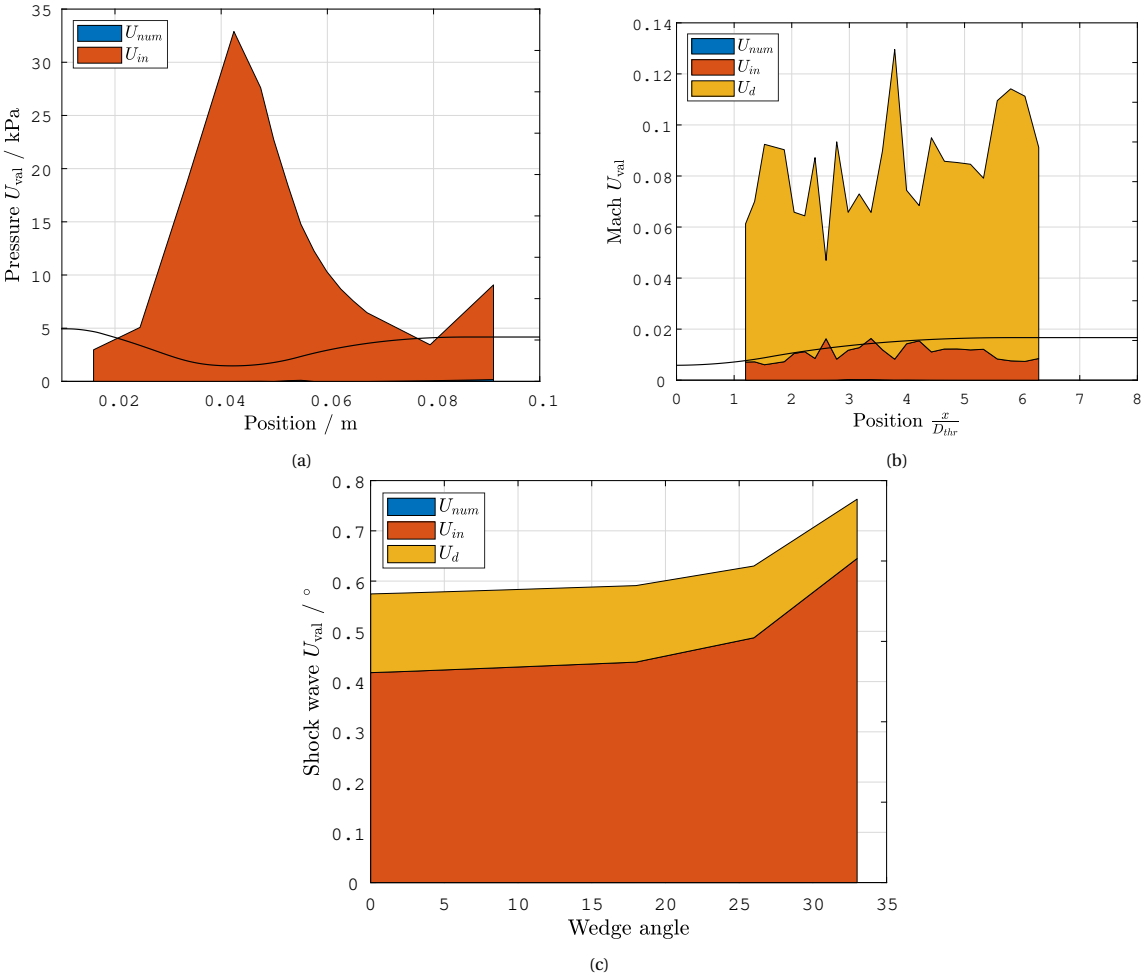

Figure 4.18: Total uncertainty along the nozzle for the static pressure at the wall, the Mach number at the center line and for the shock wave angles. The experimental uncertainties were obtained from experiments PR.025-NT.001 [34, Chap. 6] and PR.028-NT.001. **a)** Total uncertainty for the static pressure along the top wall. **b)** Total uncertainty for the Mach number along the center line. **c)** Total uncertainty for the shock wave angle for the different wedge angles. The experimental uncertainty is an estimate of the bias introduced by the operator when he manually measures the angle, it is assumed to be constant for all wedges.

4.8.2. Pressure and Mach Number

In this section the pressure and the Mach number from the experiments and the SU2 simulations will be compared. The pressure was generated with the state-of-the-art CFD software at design conditions. The Mach number was extracted from experiments PR.025-NT.001 and PR.025-NT.002 [34, Chap. 6]. The boundary conditions of these experiments are presented in Sec. 4.6.

Figure 4.19 shows the comparison between total uncertainty (U_{val}) and comparison error (E) for the pressure with the V&V20 and the Real Space methods. Figure 4.19a shows that the error remains low and constant at 5 kPa, or 0.3% of the total pressure, along the nozzle length. The total uncertainty instead peaks at over 30 kPa around the throat, less than 2% of the total pressure. In Fig. 4.19c, it can be seen that the pressure of the experiment tends to stay below the mean value of the simulation in the supersonic part of the nozzle, slightly outside the uncertainty bands, indicating that a trend probably exists. With the exception of the points close to the outlet which lies slightly outside the uncertainty bands, both models show that the validation is successful.

The result provided by the Hills model is 0.6073, much below one, which indicates that statistically the presence of a few points outside the bounds is not significant. The three methods are in agreement. It should

be noted that the pressure generated by the state-of-the-art CFD software might not be representative of the true values. In particular, Bills [9] compared the experimental pressure at non-design conditions, case PR.027-NT.001 [34, Chap. 6], and found that in the region close to the throat a large deviation outside the bounds of uncertainty was present. Experimental data for the design conditions should be gathered to confirm the observations made here.

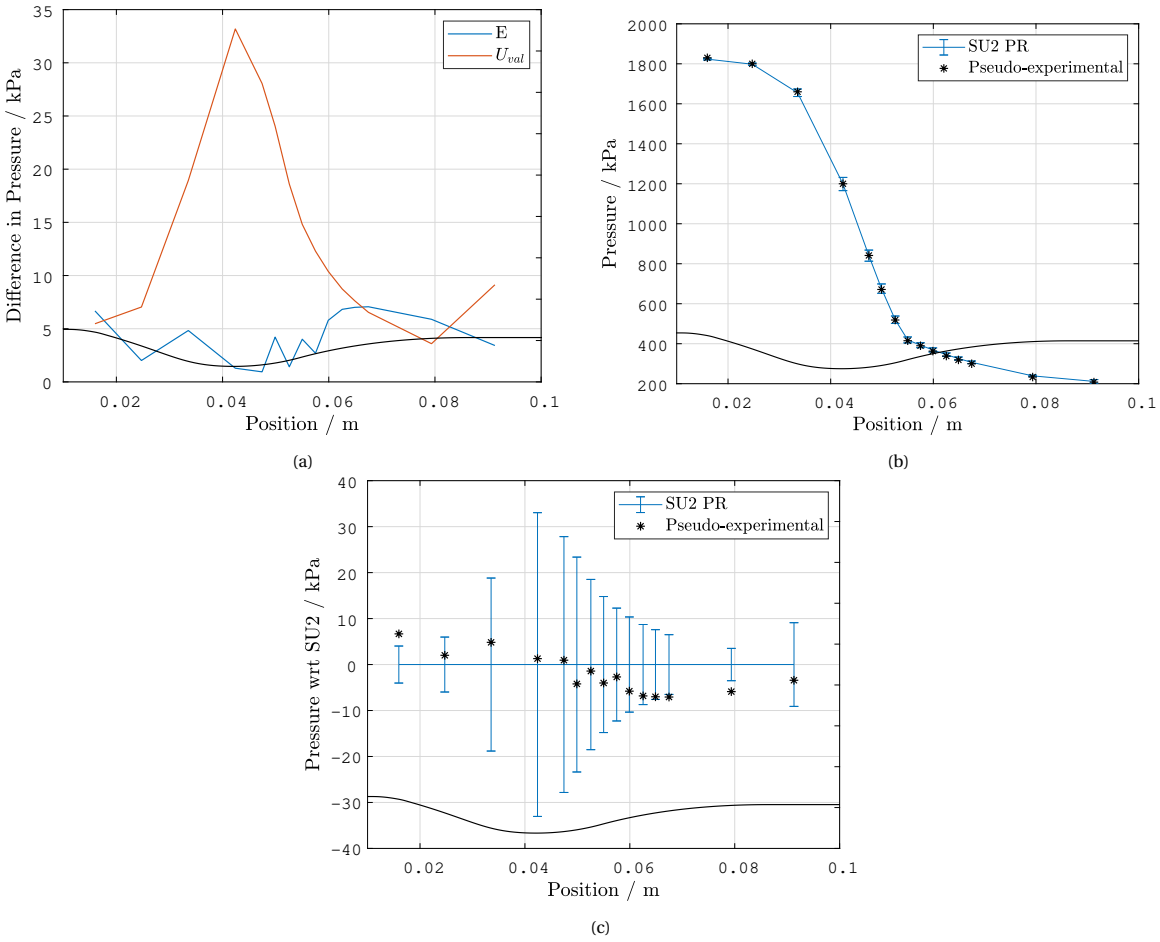

Figure 4.19: Values of the static pressure from the state-of-the-art CFD software and from the simulations using the V&V 20 and the real space methods. **a)** Comparison with the V&V 20 method of the pressure. **b)** Comparison with the real space method of the pressure. **c)** Comparison with the real space method of the pressure normalized with the simulation result.

Figure 4.20 shows the comparison between the total expanded uncertainty (U_{val}) and the comparison error (E) for the Mach number in the diverging part of the nozzle. Figure 4.20a shows a clear trend. The total uncertainty tends to be high at around 0.08 Mach, as seen earlier mostly because of the experimental uncertainty. Nonetheless, it remains roughly constant in the region considered. The error, which remains low at around 0.03 Mach near the throat and in the uniform region, peaks at more than 0.1 Mach in the kernel region. There the comparison error is higher than the total uncertainty, which indicates that the model is unable to predict correctly the Mach number.

The same trend is registered in Fig. 4.20b and 4.20c, the simulations and experiments match in every region with the exception of the kernel where the uncertainties do not overlap. The reason for this mismatch could be due to the Peng-Robinson equation not being accurate in the conditions found at the kernel. This was noticed when the operating maps were generated, but this does not explain why just after the throat the error decreases again. Using Hills model to determine whether validation is achieved produce 0.91 as the result, which indicates that overall the validation is acceptable. But in this case the value is closer to one than in the pressure case, which indicates a less clear outcome.

Since only the kernel region showed unacceptable results, more experiments were performed focusing on that zone. Doing so allowed to increase the resolution of the schlieren photos making it possible to increase

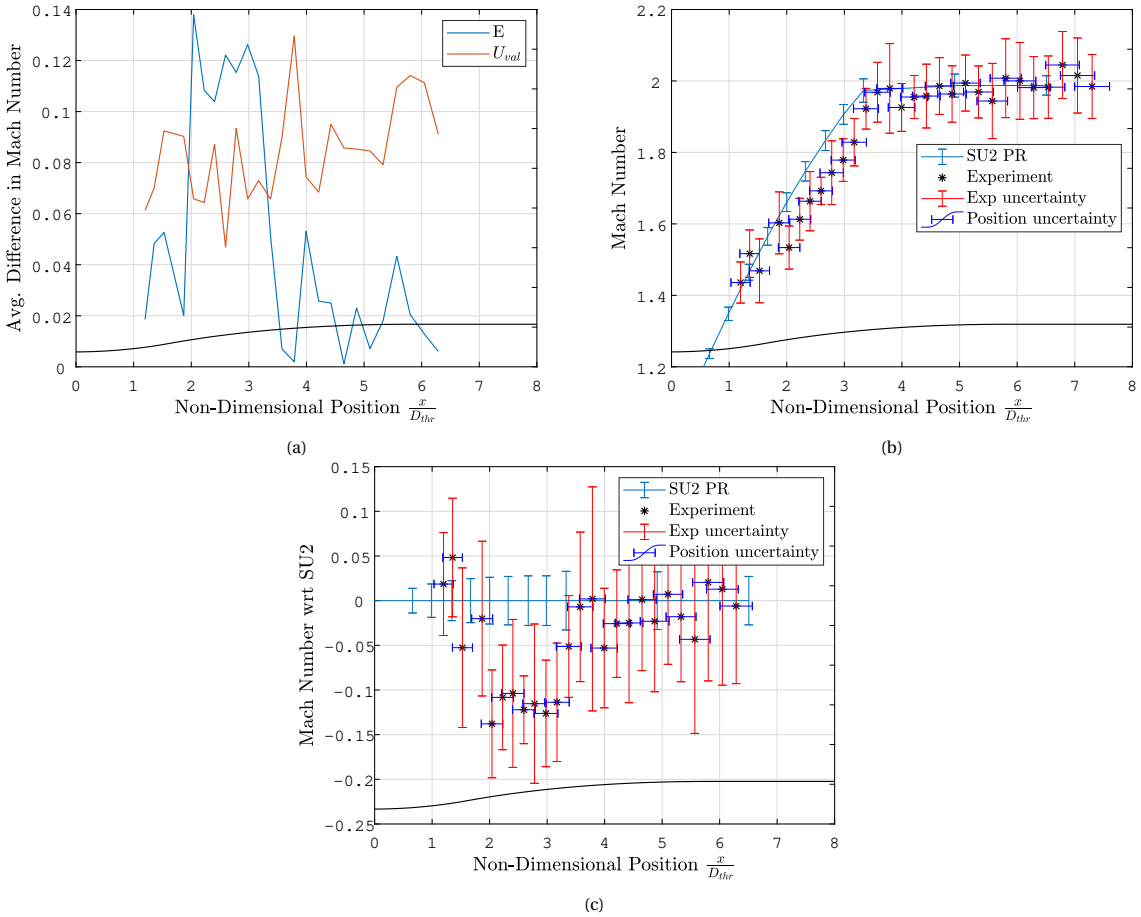

Figure 4.20: Experimentally derived Mach number from experiment PR.025-NT.001 [34, Chap. 6] and from the simulations using the V&V 20 and the real space methods. **a)** Validation with the V&V 20 method for the Mach number. **b)** Comparison with the real space method of the Mach number. **c)** Comparison with the real space method of the Mach number normalized with the simulation result.

the quality of the expansion waves. Figure 4.21 shows the results from the PR.025.NT.002 [34, Chap. 6] experimental campaign. The first note of interest, visible in Fig. 4.21a, is the confirmation of the large error. The mismatch can be clearly seen also in Fig. 4.21b. For this data set Hills model provide an overall value of 1.77, much higher than one, indicating that the comparison is not valid. The large difference between the results from experiments PR.025-NT.002 and PR.025-NT.001 [34, Chap. 6] is due to the difference in the region examined. Hills model compares the distributions of the errors with respect to the expected normal distribution. In the first set the large errors were limited to a portion of the points, instead, when focusing on the kernel region, most points were outside the expected distribution making the result not valid.

4.8.3. Shock Waves

In this section the shock wave angle is assessed as a direct response quantity for the validation of the SU2 flow solver. Figure 4.22 compares the experiments to the simulations. In Fig. 4.22a, the shock wave angles are plotted against the wedge angles. As expected, higher flow turning angles lead to wider shock angles. The experiment for the 2.5° wedge shows a comparison error of only 0.57% of the shock wave angle. Furthermore, as shown in Fig. 4.22b, the uncertainty of the simulation fully contains the uncertainty band of the experiment, which is the real space method criteria for considering a comparison successful. Even though the operating conditions of the experiment were very different from the design case of the nozzle, the shock wave angle is matching the simulations performed at design condition. This suggests that, as long as the expansion remains shock free, the Mach number at the exit will be unchanged and so will be the shock wave angle. This argument is also supported by the negligible influence of the total properties on the shock angle Sobol indices. This result confirms the suitability of the SU2 flow solver in simulating the flow in the presence of shocks. Further experiments should be run at the design conditions and with wider wedges to generalize

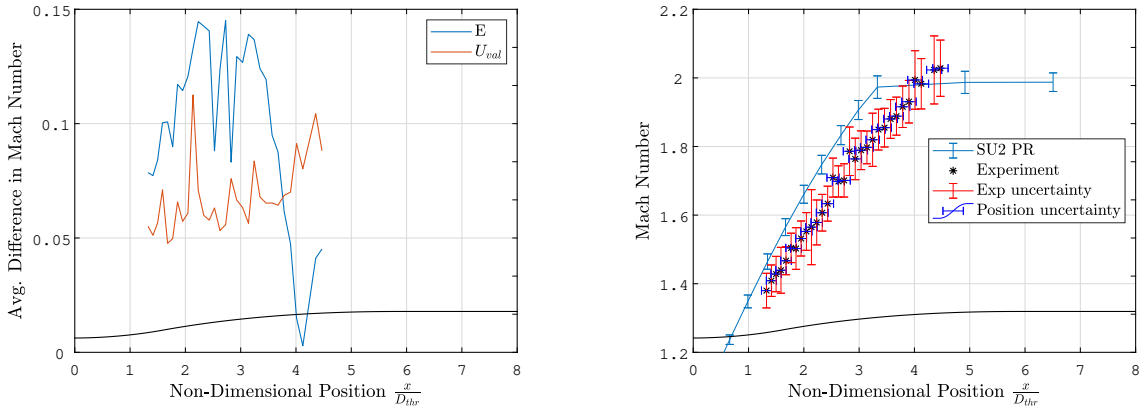

(a) (b)

Figure 4.21: Experimentally derived Mach number from experiment PR.025-NT.002 [34, Chap. 6] and from the simulations at the kernel region using the V&V 20 and the real space methods. **a)** Comparison with the V&V 20 method of the Mach number at the kernel region. **b)** Comparison with the real space method of the Mach number at the kernel region.

this conclusion for stronger shock waves. After examining blockage risks, it should also be considered moving the wedge closer to the throat, since there the flow is non-ideal.

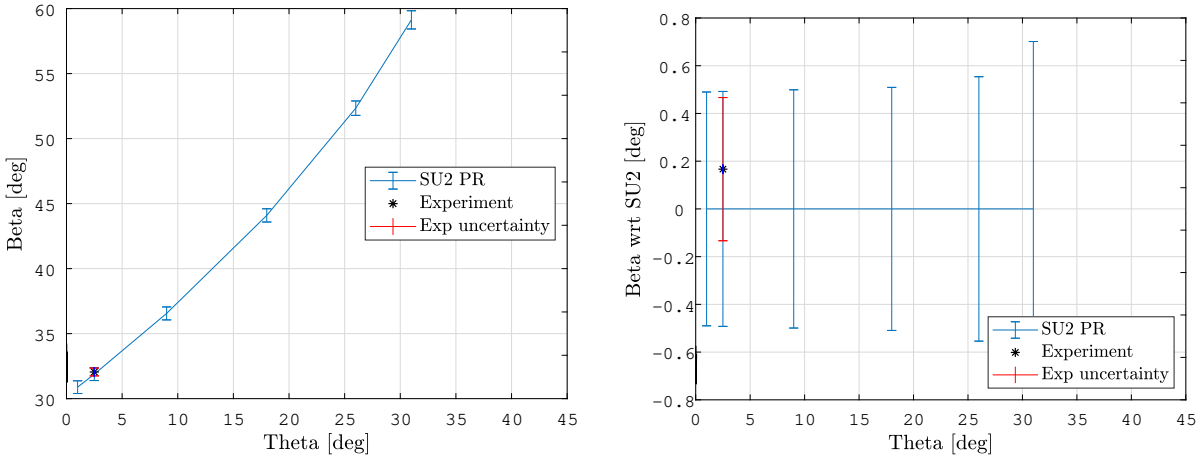

(a) (b)

Figure 4.22: Comparison of the shock wave angle from experiment PR.028-NT.001 and from the simulations using the real space method. **a)** Shock wave angle against the wedge angle, with associated uncertainties. **b)** Comparison of the shock wave angle from the experiment and from the simulations, with the associated uncertainties.

4.8.4. Mass Flow Rate

The first system response quantity to be assessed is the mass flow rate. Figure 4.23 presents the expanded uncertainty due to the uncertainty in the input. Figure 4.23a shows the influence of the input uncertainty on the mass flow rate. Similarly to most other response quantities, the uncertainty is mostly due to the critical properties. Figure 4.23b shows the total expanded uncertainty breakdown for the mass flow rate, the largest share derives from the input uncertainty.

Table 4.6 shows the result of the comparison. The comparison error is much higher than the uncertainty. If plotted, the two uncertainties, experimental and from the simulation, do not overlap. This indicates that there must be either a calibration error of the meter or a large density prediction error at the throat in the simulation. The 1D approximation should not be the reason for this, since in App. B it was demonstrated to closely match the integral method of the momentum at various surfaces. It was also hypothesized that a bleed on the bypass valve could be present.

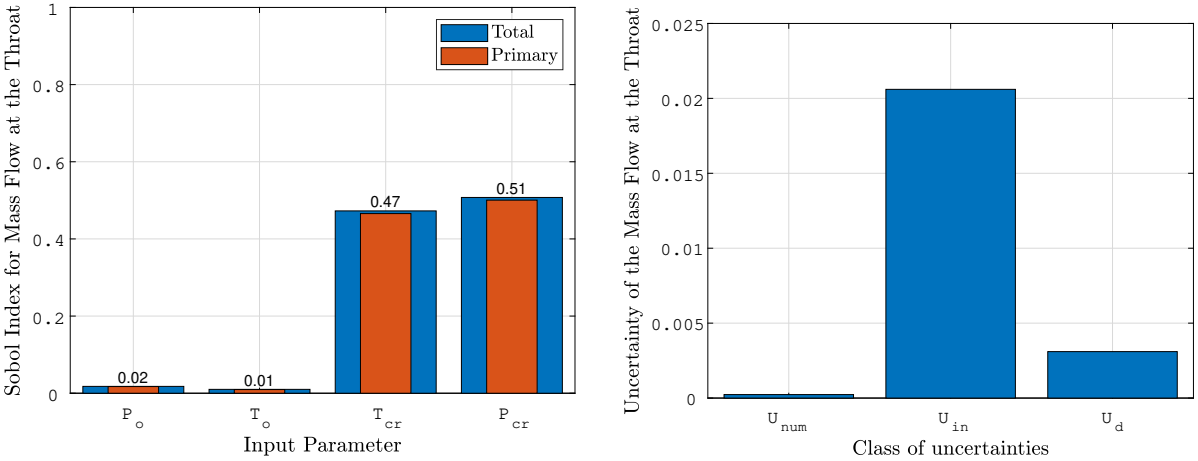

Figure 4.23: Sobol indices and uncertainty breakdown of the mass flow rate at the throat. **a)** Sobol indices for the mass flow rate. **b)** Uncertainty breakdown for the mass flow rate.

Table 4.6: Mass flow rate measure from simulation and experiment PR.025-NT.001 [34, Chap. 6] together with the comparison error and the total uncertainty.

	Mass flow rate
Simulation S	1.1659 kg/s
Experiment D	1.2576 kg/s
Comparison Error E	0.0917 kg/s
Total Uncertainty U_{val}	0.0208 kg/s

5

Towards the Validation of the SU2 Flow Solver for NICFD Turbomachinery: the Case of the Linear Cascade

This chapter documents the preliminary outcomes of a numerical study related to a validation exercise of the SU2 solver for turbomachinery applications by means of a supersonic linear cascade. For this initial assessment direct response quantities such as pressure, Mach number, density and the mass flow rate are analyzed as potential candidate measurements for the validation of the SU2 flow solver. However, other fluid dynamic and thermodynamic quantities are also recorded because they are critical for the calculation of system response quantities (SRQ), such as loss coefficients. In the future it will be possible to easily calculate different system response quantities (SRQ), for example to study loss coefficients. Since the experimental infrastructure is not yet available, the results will be verified with the state-of-the-art CFD software. The findings will be used to provide guidance in the set-up of the future experiments.

In the first section the validation hierarchy for the cascade blade row is presented. In Sec. 5.2, the test section is described and the response quantities selected are defined. Follows in Sec. 5.3 the verification of the assumptions made, the definition of the thermodynamic model and of the numerical scheme. The mesh generation and the choice of the convergence threshold are presented in Sec. 5.3.2 and 5.3.3, respectively. The characterization of the uncertainties is described in Sec. 5.4. Finally, the verification of the results in performed in Sec. 5.5.

5.1. Validation Hierarchy

A list of unit cases that can be executed in the cascade is presented in Fig. 5.1. The case which will be examined in this chapter is the supersonic flow through a 5-channel blade row. The aim of the validation unit test cases is to validate the solver for a more complex flow case and to assess the capabilities of the adjoint-based optimization framework of SU2. A series of investigations can also be performed by measuring flow quantities in a linear supersonic cascade:

- blade shape and cascade design parameters like the solidity can be easily adjusted and their effect studied;
- shock boundary layer interaction, thanks to a clean optical flow path;
- unsteady flow phenomena, by varying the conditions upstream of the blade row; and,
- wake mixing, by positioning measuring probes along the wake [36].

The optimized geometry case will be defined using the information gathered in this verification. It is left to future work since a comparison with experimental data should be performed first. The flow through a rotor is also envisioned as a unit test case, since this is an active area of research. The mechanical design of the cascade vapour tunnel was designed also with this case in mind [31].

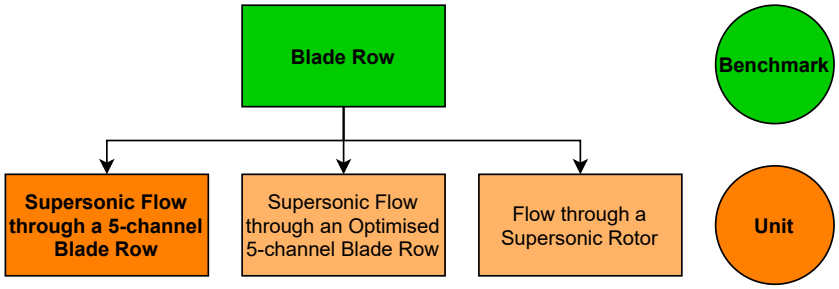

Figure 5.1: List of unit cases envisioned to validate the flow solver for the prediction of the flow physics inside a blade row. The dark orange boxes represent the unit cases analysed in this thesis.

5.2. Design of Experiments

Design of experiments is a process of experimental planning such that the data obtained are suitable for a statistical analysis [15]. The relative influence of each parameter on the validation uncertainty can then be computed and the uncertainty reduced to improve the quality of the validation.

The supersonic flow through a 5-channel blade row case is designed to assess the choice of turbulence and transport models in a CFD simulation. This section describes the domain which will be used in the simulations and how the flow quantities were chosen.

5.2.1. Test Section

The complete mechanical design of the cascade vapor tunnel is described in Hariharan [31]. It is built up of three main components; namely, the settling chamber, the blade row housing and the receiver dump tank. The blade row housing contains the blade row, which is mounted on a wheel. The cascade blade row is shown in Fig. 5.2. The names shown in the figure identify each blade, FB stands for full blade while the N and the S stand for north and south. MP indicates the measuring passage.

Before reaching the blade row, the flow goes through a settling chamber which makes it uniform when it approaches the leading edge of the blades. Immediately after the blade row, the exit channel is aligned with the outlet blade angle so to be parallel to the flow direction.

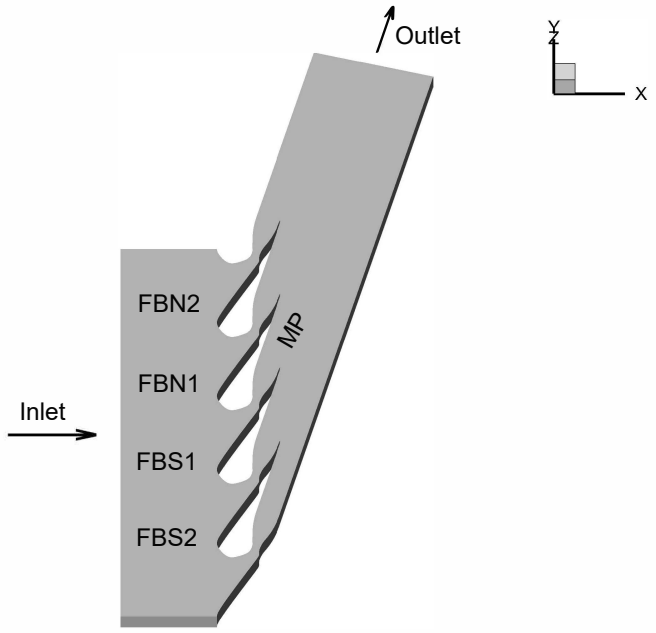

Figure 5.2: A 5-channel cascade blade row. FB stands for full blade, while N and S indicates north and south. MP stands for measuring passage.

The cascade includes four blades immersed in the flow domain with half blades (a pressure and a suction

side) on the top and on the bottom wall. The blade channels/stators are designed to accelerate the flow to Mach 2.0 and at an outlet flow angle of 75 degrees. Each channel has a throat area of 30.6 mm^2, which gives a throat width of 3.83 mm and a blade height of 8 mm. The throat size was chosen in order to not require more than the maximum thermal power that can be generated by the ORCHID for the design conditions. The design operating conditions of the cascade are listed in Tab. 5.1 and the resulting isentrope is shown in Fig. 5.3.

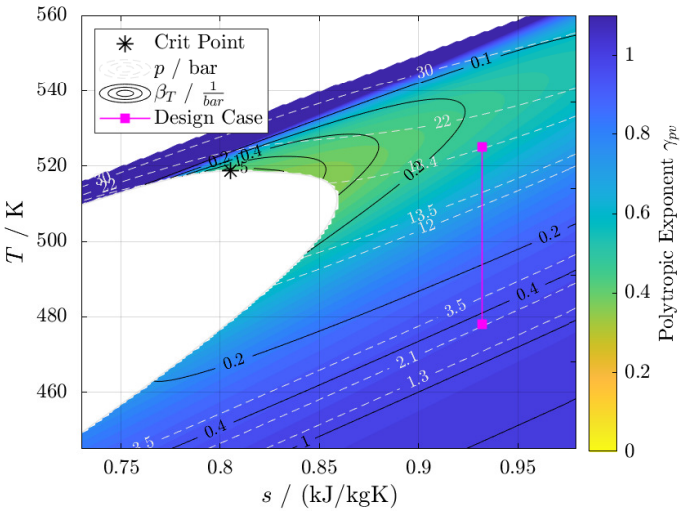

Figure 5.3: Location of the isentrope at design condition of the cascade in the $T-s$ diagram.

Condition	Value
Inlet Total Pressure	18.40 bara
Inlet Total Temperature	252°C
Outlet Static Pressure	1.95 bara

Table 5.1: Boundary conditions used for the design of the linear cascade.

5.2.2. Response Quantities

The experiments designed previously in the ORCHID [34, Chap. 6] resulted in the successful and accurate measurement of *the static pressure* and *the Mach number* distribution, and of *the mass flow rate*. Therefore, this study focuses on the same response quantities, together with the density. The additional direct response quantity, density, is chosen because it can be measured with high accuracy using a Coriolis mass flow or by means of optical techniques. The most interesting flow quantity that can be obtained at the blade surfaces is the pressure distribution since it allows the expansion to be characterized. Figure 5.4 highlights the boundaries and the measuring stations inside the blade row. The direct response quantities are measured in four regions: at the suction and pressure surfaces of the FBN1 blade, in the measuring passage between FBN1 and FBS1 and at the outlet boundary downstream of the blade row, roughly half a chord from the trailing edge. These regions were selected in order to sample the simulation space and to assess if these quantities could be meaningful to measure. The suction and pressure sides of the blades are divided with respect to the minimum and maximum y-value. The periodic boundary represents an approximation of the mid plane of the measuring passage and there the Mach number trend can be calculated. For future studies the spline should be better approximated by choosing the precise mid-plane as the periodic boundary. The outlet is useful to study the wake and the behaviour of the shock waves. In the future the outlet could be used to evaluate entropy generation and efficiency through the pressure loss coefficient.

In Fig. 5.4, the coloured dots represent the measuring stations used along each boundary. The Mach number and the density are extracted at the mid plane of the measuring passage and at the outlet boundary. The expansion wave angles are only calculated along the mid-plane of the measuring passage. The mass flow rate is calculated at the throat using the assumption of 1D flow described in Sec. 4.2.2. Each property is measured at 15 points along the four boundaries, with the exception of the expansion wave angle for which 100 locations are used at the periodic boundary only. The response quantities have a uniform distribution along the boundaries with respect to the y-coordinate except for the measuring passage, for which there is an increased density close to the outlet. This was done in order to better capture the flow features where the wake crosses the boundary.

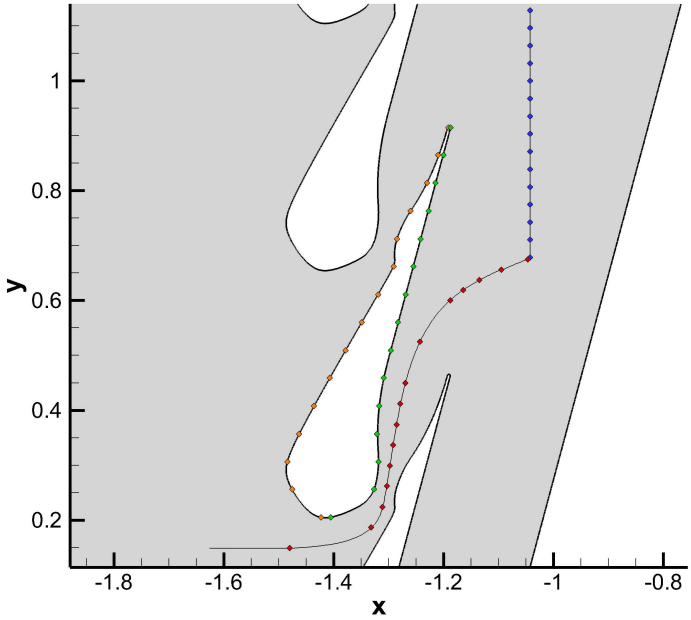

Figure 5.4: Location of the measuring stations along the four boundaries analyzed. The orange and the green points indicate, respectively, the pressure and the suction side of the blade. The red ones indicate the measuring stations along the periodic boundary, while the blue ones the outlet.

5.3. Model Definition

In this section the model parameters used in the study are defined. A convergence study was also conducted which ensured mesh independent results and allowed to define a simulation convergence threshold. The assumptions made for this study are then justified. A dense mesh is needed in order to resolve the complex flow field phenomena such as shock waves, boundary layers, wakes and their interactions. This highlights the importance of optimizing as much as possible the problem in order to make it affordable with the available computational power.

5.3.1. Simulation Set-Up

The simulation set-up will be presented for the single blade chosen to represent the cascade. Only a single blade is used since the cascade was designed to approximate flow periodicity. In Sec. 5.3.4 the flow quantities of the single blade case are compared to the ones of the FBN1 blade of the cascade, which verifies the assumption of flow periodicity.

The flow inside a linear cascade is three dimensional, however, it is possible to simplify the problem if a number of modelling assumptions are verified. A channel height of 8 mm is sufficient to avoid flow blockage effects and to simplify the problem to a 2D plane. In Sec. 5.5.2, the flow quantities of the 2D cascade are compared to the 3D one to verify this statement. The entropy generated inside the boundary layers accounts for 1/3 of the performance loss in turbines [21]. Since the focus of this benchmark test case is on performance metrics, it is important that viscosity is taken into account since boundary layers develop on multiple surfaces.

The simulations were computed using the SU2 v. 5.0 and using a CFD model based on RANS equations. The Spalart-Allmaras model is used to solve the turbulent quantities. The thermophysical properties are computed with the Peng-Robinson model. The advective fluxes are discretized by using the second-order accurate JST scheme. The total conditions are provided at the inlet, and the static pressure at the outlet. The values used are the design condition presented in Tab. 5.1. Giles boundary conditions are used instead of Riemann type, since they provide a special treatment to the domain boundaries to control spurious wave reflections [27]. The top and bottom boundaries of the domain are defined as periodic to approximate a cascade with an infinite number of blades. The blade wall is set-up as adiabatic. The remaining sub-models, such as the transport one, are provided in the complete configuration file in App. A.2.

5.3.2. Mesh Convergence Study

To verify whether the solutions were mesh independent, a mesh convergence study based on bulk averaged system quantities was performed. Five different meshes ranging from 25k to 300k elements were utilized.

Figure 5.5a shows the trailing edge of the 160k elements mesh. At the trailing edge the mesh was refined to better capture the wake. For the mesh convergence study, the cell sizes were scaled proportionally to the initial value defined at each boundary, since the meshes were not uniform. The boundary layer was not modified with the different meshes since the total thickness is dependent on the flow case. The first layer thickness was chosen to maintain y+ below 1.

Figure 5.5b shows the RMS deviation resulting from the mesh convergence study. To calculate this value, the difference between the flow quantities of the chosen mesh and the finest one is calculated, then the root-mean-square of the difference is computed. The mesh chosen, as a trade-off between computational cost and accuracy of the result, is the one with 160k elements. With it, a RMS deviation below 1% for all properties studied with respect to the highest quality mesh can be achieved.

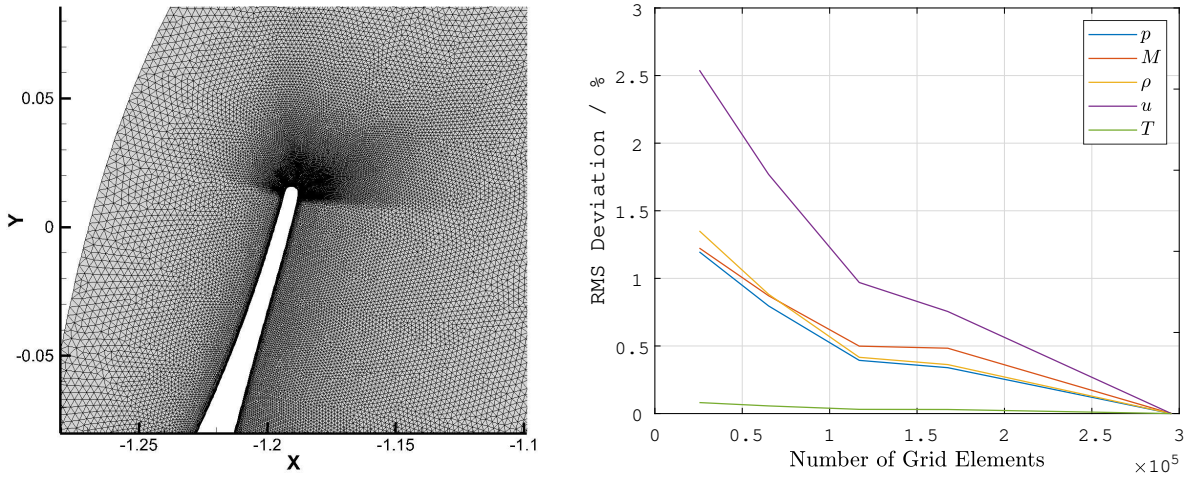

(a) (b)

Figure 5.5: Mesh convergence study of the single blade and a detail view of the trailing edge of the mesh used. **a)** A detail view of the trailing edge of the blade. **b)** Plot of the RMS deviation for five properties and five meshes at the periodic boundary, with respect to the values of the finest one.

5.3.3. Convergence Threshold

Unlike in Chap. 4, convergence close to machine accuracy cannot be achieved in this case. The rho residual level reaches $10^{-6.5}$ after 20k iterations, at which point it is still slowly decreasing. Furthermore, for the stochastic simulations it is necessary to choose a threshold common for all iterations that can be reached in a reasonable amount of time. The procedure defined in Sec. 4.3.4 to determine a convergence threshold for the nozzle was then applied to this case.

To determine the convergence level of the result, three properties available from the simulations were used since they did not require the solution to be calculated. Figure 5.6 shows the entropy generated, the mass flow rate difference between inlet and outlet and the outflow angle. Figure 5.6a shows that at a residual of $10^{-5.5}$, the three properties examined are very close to the converged value. The deviation with respect to the final value at that point is of 4% and 7% higher for the entropy and the mass flow rate difference. The mass flow rate deviation between inlet and outlet at $10^{-5.5}$ is below 1%, which is a commonly used threshold to determine if a result is converged. The outflow angle value converged sooner, so that deviation with respect to the $10^{-6.5}$ threshold is already lower than 0.1%. The number of iterations required to reach $10^{-5.5}$ is one third of the number needed to reach rho equal to $10^{-6.5}$. Figure 5.6b shows the change of the properties between the threshold considered in logarithmic scale. A low deviation indicates that the value is no longer changing considerably. It confirms that the outflow angle converges sooner than the other two properties, and that there is a diminished improvement in the result for the remaining properties after residual 10^{-5}.

The results of this analysis led to the choice of $10^{-5.5}$ as the convergence threshold. From the trial, it was expected that most of the UQ simulations restarting from the converged solutions would take between 2000 and 3000 iteration to reach the residual chosen.

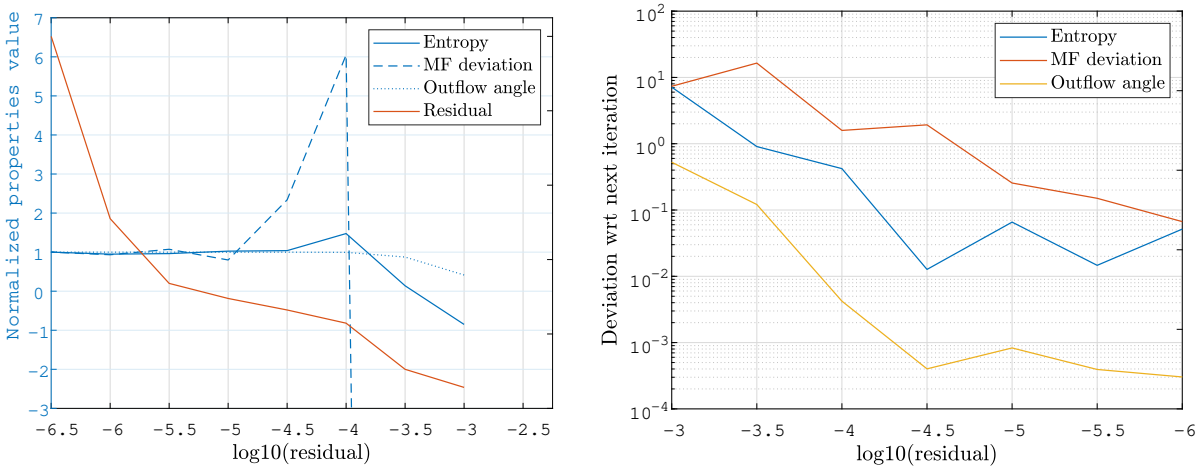

(a) (b)

Figure 5.6: Relation between residual, number of iterations, entropy and mass flow rate (MF) difference between inlet and outlet. **a)** Evolution of the three properties with respect to the residual, together with the normalized number of iterations. **b)** Deviation of the three properties considered with respect to the next residual threshold.

5.3.4. Verification of the Periodicity Assumption

Truly periodic conditions require an infinite number of blades. Due to mass flow rate restrictions, a lower number is used. According to the best practices documented in Hirsch [36, Pg. 13], five blades should be adequate to approximate flow periodicity. To verify this assumption, flow quantities of the cascade blade row were compared to the single blade domain. The flow quantities at blade FBN1 and at the mid-plane of the measuring passage were compared. Being located far from the cascade walls, these boundaries are expected to best approximate the periodic condition. The flow domain was added to the Tecplot interface and through linear interpolation the values were extracted. The values were then compared for the pressure and, where possible, the Mach number.

Figure 5.7 shows the Mach field of the cascade and the single blade. Figure 5.7a highlights with blue circles the reflected shock wave which is only present in the cascade blade row and not in the single blade. The shock wave is reflected from the cascade wall, it originates at the trailing edge of FBS2. The reflected shock wave is located at the same position as the wake of FBS1, this has a significant effect on the Mach number at the location.

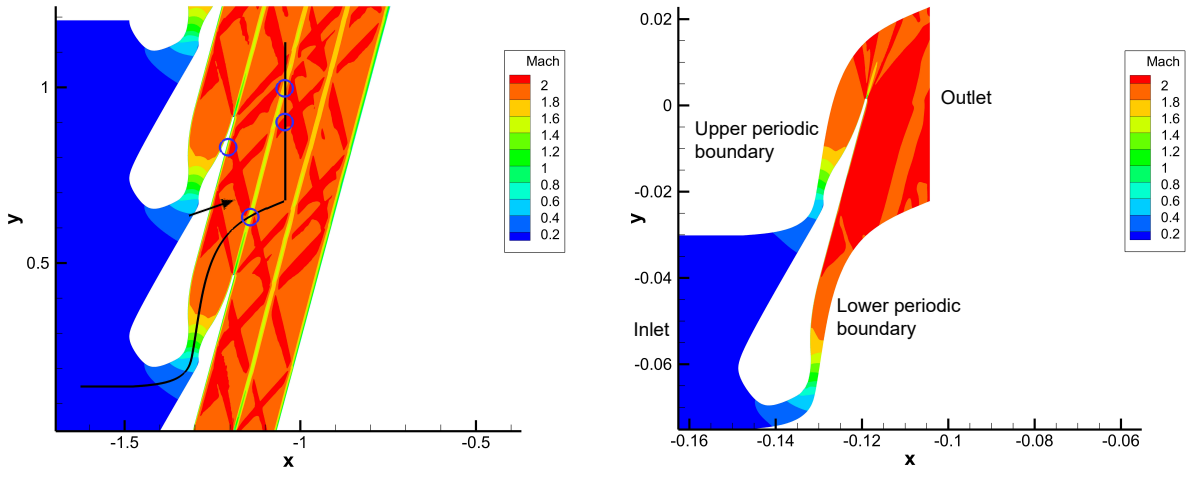

(a) (b)

Figure 5.7: SU2 simulations showing the Mach field of the cascade and of the single blade. **a)** Mach number for the cascade blade row. Highlighted in black are the periodic and the outlet coincident with the boundaries of the single blade shown in (b). The blue circles show the location of the reflected shock waves from the cascade wall. This shock wave originates from the trailing edge of FBS2. **b)** Mach number for the single blade.

Figure 5.8 shows the quantitative comparison between the pressure at the blade surfaces and the mid flow passage Mach number. Figure 5.8a shows the static pressure distribution at the blade surfaces, the difference between the full cascade and the single blade is minimal. The deviation, shown in Fig. 5.8b, presents a few peaks which only reach around 4 % of the inlet pressure. The deviation at 0.05 m is due to the reflected shock wave.

Figure 5.8c refers to the mid flow passage Mach number. The match is generally good, with the exception of the large deviation close to the outlet. There, the shock wave reflected from the cascade wall, not present in the single blade analysis, crosses the boundary at the location of the wake. This leads to a large decrease in the Mach number because of the combination of the two effects. Figure 5.8d, which is showing the Mach number at the outlet, clearly highlights the presence of the shock wave crossing the wake. The smaller peaks in the two Mach plots are due to the presence of shock waves crossing the domain.

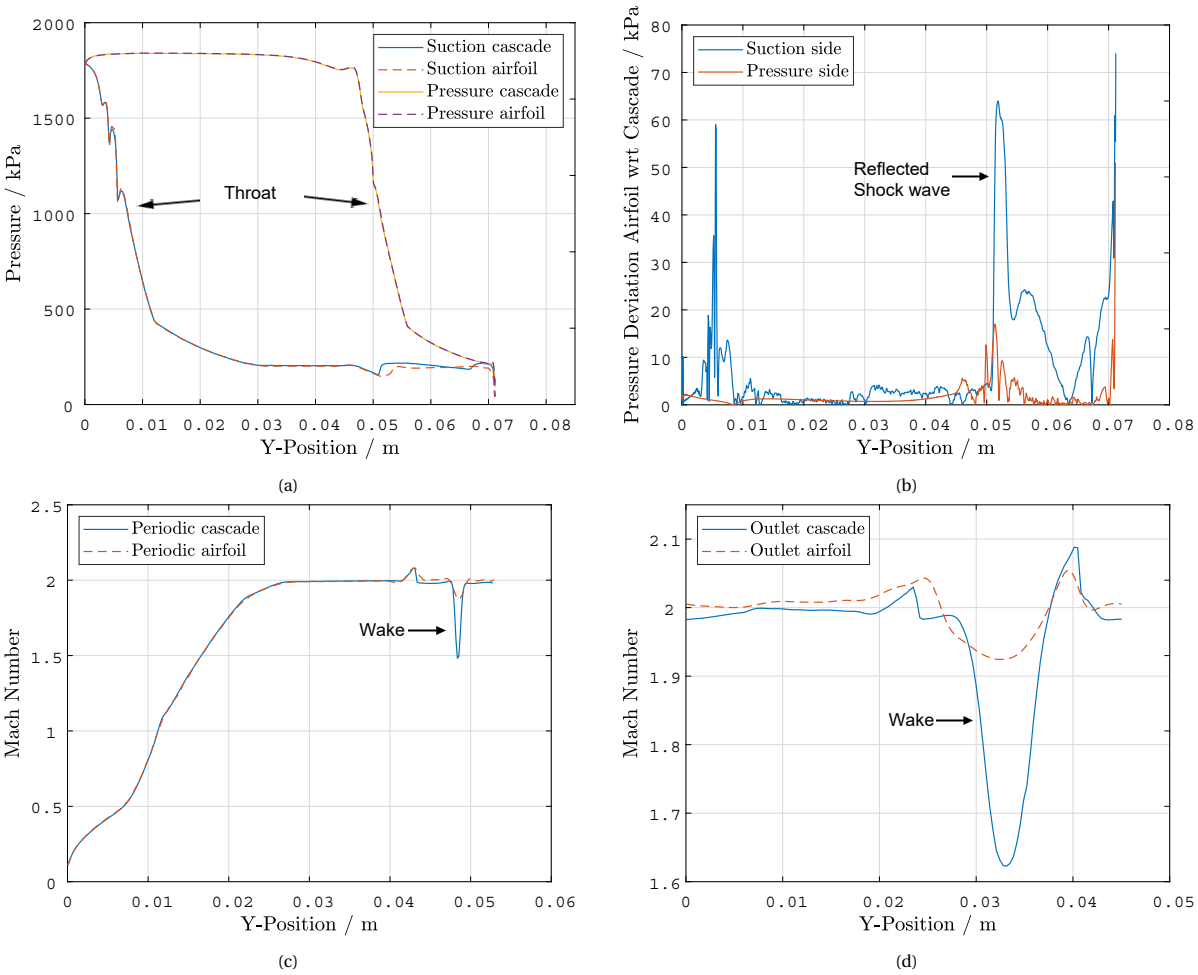

Figure 5.8: Comparison of the pressure and the Mach number distribution between the single blade and the FBN1 blade of the cascade, for the four surfaces considered. **a)** Pressure plot for the blade surfaces. **b)** Pressure absolute deviation plot for the blade surfaces. **c)** Mach number plot at the mid-plane of the measuring passage. **d)** Mach number plot at the outlet. The wake is influenced by the reflected shock wave which first crossed the mid-plane.

In conclusion, using a single blade in place of the complete cascade is acceptable for the response quantities extracted from the blade surface and in the mid of the flow passage. For the outlet, the solution differs mainly because of the interaction between the reflected shock wave and the wake, which drastically decreases the Mach number. A solution to decouple the effect of the shock wave from that of the wake could be changing the position of the outlet boundary, where the two are separated. In general, the two results match very well, but caution should be taken with the region downstream of the blade since the reflected shock wave can modify the flow.

5.3.5. Comparison between Upwind and Central-Differencing Schemes for NICFD Flows

The numerical scheme is known to affect the solution of simulations, particularly when shock phenomena are present such as in the case considered. Similarly to what was done in Sec. 4.3.6, a comparison was made between flow quantities of the single blade solution using the JST and ROE with MUSCL numerical scheme for discretizing the advective fluxes.

The comparison was performed for the pressure, but the same conclusions can be applied to the other response quantities. The case studied is the design operating point of the cascade. The convergence threshold was defined as rho residual of 10^{-6}.

Figure 5.9 shows the predictions of the pressure along the four surfaces using the JST and the ROE numerical schemes. In Fig. 5.9a, the pressure distribution at the two surfaces of the blade calculated with both schemes are superimposed. The noticeable differences between the two are minimal, small discrepancies can be seen at the throat and at the impinging shock wave location along the suction surface. In Fig. 5.9b the pressure deviation is plotted, spikes up to 65 kPa can be seen. The locations correspond to the points where the gradient of the flow quantities is the largest, such as the throat and at the shock wave impinging point. At the throat and at the impinging shock wave point the relative deviation of the pressure is limited to 4% of the total pressure. The spike at the trailing edge matches the position of an expansion fan. A close look at the wake region shows that the gradients are sharper in the JST case. Similar considerations can be made for Fig. 5.9c and 5.9d where the periodic and the outlet deviation are plotted, there the maximum deviation reached is of 5% in a single point.

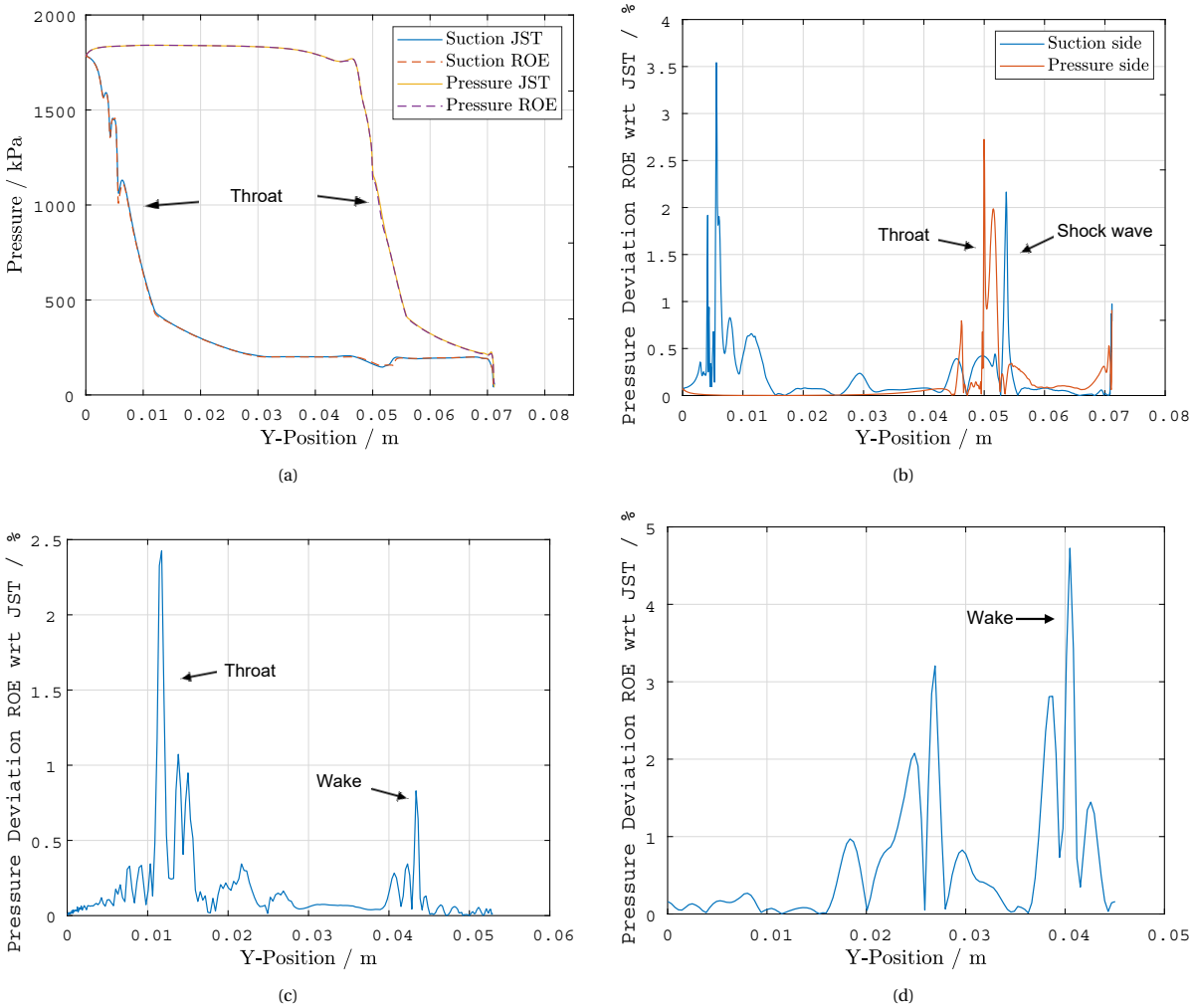

Figure 5.9: Pressure plot comparing the use of the JST and of the ROE numerical schemes. **a)** Pressure at the suction and at the pressure side of the blade. **b)** Pressure deviation between JST and ROE for suction and pressure sides. **c)** Pressure deviation at the periodic boundary. **d)** Pressure deviation at the outlet.

In conclusion, the comparison shows that in the blade test case the two solutions are equivalent. Noticeable differences are present at few locations where the deviation can peak at 5% of the total pressure. These points are located where the gradient of the properties are the highest, at shock impingement locations and at the wake. In the blade case the deviation in the pressure is on the same order of magnitude as the total expanded uncertainty presented in Sec. 5.5.1, so the scheme choice might have an influence in the assessment of the flow quantities and it should be taken into account. The JST scheme is preferred since in this case it has better convergence behaviour.

5.4. Characterization of Model Derived Uncertainties

In this chapter the model uncertainties from the simulations will be presented. The procedure to be used in the actual validation will also be briefly presented. Then the preliminary results of the simulation uncertainties, for example, the expanded uncertainty of pressure, density and Mach number due to the numerical and input uncertainties, will be commented.

5.4.1. Model Definition, Procedure and UQ Infrastructure

The procedure followed to generate the data to validate the flow solver for the cascade blade row unit case closely follows the one for the nozzle unit case presented in Sec. 4.4.1. The results of a series of deterministic simulations are compared to calculate the expanded numerical uncertainty, through a stochastic simulation the response quantities and their expanded uncertainties due to the inputs can be extracted. The responses are compared to the pseudo-experimental data with the V&V20, Romero and Hills model to determine whether a model error is present. Since the nature of this chapter is a preliminary study of the cascade, no experimental data is generated and so the validation is not completed. This assessment will only consider the numerical and the input uncertainty.

The examined test case is the flow expansion at cascade nominal operating conditions. The boundary conditions used are an inlet total pressure of 18.4 bar and an inlet total temperature of 525.15 K. The outlet static pressure is 1.95 bar. The unstructured mesh used has 160k elements, unless otherwise stated. The advective scheme is JST. The convergence threshold is rho residual equal to $10^{-5.5}$.

As described in Sec. 5.2.2, the pressure, the density and the Mach number are sampled at 15 different locations of the four surfaces. The mass flow rate is calculated only at the throat at the mid-plane of the measuring passage.

5.4.2. Expanded Numerical Uncertainty

The expanded uncertainties of the pressure and the Mach number due to the numerical uncertainty are calculated with Refresco [43]. The five meshes, with 25k to 300k elements, generated for the convergence study were used. Figure 5.10 shows the absolute numerical uncertainty of the pressure and the Mach number response quantities. These values, when compared to the results of an isentropic expansion in a de Laval nozzle (see Sec. 4.4.2), are one order of magnitude higher. Figure 5.10a, 5.10b and 5.10c shows that he highest spikes in uncertainty are found at the throat, where they reach between 30 and 65 kPa. This is expected since in that region the pressure gradient is large. Another noticeable region is the wake in Fig. 5.10d, which leads to a limited increase in the uncertainty. Figures 5.10c and 5.10d show the pressure and the Mach number distribution at the periodic boundary. It is interesting to notice that while the impinging shock wave towards the end of the periodic boundary leads to an almost negligible increase in the pressure uncertainty, this is not the case for the Mach number where the peak is higher and almost match the throat uncertainty. This is probably due to the larger variation in the Mach number in the presence of shock wave with respect to the change in the pressure. This also highlights the importance of improving the mesh locally if the Mach number is being studied. A final note is that the last measuring station of the blade surfaces, placed at 0.07 m in the wake, was not plotted since the uncertainty was extremely high at around 300 kPa. This is probably due to the large gradient of properties in the wake which would require a much finer mesh to decrease the uncertainty. A possibility is that the use of the JST scheme in the different meshes, which is very sensitive to the gradients, may drastically influence the location of the shock phenomena.

5.4.3. Expanded Input Uncertainty

The expanded uncertainties of the pressure and the Mach number U_{in} due to the uncertainty in the model inputs are calculated using an UQ framework. A stochastic collocation method is used since it was proved to accurately represent the expanded uncertainties while requiring less iterations than the Monte Carlo sam-

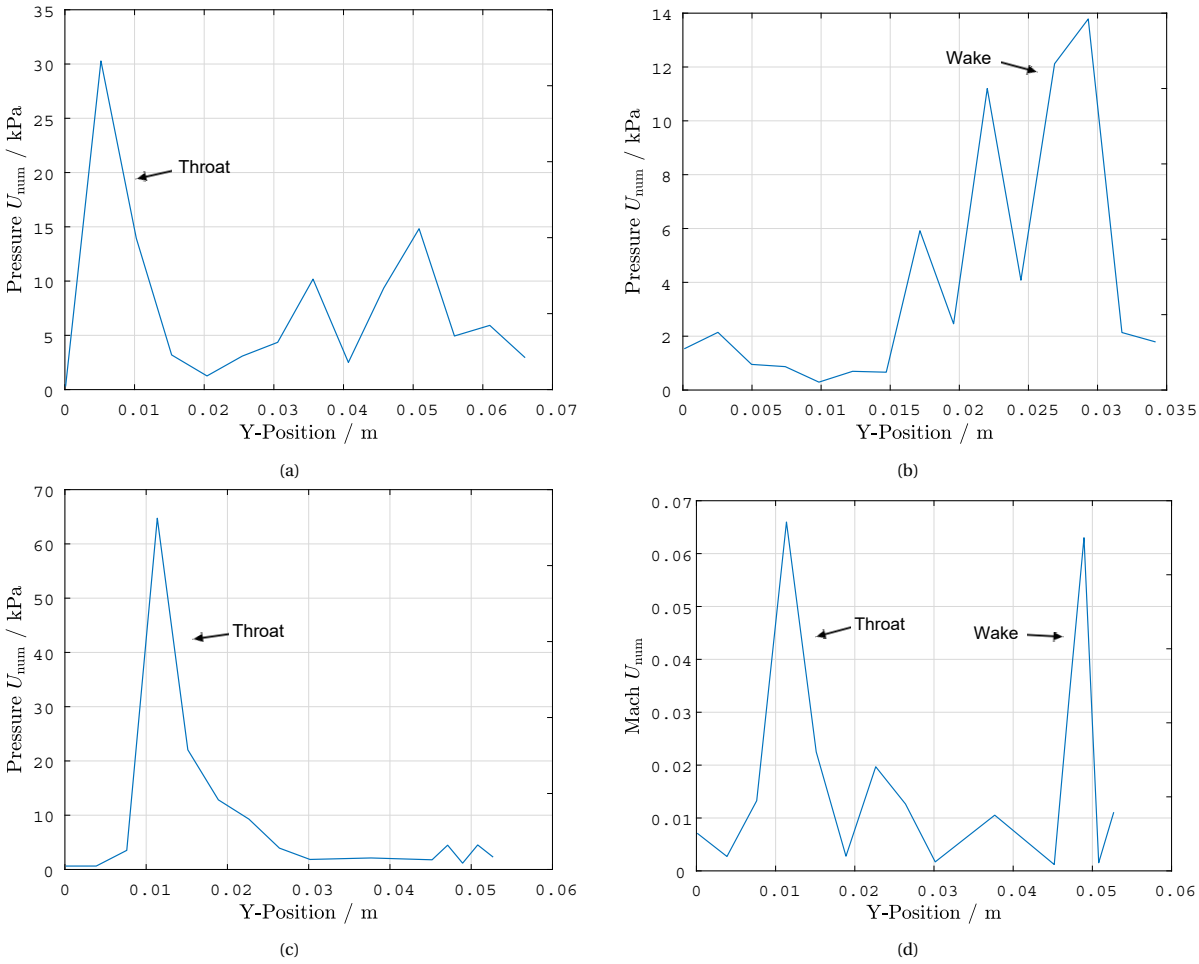

Figure 5.10: Expanded uncertainty of the direct response quantities Mach number and the Pressure derived from the numerical uncertainty U_{num}. **a)** Pressure uncertainty plot for the blade suction surface. **b)** Pressure uncertainty plot for the outlet. **c)** Pressure numerical uncertainty plot for the blade periodic boundary. **d)** Mach number uncertainty plot for the periodic boundary.

pling, see Sec. 4.4.3. The 95% confidence level uncertainties in the inputs are listed in Tab. 5.2. The outlet pressure is an addition with respect to the nozzle unit case since it is expected to have an influence on the position of the shock waves.

Figure 5.11 shows the expanded uncertainty of the static pressure distribution along the blade and the mid-plane measuring passage Mach number and density, with associated Sobol indices. Figure 5.11a presents the static pressure plot, the general trend is of a low uncertainty in relative terms, even at critical locations such as the throat. The flow features of interest, such as the impinging shock wave on the suction side and the blade trailing edge, are captured and are indicated in the figure. It can be noticed that these point have a very low uncertainty, which means that the shock wave behaviour is weakly influenced by the input considered. The related Sobol plot, Fig. 5.11b, for the pressure side, in the subsonic part where the uncertainty is low, the leading contribution is the total pressure. This quickly changes close to the throat where the predominant input becomes the critical pressure and the outlet back pressure. The latest consideration is related to the measuring stations located in the wake, there all the Sobol numbers are below zero. This does not make physical sense, the reason suggested in Qian and Mahdi [56] is the presence of large approximation deviation which can only be fixed by increasing the number of samples. Considering the problematic behaviour at the same location for the numerical uncertainty, it could also be a problem related to insufficient mesh density which lead to results which cannot be related to the specific input.

Figure 5.11c shows the measuring passage mid-plane Mach number. The main observation is the negligible uncertainty at the throat, since independently from the conditions it will always be at Mach one. The uncertainty is moderately high at the other locations and at the wake the Mach number is clearly lower. The last case is also characterized by a high uncertainty which indicates that the magnitude of the wake can change

Table 5.2: Total expanded uncertainty of the input data of the thermodynamic model of MM and of the boundary conditions for the flow simulation. The distribution of the uncertainty is assumed uniform for the fluid model parameters and normal for the boundary conditions of the flow solver.

Parameter	Nominal value	% uncertainty
Peng-Robinson thermodynamic model [14]		
T_{cr} / K	518.7	$\pm 3^{*}$ [61]
P_{cr} / bar	19.40	$\pm 5^{*}$ [61]
Boundary Conditions (BC)		
T_0 / K	525.15	$\pm 0.2^{+}$
P_0 / bar	18.40	$\pm 0.5^{+}$
P_{out} / bar	1.95	$\pm 0.5^{+}$

* Experimental. $^{+}$ Assumed.

considerably. Shown in Fig. 5.11d are the Sobol indices which presents a constant trend, and they confirm once more the importance of the critical pressure and of the outlet static pressure on the Mach number uncertainty. The zero Sobol indices at the throat are due to the very low uncertainty there, which prevent Dakota [1] from defining the relative influence of the input.

The expanded uncertainty of the density, shown in Fig. 5.11e, was plotted to highlight its sensitivity to the critical properties in the converging part of the nozzle. This could be exploited in the future to calibrate the thermodynamic model when the experimental infrastructure to detect the density will be available [34].

Figures 5.11b and 5.11d show that, like in the nozzle case, the least influential parameter is the total pressure. The total temperature also had limited importance. The Sobol index of the total pressure is non-negligible only for the pressure response quantities in the subsonic part of the cascade. There the expanded input uncertainty is low, so the inference is that the total pressure is relevant only because the expanded uncertainties due to the other inputs are negligible. In conclusion, for complex cases where the number of input parameters has to be limited to minimize the computational time, the input total pressure can be removed as an input to the UQ problem. In the case considered, going from five to four different input would reduce the number of total iterations from 382 to 211.

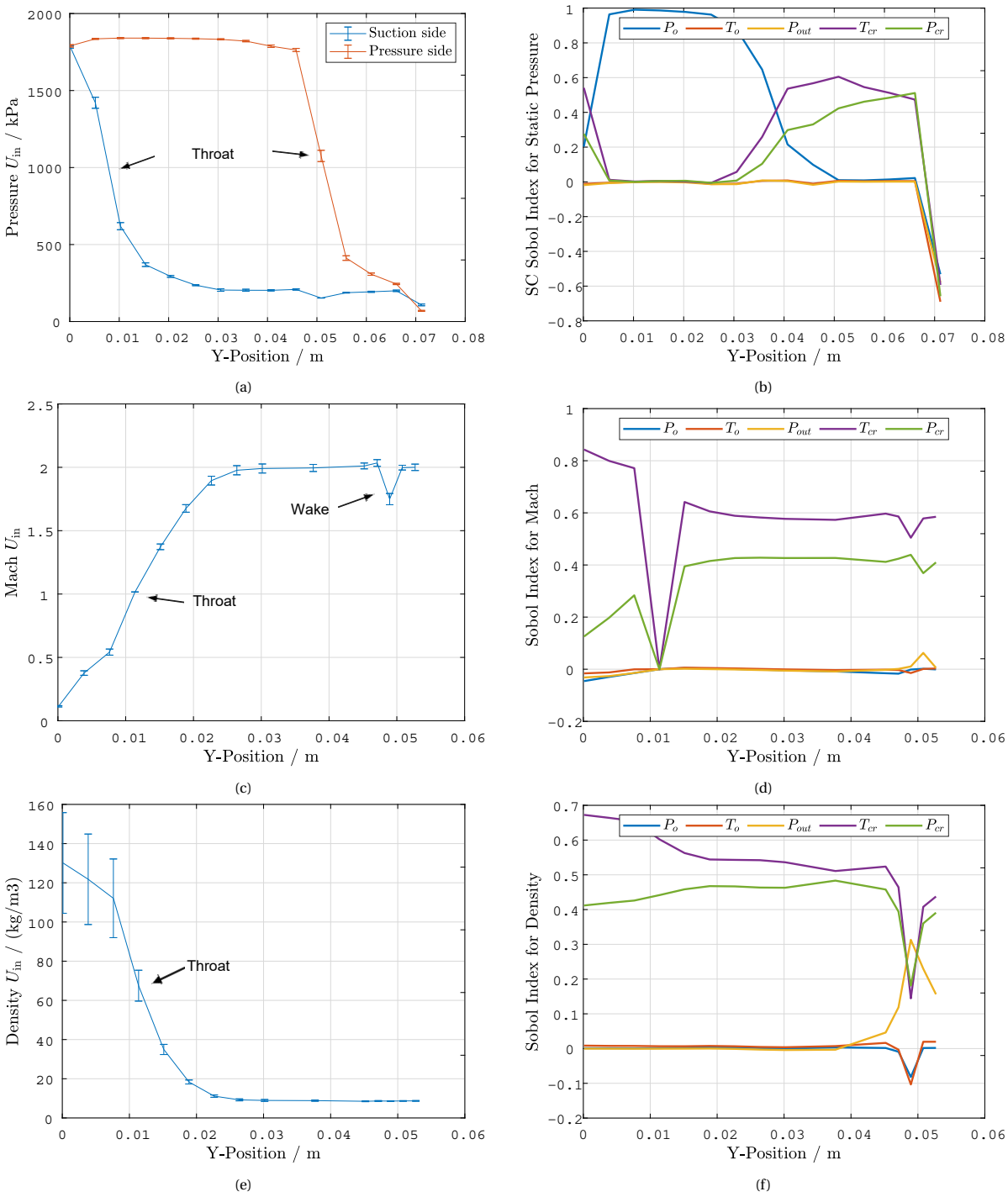

Figure 5.11: Expanded uncertainty of the direct response quantities pressure, density and Mach number. These uncertainties are purely derived from the input uncertainties U_{in}, see Tab. 5.2. The relative importance of the variables are shown with their Sobol indices. **a)** Blade pressure distribution of the pressure and the suction side with associated 2-sigma uncertainty. **b)** Sobol indices of the pressure side of the blade. **c)** Mach number at the measuring passage mid-plane with associated 2-sigma uncertainty. **d)** Sobol indices of the Mach number at the measuring passage mid-plane. **e)** Density plot at the measuring passage mid-plane with associated 2-sigma uncertainty. **f)** Sobol indices of the density at the measuring passage mid-plane.

5.5. Verification Assessment

The two expanded uncertainties available, derived from U_{num} and U_{in}, were combined to determine the total expanded uncertainties.

5.5.1. Total Expanded Uncertainties

The total expanded uncertainty, defined as $U_{val} = \sqrt{U_{num}^2 + U_{in}^2}$, for the pressure and the Mach number distribution is presented. Since no experimental data is available, the related uncertainty is not considered.

Figure 5.12 shows the validation uncertainty at the four surfaces considered for the static pressure. Figures 5.12a and 5.12b show that, respectively for the suction and the pressure side of the blade, the baseline validation uncertainty is around 0.5% of the inlet total pressure, which is comparable to the nozzle results. The largest peaks, between 2.7% and 3.8% of the inlet total pressure, are found at the throat of the first three boundaries. A smaller peak, roughly 0.8% of the inlet total pressure, is in the wake of the outlet. The uncertainty at the blade surfaces is evenly distributed between the numerical and the input uncertainty. At the periodic and at the outlet the numerical uncertainty is the largest component. This is expected since the mesh quality at the periodic boundary and at the outlet is lower than an at the blade wall.

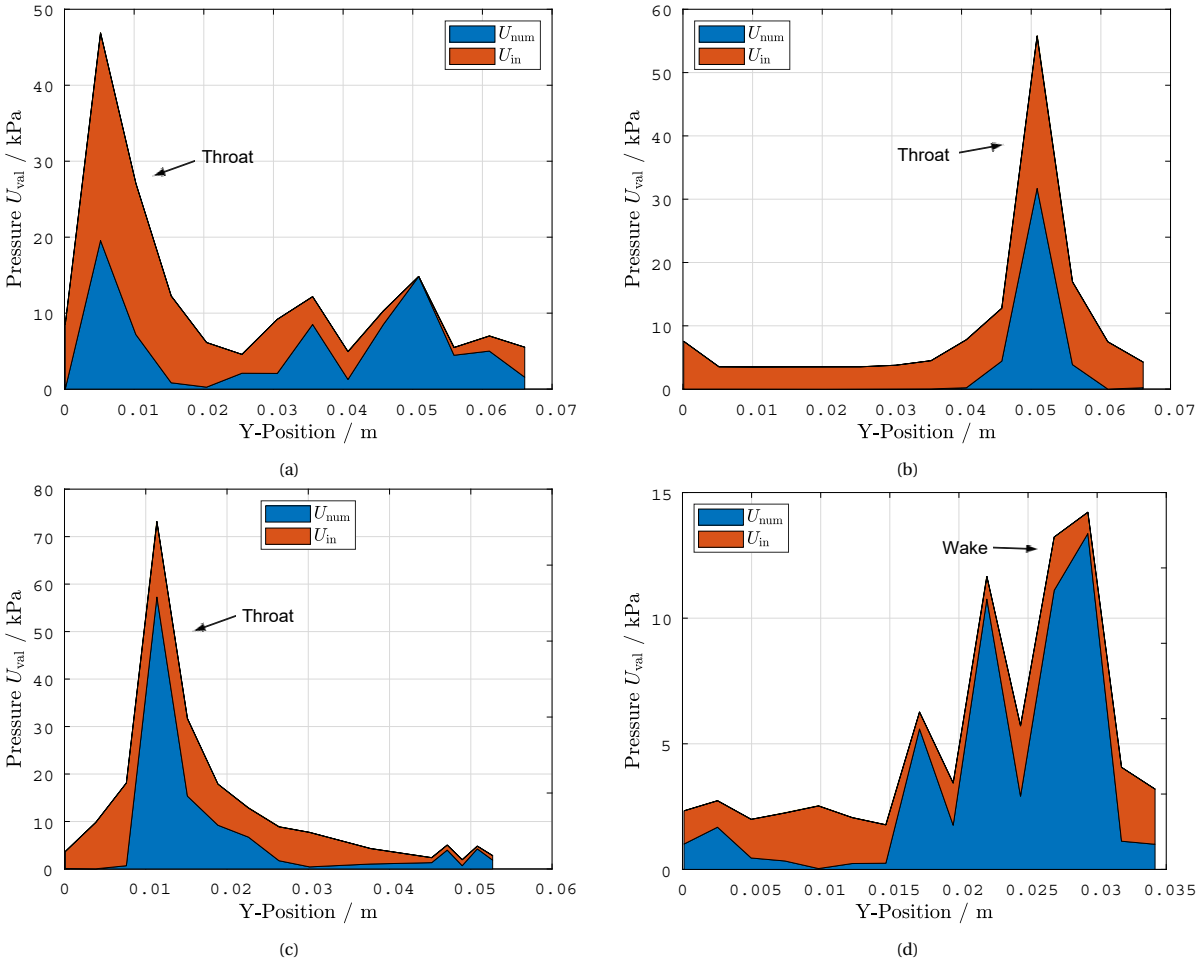

Figure 5.12: Total expanded uncertainty (U_{val}) for the pressure distribution predicted along the four boundaries. **a)** The blade suction surface. **b)** The blade pressure surface. **c)** The blade periodic boundary. **d)** The outlet.

Figure 5.13 shows the validation uncertainty for the Mach number at the periodic and at the outlet. Along the periodic boundary the validation uncertainty is roughly constant, but the main contributor to the expanded uncertainty differs. The uncertainty of the input is the most important contribution at all points except for the throat and the wake, there the numerical expanded uncertainty takes the largest share. The outlet has a large peak at the wake location mostly due to the numerical uncertainty.

The expanded uncertainty of the mass flow rate was also calculated. This parameter was estimated for the four channels of the cascade blade row and for a thickness of the domain of 8 mm. The results are presented in Tab. 5.3. The two uncertainties are comparable in magnitude and combined they lead to an deviation of 1.75% with respect to the mass flow rate.

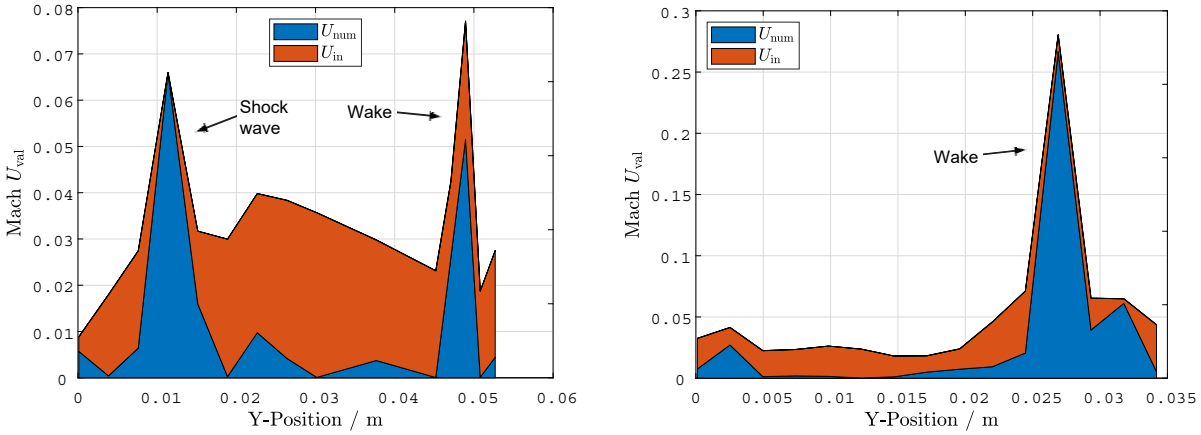

Figure 5.13: Total expanded uncertainty (U_{val}) for the Mach number predicted along the periodic and outlet boundary. **a)** The periodic boundary. **b)** The outlet.

Table 5.3: Estimate of the mass flow rate across the four channels of the cascade. The numerical and the input uncertainties are also presented.

	Value
Simulation S	1.1903 kg/s
U_{num}	±0.0179 kg/s
U_{in}	±0.0106 kg/s
U_{val}	±0.0208 kg/s

5.5.2. Verification Against Results from a Commercial Solver

In this section a pseudo-validation will be performed by comparing the flow quantities obtained with results from the SU2 simulations with a deterministic simulation generated from a state-of-the-art CFD software. The pseudo-experimental data was generated with CFX, the thermodynamic properties were calculated through RefProp, the most accurate thermodynamic model available, using a multiparameter EoS. The comparison is made between the single airfoil 2D domain and the full 3D cascade blade row shown in Fig. 5.2, the 3D mesh is made of 80 million elements. The pseudo-experimental data does not have an experimental uncertainty associated.

Figure 5.14 highlights the results obtained. E is the comparison error given by $E = S - D$, where S is the simulation result coming from SU2 and D is the pseudo experimental result coming from CFX. U_{val} represents the total uncertainty given by $U_{val} = \sqrt{U_{num}^2 + U_{in}^2}$. The deviation remains low at most points with the exception of the throat and at the reflected shock wave points. Figure 5.14a shows how the deviation in pressure at the blade suction surface remains below the total expanded uncertainty, with the exception of the throat and the shock wave impingement location. This indicates that the change in the thermodynamic model does not strongly affects the pressure. The large deviation at the throat is due to to the different interpolation methods used by the software to generate the blade mesh, it does not modify the flow in any other way. The error increase due to the reflected shock wave from the cascade wall is significant, around 4% of the total pressure. Figure 5.14b shows the trends of the Mach number at the measuring passage mid-plane. The comparison is good with the exception of the wake point, in the cascade the reflected shock wave is at the same location and it leads to a decrease in the Mach number. Finally, Fig. 5.14c shows the Mach number at the outlet. This boundary is important since it could be used as measurement plane which could facilitate the calculation of performance metrics. This could then lead to a way to characterize the efficiency of the blade. The deviation there is generally close to the total expanded uncertainty. At the wake, despite the large uncertainty, the deviation is low. Instead, the reflected shock wave from the cascade wall leads to a deviation of 0.2.

The infrastructure proved to be adequate to validate the flow solver for the flow physics in a linear cascade. The total uncertainty is generally low enough to allow a meaningful comparison of the flow quantities of interest. The five blades of the cascade should be adequate to approximate flow periodicity.

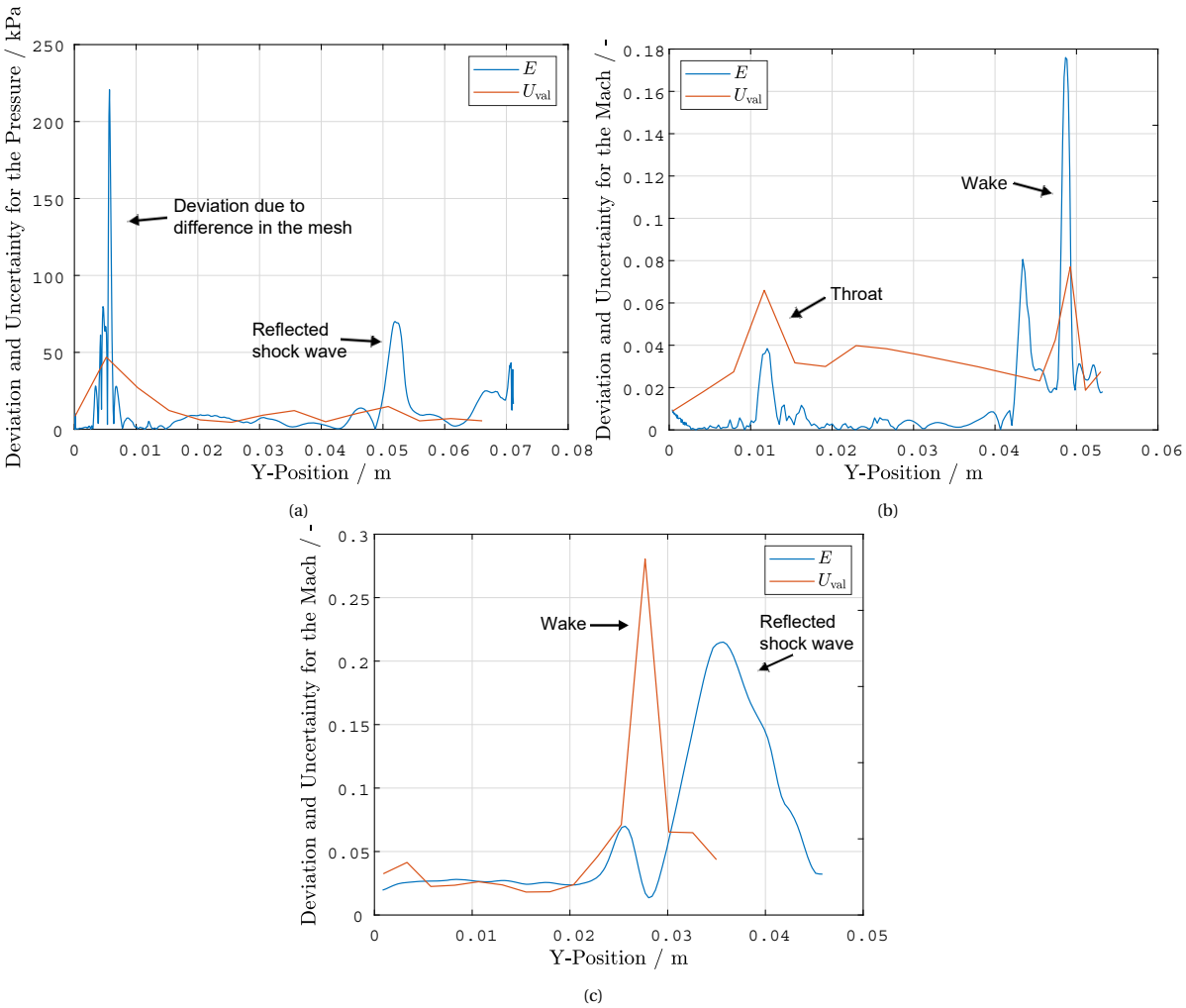

Figure 5.14: Verification with the V&V20 framework of the relation between uncertainty and deviation between the SU2 and the CFX simulation for selected boundaries. **a)** Static pressure uncertainty and deviation along the suction side of the blade. **b)** Mach number uncertainty and deviation along the periodic boundary. **c)** Mach number uncertainty and deviation along the outlet.

5.5.3. Lessons Learned from the V&V of the SU2 Solver

In this section, some suggestions to improve the simulations are made.

- In all the boundaries examined a consistent part of the uncertainty is due to the grid discretization which can be at least partly reduced with the use of a denser mesh.
- If the experimental uncertainty will be the same as the one measured during the experiments in the nozzle, the influence on the total uncertainty of the static pressure would be negligible. Instead for the Mach response quantities the expected experimental uncertainty is estimated to be higher than the other two sources combined. Figure 5.15 shows the total expanded uncertainty, including an estimate of the experimental one, for the Mach number at the periodic boundary and at the outlet.
- The response quantities provided by the measuring station located at the blade trailing edge showed a very large expanded numerical uncertainty, around 300 kPa. A refinement of the trailing edge mesh could be made to have obtain meaningful results.
- As highlighted in Sec. 5.4.3, the total pressure and the total temperature, have a very limited influence on most of the response quantities during the UQ. The main exception is at measurement locations in the subsonic section of the stator, where the overall expanded uncertainty is generally low. If the computing time needs to be reduced it is suggested to remove them from any further study.

- When the transport and the thermal model will be assessed, the model's parameters such as the viscosity and the thermal conductivity constant could be added to the UQ inputs. Their influence on the response quantities uncertainty could be studied.
- The periodic boundary currently defined does not match the mid-plane of the measuring passage of the cascade blade row. For a more rigorous study of the Mach trend the actual mid-plane of the measuring passage should be used.
- The comparison between JST and ROE numerical schemes indicates ideal locations for measuring stations. At these locations the predicted property gradients are large and explains why there is a deviation in the prediction of pressure along the blade surface. In the future, if accurate experimental data can be gathered at those points, an assessment of the numerical schemes could be performed.

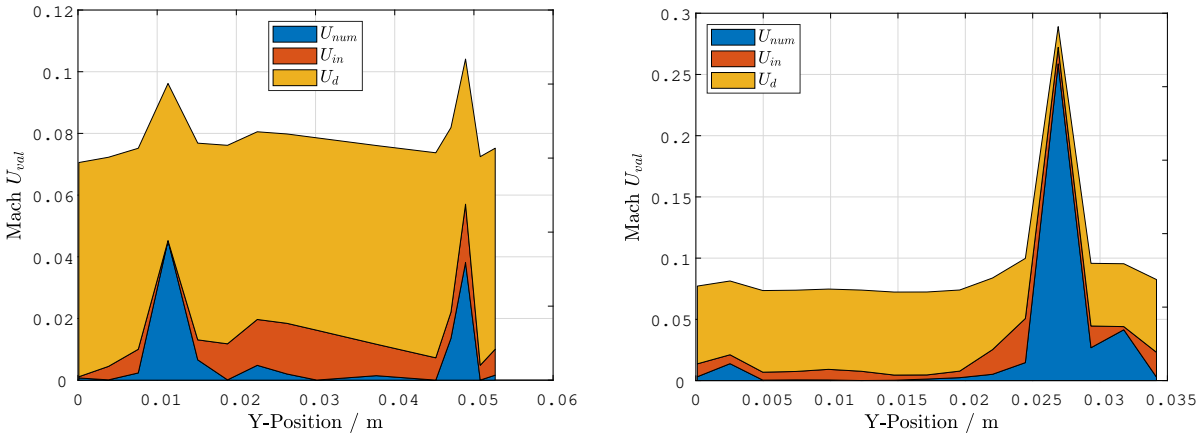

(a) (b)

Figure 5.15: Mach number total expanded uncertainty (U_{val}) including the estimated experimental uncertainty for the periodic boundary and the outlet. **a)** The periodic boundary. **b)** The outlet.

5.5.4. Take-Aways for the Actual Experimental Campaign

In this section, suggestions on how the future experimental campaigns could be designed are presented.

- The experimental uncertainty is expected to be important in the assessment of the Mach number since it already reaches Mach 0.1 in the nozzle case, a much higher level than the other two sources combined. Efforts should be made to lower it to make the validation meaningful;
- If the experimental uncertainty of the pressure remains in the same order of magnitude as in the nozzle experiments, around 5 kPa, its share of the total uncertainty should remain low with respect to the other sources combined, making it a suitable flow quantities to assess;
- The current position of the measuring stations seems to adequately capture the flow phenomena of interest. To increase the resolution at the shock waves and the wake, an higher density of measuring stations could be used where these are present;
- The position of the measuring station at the blade trailing edge should be improved. They could be positioned along the wake to study it;
- The sensitivity of the density to the critical properties should be exploited to calibrate the thermodynamic model by collecting experimental data;
- The measuring stations at the outlet should be positioned to avoid the reflected shock wave from the cascade wall; and,
- When system response quantities, such as the efficiency, will be studied, static pressure probes could be positioned at the outlet boundary to estimate the pressure losses.

6

Conclusions

The contributions documented in this thesis have provided critical insights to the validation of the SU2 flow solver for non-ideal compressible flows of organic fluids. In particular, Chap. 2 presented a refined validation hierarchy for ORC turbomachinery and critically assessed the use of various validation metrics. Chapter 3 documented the numerical infrastructure adopted to facilitate the UQ analysis which enabled to quantify the numerical uncertainty of the various test cases. Furthermore, an assessment of different thermodynamic models was performed. The maps generated allowed to define a region where to focus the experiments and to define the boundary conditions of the case to perform in the de Laval nozzle.

In Chap. 4, two unit tests were run in a supersonic nozzle. First, the comparison between experiments and simulations was performed for an isentropic expansion at design condition. The static pressure at the top wall, the Mach number at the center line and the mass flow rate were compared with experimental data. Then, a wedge was inserted in the nozzle outlet to generate a shock wave that was then measured. The validation was performed with the V&V 20 ASME [5] model and the Real Space Romero [60] model. In addition, the Hills model [35] was used to determine a global metric to establish the outcome of the assessment.

In Chap. 5, the cascade blade row case was assessed to define the future experimental campaigns. The response quantities of interest were identified and recommendations were made to improve the model used for the validation. The deterministic and stochastic simulations necessary to generate the expanded numerical and input uncertainties were run. No experimental data is currently available, so the results were verified with the state-of-the-art CFD software.

6.1. Research Answers

The main research question formulated in Chap. 1 was **"Can the SU2 flow solver accurately predict complex flow structures in the NICFD regime?"**

To adequately answer this question, more detailed sub-questions were made which closely relate to the work done.

1. **What is the domain of applicability of the Peng-Robinson equation of state?**

   Through a series of operating maps, the applicability range of different equations of state was defined. The density and the speed of sound predicted by two cubic equations of state, the Peng-Robinsion polytropic EoS and the iPRSV non-polytropic EoS, with respect to the reference model, RefProp, were compared.

   Overall, the largest deviations were present in the liquid and in the supercritical region where the deviation between the two cubic EoS and RefProp was over 20%. Focusing on the vapour region which is more important for turbomachinery cases, for any combination of pressure and temperature below 30 bar and 570 K, the deviation of the density did not exceed 7%. The Peng-Robinson equation has its minimum deviation with respect to the RefProp prediction at the vapour saturation line.

   A comparison was also performed between the Peng-Robinson polytropic EoS and the iPRSV non-polytropic EoS to determine whether a relevant difference between the two existed. The deviation in the density was found to be minimal, below 0.1%, across all the domain considered with the exception

of the region around the critical point. There, a deviation over 1% was found where the iPRSV better approximated the reference model results. Nonetheless, turbomachines usually do not operate so close to the critical point so the difference can be considered irrelevant in the choice of the equation. To quantify the difference between the polytropic and the non-polytropic feature of the thermodynamic model existed, the speed of sound was also compared. Again, the deviation was higher than 1% only in proximity of the critical point, and lower that 0.1% across all the vapour region. The diagrams and more considerations are presented in Sec. 3.3.2.

2. **How accurately can SU2 predict shock-wave angles and is it possible to characterize the associated uncertainties?**

   The shock wave angle generated by a 2.5° wedge inserted in a Mach 2.0 flow was examined. The results were positive since the comparison error between the simulation and the experiment was only 0.56% of the shock wave angle measured, lower than the total expanded uncertainty of 1.79%. The experiment was not executed at the nozzle design conditions, but at an inlet total temperature and pressure of $T_0 = 180°C$ and $P_0 = 3.5$ bara to a back pressure of $P_{out} = 1.0$ bara. Nonetheless, as long as there is flow similarity at the leading point of the wedge, same Mach number, the angle predicted will not differ from the on-design conditions. This assumption is supported by simulations and should be checked in the future experiments.

   A comparison of pressure distribution, Mach number distribution and mass flow rate at design conditions, inlet total temperature and pressure of $T_0 = 252°C$ and $P_0 = 18.4$ bara to a back pressure of $P_{out} = 2.1$ bara, was performed with the updated UQ infrastructure. The first response quantity was generated with state-of-the-art CFD software, while the others were coming from experiments. The pressure shows a good agreement with respect to the SU2 result across all the nozzle length. The Mach number instead presents a large comparison error in the kernel region, while at the outlet experiments and simulations are again in agreement. An hypothesis to explain the mismatch could be the deviation of the Peng-Robinson EoS with respect to more accurate models. The mass flow rate shows an error which is four time higher than the uncertainty, a new meter in the ORCHID will be used to investigate this error. The results are presented in Sec. 4.8.

3. **Is the flow solver able to predict the physics of the flow around more complicated shapes, such as a blade row?**

   The validation infrastructure was successfully adapted to handle the linear cascade case. This study only evaluated direct response quantities, but in the future it will be possible to extend the infrastructure to include system response quantities such as pressure loss coefficients. A single blade was demonstrated to be representative of the flow in the cascade. The influence of flow periodicity, flow blockage and 3D effects due to boundary layers on the walls were proved to have a negligible influence on the flow quantities studied.

   The expanded simulation uncertainty for the pressure and the Mach number values was on the same order of magnitude as reported in the nozzle test case, which is not viscous and free of shock phenomena. Lowering the contribution of the numerical uncertainty is possible by refining the mesh at some locations, such as the throat. In the absence of experimental data, a comparison with the simulation of the complete 3D domain produced with the state-of-the-art CFD software was performed. The deviation between the 3D domain and the single blade was lower than the expanded simulation uncertainty for the pressure and for the Mach number at the four boundaries considered, indicating that the infrastructure is adequate to assess the cascade case.

6.2. Recommendations for Improvement

The suggestions made are primarily related to the procedure used to validate and to improve the models defined.

- As noticed in the study of the Mach number in the nozzle, the Hills model cannot be used standalone since it only provides a global result. Clear trends, such as a localized increase in the comparison error, should be examined first. The model is best applied in regions with constant error.
- In future simulations with the single blade the choice of the boundaries of the domain should be improved. In particular, the periodic boundary should be matched with the mid-plane of the measuring

passage to have more accurate measures of the Mach number. The outlet boundary should be positioned where the reflected shock wave does not coincide with the wake.

- An alternative to moving the outlet boundary could be the use of empirical corrective factors at the wake-shock wave crossing point to simulate the effect of the reflected shock wave in the single blade.
- The number of measuring stations should be increased where the flow properties of interest are extracted, such as at the wake.
- To study the wake, the location of the measuring station at the blade trailing edge should be refined as it currently does not match the stagnation point. The mesh of the periodic and outlet boundaries should also be improved since the numerical uncertainty was the largest contribution to the total expanded uncertainty.
- The mesh around the throat should be refined, since there, peaks in uncertainty up to 4% of the total pressure are present and the numerical uncertainty make up a large part of the total expanded uncertainty.
- If the use of a denser mesh would make the stochastic simulation too computationally expensive and only the DRQs in the diverging part are of interest, the inlet total pressure should be removed since its influence was demonstrated to be minimal to most response quantities. The inlet total temperature has also a rather limited influence, so it too can be discarded.

6.3. Future Work

This section presents the work to do to continue the validation procedure defined in Fig. 2.9 and to confirm the conclusions of this study.

- When RefProp will be made available in SU2 by means of look-up tables, the cases defined in Sec. 3.3.3 should be executed and compared to the equivalent case using cubic EoS. The effect of the thermodynamic models on the flow quantities along the nozzle length could then be studied. If density, pressure and temperature could be simultaneously measured along the nozzle length, the thermodynamic model could be directly assessed.
- More cases involving shock wave phenomena were envisioned and could be run to further assess the flow solver in the presence of large property gradients.
- The transport and the thermal model should be assessed. To do so the model's parameters such as the viscosity and the thermal conductivity constant could be added to the UQ inputs, so that their influence on the response quantities uncertainty could be studied.
- A tool to extract the shock wave angle from the schlieren pictures should be made to determine the uncertainty of the angle measures.
- Expand the type of response quantities for which the validation is performed. Plans already exist to extract the density along the nozzle midplane with optical systems.
- To continue the validation hierarchy defined, experimental data from the cascade should be gathered and compared to the simulations.
- This thesis focused on direct response quantities from the cascade blade row. An assessment of system response quantities, such as loss coefficients, should also be considered due to their importance in engineering design process. This would allow for optimization study to be performed through simulations.
- Simulations with higher mesh density should be performed for the blade case to determine which numerical scheme better approximate the regions with a large gradient.

A

SU2 configuration Files

In this appendix the two base cases used for the SU2 simulations are presented. For the deterministic simulations the main variation was switching between ROE with MUSCL and JST numerical schemes. The coefficient to be set for ROE is the ENTROPY_FIX_COEFF, which is by default 0.1, and MUSCL_FLOW to YES. For the JST numerical scheme, it is necessary to set the JST_SENSOR_COEFF, which by default are 0.5 and 0.12.

For the UQ, the value of some settings of the base configuration file are substituted by XX[ValueName]XX so that the they can be updated through a Python script depending on the iteration. The values substituted are the inputs with an associated uncertainty, boundary conditions and thermodynamic model parameters, and others, such as the CFL number, which can be varied during the UQ to improve convergence performance.

A.1. SU2 Configuration for the Nozzle Case

```
%%%%%%%%%%%%%%%%%%%%%%%%%%%%%%%%%%%%%%%%%%%%%%%%%%%%%%%%%%%%%%%%%%%%%%%%%%%%%%%%
%                                                                              %
% SU2 configuration file                                                       %
% Case description: Nozzle Euler ORCHID                                        %
% Author: R. Vello                                                             %
% Institution: Delft University of Technology                                  %
% Date: Feb 28th, 2020                                                         %
% File Version 5.0.0 "Raven"                                                   %
%                                                                              %
%%%%%%%%%%%%%%%%%%%%%%%%%%%%%%%%%%%%%%%%%%%%%%%%%%%%%%%%%%%%%%%%%%%%%%%%%%%%%%%%

% ------------- DIRECT, ADJOINT, AND LINEARIZED PROBLEM DEFINITION ------------%
PHYSICAL_PROBLEM= EULER
KIND_TURB_MODEL= NONE
MATH_PROBLEM= DIRECT
RESTART_SOL= YES

% -------------------- COMPRESSIBLE FREE-STREAM DEFINITION --------------------%
MACH_NUMBER= 0.3
AoA= 0.0
FREESTREAM_PRESSURE= 1000000.0
FREESTREAM_TEMPERATURE= 515.85
FREESTREAM_DENSITY= 48.9223
FREESTREAM_TURBULENCEINTENSITY= 0.1
FREESTREAM_TURB2LAMVISCRATIO= 100.0
FREESTREAM_OPTION= TEMPERATURE_FS
INIT_OPTION= TD_CONDITIONS

% ---------------------- REFERENCE VALUE DEFINITION ---------------------------%
REF_DIMENSIONALIZATION= FREESTREAM_PRESS_EQ_ONE

% --------------------------------- FLUID MODEL --------------------------------%
FLUID_MODEL= PR_GAS
GAMMA_VALUE= 1.02605
```

```
GAS_CONSTANT= 51.2
CRITICAL_TEMPERATURE= 518.7
CRITICAL_PRESSURE= 1939000.0
ACENTRIC_FACTOR= 0.419

% ---------------------------- THERMAL CONDUCTIVITY MODEL ----------------------%
CONDUCTIVITY_MODEL= CONSTANT_PRANDTL
KT_CONSTANT= 0.0257

% --------------------- BOUNDARY CONDITION DEFINITION --------------------------%
MARKER_EULER= ( wall1 )
MARKER_SYM= ( wall2 )
MARKER_RIEMANN= ( inflow, TOTAL_CONDITIONS_PT, 1840000.0, 525.15, 1.0, 0.0, 0.0,...
outflow, STATIC_PRESSURE, 210000, 0.0, 0.0, 0.0, 0.0 )
SPATIAL_FOURIER = YES
RAMP_OUTLET_PRESSURE= NO
MARKER_PLOTTING= ( wall1, wall2 )

% ------------- COMMON PARAMETERS DEFINING THE NUMERICAL METHOD ---------------%
NUM_METHOD_GRAD= WEIGHTED_LEAST_SQUARES
CFL_NUMBER= 40.0
CFL_ADAPT= YES
CFL_ADAPT_PARAM= ( 0.3, 0.5, 10.0, 60.0 )

% ------------------------ LINEAR SOLVER DEFINITION ----------------------------%
LINEAR_SOLVER= FGMRES
LINEAR_SOLVER_PREC= LU_SGS
LINEAR_SOLVER_ERROR= 1E-4
LINEAR_SOLVER_ITER= 5

% -------------------------- MULTIGRID PARAMETERS ------------------------------%
MGLEVEL= 0

% ----------------------- SLOPE LIMITER DEFINITION -----------------------------%
VENKAT_LIMITER_COEFF= 0.5

% --------------------- FLOW NUMERICAL METHOD DEFINITION -----------------------%
CONV_NUM_METHOD_FLOW= ROE
MUSCL_FLOW= YES
ENTROPY_FIX_COEFF= 0.1
SLOPE_LIMITER_FLOW= VAN_ALBADA_EDGE
TIME_DISCRE_FLOW= EULER_IMPLICIT
RELAXATION_FACTOR_FLOW= 0.6

% --------------------------- CONVERGENCE PARAMETERS --------------------------%
EXT_ITER= 10000
CONV_CRITERIA= RESIDUAL
RESIDUAL_FUNC_FLOW= RHO
RESIDUAL_REDUCTION= 9999
RESIDUAL_MINVAL= -13
STARTCONV_ITER= 10
CAUCHY_ELEMS= 100
CAUCHY_EPS= 1E-6
CAUCHY_FUNC_FLOW= DRAG

% ------------------------- INPUT/OUTPUT INFORMATION --------------------------%
MESH_FILENAME= su2mesh.su2
MESH_FORMAT= SU2
MESH_OUT_FILENAME= su2mesh_per.su2
SOLUTION_FLOW_FILENAME= restart_flow.dat
OUTPUT_FORMAT= TECPLOT
CONV_FILENAME= history
RESTART_FLOW_FILENAME= restart_flow.dat
VOLUME_FLOW_FILENAME= flow
SURFACE_FLOW_FILENAME= surface_flow
WRT_SOL_FREQ= 100
WRT_CON_FREQ= 1
WRT_RESIDUALS= YES
```

A.2. SU2 Configuration for the Airfoil Case

```
%%%%%%%%%%%%%%%%%%%%%%%%%%%%%%%%%%%%%%%%%%%%%%%%%%%%%%%%%%%%%%%%%%%%%%%%%%%%%%%%
%                                                                              %
% SU2 configuration file                                                       %
% Case description: Airfoil RANS ORCHID                                        %
% Author: R. Vello                                                             %
% Institution: Delft University of Technology                                  %
% Date: Feb 28th, 2020                                                         %
% File Version 5.0.0 "Raven"                                                   %
%                                                                              %
%%%%%%%%%%%%%%%%%%%%%%%%%%%%%%%%%%%%%%%%%%%%%%%%%%%%%%%%%%%%%%%%%%%%%%%%%%%%%%%%

% ------------- DIRECT, ADJOINT, AND LINEARIZED PROBLEM DEFINITION ------------%
PHYSICAL_PROBLEM= RANS
KIND_TURB_MODEL= SA
MATH_PROBLEM= DIRECT
RESTART_SOL= YES

% -------------------- COMPRESSIBLE FREE-STREAM DEFINITION --------------------%
MACH_NUMBER= 0.05
AoA= 0.0
FREESTREAM_PRESSURE= 1840000.0
FREESTREAM_TEMPERATURE= 523
FREESTREAM_DENSITY= 122
FREESTREAM_TURBULENCEINTENSITY = 0.1
FREESTREAM_TURB2LAMVISCRATIO = 100.0
FREESTREAM_OPTION= TEMPERATURE_FS
INIT_OPTION= TD_CONDITIONS

% ---------------------- REFERENCE VALUE DEFINITION ---------------------------%
REF_DIMENSIONALIZATION= DIMENSIONAL

% --------------------------------- FLUID MODEL -------------------------------%
FLUID_MODEL= PR_GAS
GAMMA_VALUE= 1.025
GAS_CONSTANT= 51.2
CRITICAL_TEMPERATURE= 518.75
CRITICAL_PRESSURE= 1939000.0
ACENTRIC_FACTOR= 0.418

% --------------------------- VISCOSITY MODEL ---------------------------------%
VISCOSITY_MODEL= CONSTANT_VISCOSITY
MU_CONSTANT= 1.354E-5
MU_REF= 1.716E-5
MU_T_REF= 273.15
SUTHERLAND_CONSTANT= 110.4

% --------------------------- THERMAL CONDUCTIVITY MODEL ----------------------%
CONDUCTIVITY_MODEL= CONSTANT_PRANDTL
KT_CONSTANT= 0.03547

% -------------------- BOUNDARY CONDITION DEFINITION --------------------------%
MARKER_HEATFLUX= ( wall1, 0.0 )
MARKER_GILES= ( inflow, TOTAL_CONDITIONS_PT, 1840000.0, 525.15, 1.0, 0.0, 0.0,...
1.0, 0.0, outflow, STATIC_PRESSURE, 195000, 0.0, 0.0, 0.0, 0.0, 1.0, 0.0 )
SPATIAL_FOURIER = YES
AVERAGE_PROCESS_KIND= MIXEDOUT
TURBOMACHINERY_KIND= AXIAL
NUM_SPANWISE_SECTIONS= 1
RAMP_OUTLET_PRESSURE= YES
RAMP_OUTLET_PRESSURE_COEFF= (1500000.0, 100.0, 1000)
MARKER_PERIODIC= (periodic1, periodic2, 0.0, 0.0, 0.0, 0.0, 0.0, 0.0, 0.0, 0.045, 0.0)

% ------------------------ SURFACES IDENTIFICATION ----------------------------%
MARKER_PLOTTING= ( wall1, periodic1, outflow )
MARKER_MONITORING= ( wall1, periodic1, outflow )
MARKER_TURBOMACHINERY= ( inflow, outflow )
```

```
% ------------------------- GRID ADAPTATION STRATEGY --------------------------%
KIND_ADAPT= PERIODIC

% ------------- COMMON PARAMETERS DEFINING THE NUMERICAL METHOD ---------------%
NUM_METHOD_GRAD= WEIGHTED_LEAST_SQUARES
CFL_NUMBER= 5.0
CFL_ADAPT= NO

% ------------------------ LINEAR SOLVER DEFINITION ---------------------------%
LINEAR_SOLVER= FGMRES
LINEAR_SOLVER_PREC= LU_SGS
LINEAR_SOLVER_ERROR= 1E-4
LINEAR_SOLVER_ITER= 5

% -------------------------- MULTIGRID PARAMETERS -----------------------------%
MGLEVEL= 0

% ----------------------- SLOPE LIMITER DEFINITION ----------------------------%
VENKAT_LIMITER_COEFF= 0.5

% --------------------- FLOW NUMERICAL METHOD DEFINITION ----------------------%
CONV_NUM_METHOD_FLOW= JST
MUSCL_FLOW= YES
ENTROPY_FIX_COEFF= 0.1
JST_SENSOR_COEFF= ( 0.5, 0.12 )
SLOPE_LIMITER_FLOW= VAN_ALBADA_EDGE
TIME_DISCRE_FLOW= EULER_IMPLICIT
RELAXATION_FACTOR_FLOW= 0.6

% --------------------- TURBULENT NUMERICAL METHOD DEFINITION -----------------%
CONV_NUM_METHOD_TURB= SCALAR_UPWIND
MUSCL_TURB = YES
SLOPE_LIMITER_TURB= VENKATAKRISHNAN
TIME_DISCRE_TURB= EULER_IMPLICIT
CFL_REDUCTION_TURB= 0.01
RELAXATION_FACTOR_TURB= 0.6

% -------------------------- CONVERGENCE PARAMETERS ---------------------------%
EXT_ITER= 200000
CONV_CRITERIA= RESIDUAL
RESIDUAL_FUNC_FLOW= RHO
RESIDUAL_REDUCTION= 9999
RESIDUAL_MINVAL= -6.25
STARTCONV_ITER= 10
CAUCHY_ELEMS= 100
CAUCHY_EPS= 1E-6
CAUCHY_FUNC_FLOW= DRAG

% ------------------------ INPUT/OUTPUT INFORMATION ---------------------------%
MESH_FILENAME= su2mesh_per.su2
MESH_FORMAT= SU2
MESH_OUT_FILENAME= su2mesh_per.su2
SOLUTION_FLOW_FILENAME= restart_flow.dat
OUTPUT_FORMAT= TECPLOT
CONV_FILENAME= history
RESTART_FLOW_FILENAME= restart_flow.dat
VOLUME_FLOW_FILENAME= flow
SURFACE_FLOW_FILENAME= surface_flow
WRT_SOL_FREQ= 100
WRT_CON_FREQ= 10
```

B

Proof of Assumptions

One Dimensional Mass flow

In this section, a comparison of the mass flow rate calculated with the 1D approximation and by integrating the momentum across the domain surface will be done. The 1D approximation is used in throughout the thesis because it is easier to perform, since the integration requires to use dedicated software.

The comparison is done at three locations: inlet, throat and outlet, and three meshes: 2D Euler, 2D RANS and 3D RANS. Figure B.1 shows the x-momentum for the 2D RANS case.

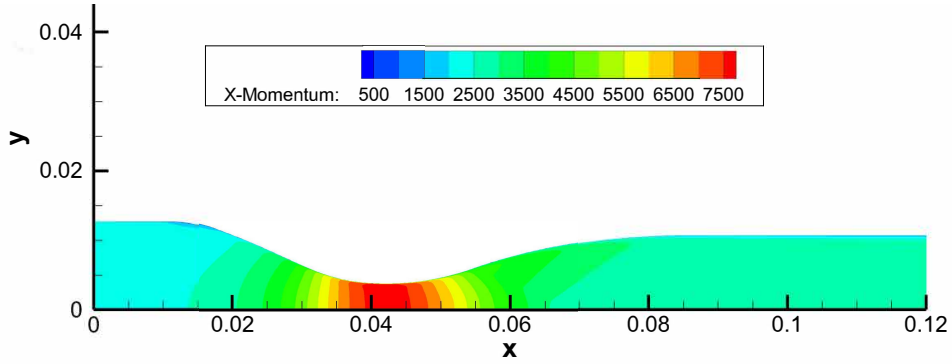

Figure B.1: X-momentum in the ORCHID nozzle for PR25 for the 2D RANS simulation.

Table B.1 shows the mass flow rate values calculated with the different methods. Mass flow 1D uses the centreline momentum values multiplied by the height and width of nozzle. Mass flow integral uses the momentum integrated along the height from tecplot mutiplied by the nozzle width.

Inlet height is 0.0254 m, throat height is 0.0075 m, outlet height is 0.0214 m. Width is 0.02 m.

Method	Inlet	Throat	Outlet
Integral 3D RANS	1.1488 kg/s	1.1492 kg/s	1.1520 kg/s
Integral 2D RANS	1.1523 kg/s	1.1549 kg/s	1.1549 kg/s
Integral 2D Euler	1.1648 kg/s	1.1590 kg/s	1.1589 kg/s
Uniform flow 1D Euler	1.1740 kg/s	1.1651 kg/s	1.1643 kg/s

These values are deterministic and do not have any uncertainty quantified. As expected, due to the presence of the boundary layer, the mass flow rate in the RANS cases is slightly lower. The mass flow rate at the inlet as a larger deviation than at the throat and the outlet. The uncertainty is around 1% between integration of the 3D RANS domain and the 1D method at the throat. In conclusion, the 1D approximation slightly underestimates the flow by roughly 0.02 kg/s, which is negligible in relative terms.

C

Tips for SU2 Simulations

Improved Convergence

In this section, some tips to help the convergence of SU2 simulations are listed.To ensure a quick convergence of 2D RANS case, some parameters should be varied. The two most critical ones identified were the boundary layer thickness and the CFL number. In case the BL was not thick enough, converge would not proceed lower than a certain threshold. This probably happened because in the region close to the outlet the boundary layer grows considerably, so if the thickness is not adequate it would not be possible for the change in velocity to be correctly captured, preventing the residual from decreasing further. The CFL number instead was critical in determining the rate of convergence, an optimal value identified is 20. Convergence was achieved by first turning off the MUSCL_FLOW option to ensure a fully converged 1st order solution, then with the option turned on, the 2nd order solution was calculated by restarting the previous case.

Mesh with Periodic Boundaries

To generate the meshes UMG2 was used. The procedure to do so is here explained. The mesh is generated using the HYMESH.sh script. Since periodic boundaries are present, after running HYMESH it is necessary to run SU2_MSH, which converts the initial mesh to allow it to work with the periodic boundary. Then, after changing the configuration file to use the newly prepared mesh, the normal SU2_CFD command can be used.

D

Procedures and Code Descriptions

D.1. The Jump Conditions

Grossman [30] proposed a series of steps to solve the jump conditions for an oblique shock wave in a non-ideal gas. This procedure require the use of an iterative solver for the following equation

$$\tan\beta = \frac{(1-\nu) \pm \left[(1-\nu)^2 - 4\nu\tan^2\theta\right]^{1/2}}{2\nu\tan\theta}, \tag{D.1}$$

where ν is the density ratio. The solution procedure is as follows:

1. The initial known conditions are V_1, p_1, ρ_1, θ. These allow the calculation of $h_1 = h\left(p_1, \rho_1\right)$.
2. An initial $\nu = \rho_1/\rho_2$ is guessed.
3. The equation can be solver for β, and then $V_{n_1} = V_1 \sin\beta$ can be calculated.
4. Using equations 2.16, 2.17, 2.18 and 2.19, it is possible to find that $V_{n_2} = V_{n_1}\nu$, $p_2 = p_1 + \rho_1 V_{n\,1}^2\left(1-\nu\right)$ and $h_2 = h_1 + \left(V_{n\,1}^2/2\right)\left(1-\nu^2\right)$.
5. Using the equation of state the enthalpy can also be determined as $\tilde{h}_2 = h\left(p_2, \rho_2\right)$
6. If $\tilde{h}_2 = h_2$ is satisfied to a certain tolerance, then the loop has converged. Otherwise a new value of ν is required and it is necessary to restart from step 3.

It is then possible to calculate β, V_{n1}, V_{n2}, p_2, h_2. Finally, $V_2 = V_{n2}/\sin\left(\beta-\theta\right)$.

D.2. Definition of the Boundary Conditions

In this paragraph it is demonstrated that the VR is equivalent to the ratio of density between inlet and outlet. The VR is defined as

$$VR = \frac{\dot{Q}_{\text{out}}}{\dot{Q}_{\text{in}}}. \tag{D.2}$$

Using the conservation of mass equation it is possible to write

$$VR = \frac{\dot{Q}_{\text{out}}}{\dot{Q}_{\text{in}}} = \frac{\dot{m}_{\text{out}} \cdot \rho_{\text{in}}}{\rho_{\text{out}} \cdot \dot{m}_{\text{in}}}, \tag{D.3}$$

and since the mass flow rate does not change between inlet and outlet, VR is the ratio of density

$$VR = \frac{\rho_{\text{in}}}{\rho_{\text{out}}}. \tag{D.4}$$

The boundary conditions of the simulations can then be defined. First, the VR of the nozzle is calculated, then the outlet pressure is calculated starting from the inlet total conditions chosen.

1. For the design condition P_0, T_0 and P_b should be known.
2. From REFPROP it is possible to find s_0 and ρ_0, and so s_b since the process is isentropic.
3. Since the static pressure and the entropy are known, ρ_b can be calculated with REFPROP.
4. Finally, by applying the formula $VR = \frac{\rho_0}{\rho_b}$, the volumetric flow ratio at design condition can be determined.

For the nozzle considered, the VR is equal to 13.57. The procedure devised to determine the outlet pressure from the inlet total conditions is here described.

1. Define an initial pressure P_0 and temperature T_0.
2. Through REFPROP determine the density ρ_0 and the entropy s_0 at the point.
3. Since VR is known, calculate $\rho_b = \rho_0 / VR$.
4. The expansion is isentropic, so $s_b = s_0$.
5. With the entropy and the density, using REFPROP, the static pressure P_1 to set at the outlet can be calculated.

D.3. Description of the Validation Map Code

The code used to generate the validation map is made of two main parts: the data generation and the plotting.

In the first part, a mesh with an arbitrary number of points is generated using as coordinates a combination of temperature and entropy in the case of the $T-s$ diagram. A `for` cycle then call the equations of state to fill the matrix. Two checks are made to avoid calculating data which is not useful, the first one involves a call to RefProp to determine if the point is in the two phase region to skip it. The second one check whether the pressure is above or below a certain threshold, since in the liquid region the temperature increases very slowly with the pressure. After then, the properties of interest are calculated. There are four implemented way to do so, through RefProp 10, RefProp 9, FluidProp and an ad-hoc code by Bahamonde et al. [6]. RefProp uses multiparameter equations of state to provide very accurate data of a certain fluid. The difference between the two versions used is related to their interface to Matlab. RefProp 10 is connected to Matlab through Python, while RefProp 9 can be called directly by having a few files in the same folder where the function is located. FluidProp instead is a collection of thermodynamic models, which also includes RefProp. In this study it is used to call the iPRSV equation through the StanMix library. Finally Bahamonde's code is an implementation in Matlab of the Peng-Robinson EoS with function calls very similar to the other programs. All of these applications need to be set-up for the fluid of interest and the can be called with a command. This requires two thermodynamic properties as input and can provide a chosen third one as the output. A limitation of Bahamonde's code is that it cannot receive the entropy as the input. Various options will be compared to determine the most useful combination.

During the second phase the properties calculated are processed and plotted. For instance, of interest in this case is the relative error of the output property at each point which is defined by using a colour scale.

Bibliography

[1] B. M. Adams, M. S. Eldred, G. Geraci, R.W. Hooper, J. D. Jakeman, K.A. Maupin, Monschke J.A., A.A. Rushdi, J. A. Stephens, L. P. Swiler, T. M. Wildey, W.J. Bohnhoff, K.A. Dalbey, M.S. Ebeida, J.P. Eddy, P.D. Hough, Khalil M., K.T. Hu, E.M. Ridgeway, D.M. Vigil, and J.G. Winokur. Dakota, A Multilevel Parallel Object-Oriented Framework for Design Optimization, Parameter Estimation, Uncertainty Quantification, and Sensitivity Analysis: Version 6.10 User's Manual. Technical Report SAND2014-4633, Sandia National Laboratories, 2019. URL `http://dakota.sandia.gov`.

[2] American Institute of Aeronautics and Astronautics (AIAA). Guide for the Verification and Validation of Computational Fluid Dynamics Simulations. *Guide* G-077-1998, AIAA, 1998.

[3] Nitish Anand, Salvatore Vitale, Matteo Pini, Gustavo J Otero, and Rene Pecnik. Design methodology for supersonic radial vanes operating in nonideal flow conditions. *Journal of Engineering for Gas Turbines and Power*, 141(2), 2019.

[4] John David Anderson Jr. *Fundamentals of aerodynamics*. Tata McGraw-Hill Education, 2010.

[5] ASME. Standard for Verification and Validation in Computational Fluid Dynamics and Heat Transfer. *Standard* V&V20-2009, ASME, 2009.

[6] Sebastian Bahamonde, Matteo Pini, Carlo De Servi, Antonio Rubino, and Piero Colonna. Method for the preliminary fluid dynamic design of high-temperature mini-organic rankine cycle turbines. *Journal of Engineering for Gas Turbines and Power*, 139(8), 2017.

[7] F. Beltrame. Accuracy assessment of the su2 flow solver for non-ideal organic vapor supersonic expansions using experimental data. Master's thesis, Politecnico di Torino, 2020.

[8] Kenneth Edwin Bett, John Shipley Rowlinson, and Graham Saville. *Thermodynamics for chemical engineers*. Mit Press, 1975.

[9] L.J. Bills. Validation of the su2 flow solver for classical non ideal compressible fluid dynamics. Master's thesis, Delft University of Technology, 2020.

[10] Yunus A Cengel and Michael A Boles. *Thermodynamics: An Engineering Approach 6th Editon (SI Units)*. The McGraw-Hill Companies, Inc., New York, 2007.

[11] T. H. Chung, M. Ajlan, L. L. Lee, and K. E. Starling. Generalized multiparameter correlation for nonpolar and polar fluid transport properties. *Industrial & Engineering Chemistry Fundamentals*, 1988.

[12] Ting Horng Chung, Lloyd L Lee, and Kenneth E Starling. Applications of kinetic gas theories and multiparameter correlation for prediction of dilute gas viscosity and thermal conductivity. *Industrial & engineering chemistry fundamentals*, 23(1):8–13, 1984.

[13] P. Cinnella, P.M. Congedo, L. Parussini, and V. Pediroda. Quantification of uncertainties in compressible flows with complex thermodynamic behavior. In *Proceedings of 19th AIAA Computational Fluid Dynamics*, San Antonio, Texas, June 22-25 2009. AIAA.

[14] P. Cinnella, P.M. Congedo, V. Pediroda, and L. Parussini. Sensitivity analysis of dense gas flow simulations to thermodynamic uncertainties. *Physics of Fluids*, 23, 2011.

[15] H.W. Coleman and W.G. Steele. *Experimentation and Uncertainty Analysis for Engineers*. Wiley, 1989. ISBN 9780471635178. URL `https://books.google.nl/books?id=H25RAAAAMAAJ`.

[16] P. Colonna, N. R. Nannan, A. Guardone, and E. W. Lemmon. Multiparameter equations of state for selected siloxanes. *Fluid Phase Equilibria*, 244(2):193–211, 2006.

[17] Piero Colonna, TP Van der Stelt, and A Guardone. Fluidprop: a program for the estimation of thermo physical properties of fluids. *Energy Technology Section, Delft University of Technology, The Netherlands*, 2004.

[18] Piero Colonna, Emiliano Casati, Carsten Trapp, Tiemo Mathijssen, Jaakko Larjola, Teemu Turunen-Saaresti, and Antti Uusitalo. Organic rankine cycle power systems: From the concept to current technology, applications, and an outlook to the future. *Journal of Engineering for Gas Turbines and Power*, 137(10):100801–100801–19, October 2015. ISSN 0742-4795. doi: 10.1115/1.4029884. URL `http://dx.doi.org/10.1115/1.4029884`.

[19] P. M. Congedo. *Contributions to the reliability of numerical simulations in fluid mechanics. Application to the flow simulation of thermodynamically complex gases*. PhD thesis, University of Bordeaux, 2013.

[20] Carlo M De Servi, Matteo Burigana, Matteo Pini, and Piero Colonna. Design method and performance prediction for radial-inflow turbines of high-temperature mini-organic rankine cycle power systems. *Journal of Engineering for Gas Turbines and Power*, 141(9), 2019.

[21] J Do Denton. *Loss mechanisms in turbomachines*, volume 78897. American Society of Mechanical Engineers, 1993.

[22] J. Dunham. CFD Validation for Propulsion System Components. Technical Report AR-355, AGARD, 1998.

[23] L Eça and M Hoekstra. On the influence of the iterative error in the numerical uncertainty of ship viscous flow calculations. In *26th Symposium on Naval Hydrodynamics*, volume 2006, pages 17–22, 2006.

[24] L Eça and M Hoekstra. Evaluation of numerical error estimation based on grid refinement studies with the method of the manufactured solutions. *Computers & Fluids*, 38(8):1580–1591, 2009.

[25] Luis Eça and Martin Hoekstra. A procedure for the estimation of the numerical uncertainty of cfd calculations based on grid refinement studies. *Journal of Computational Physics*, 262:104–130, 2014.

[26] T. D. Economon, F. Palacios, S. R. Copeland, T. W. Lukaczyk, and J. J. Alonso. SU2: An open-source suite for multiphysics simulation and design. *AIAA Journal*, 54(3):828–846, December 2015.

[27] Michael Giles. *Non-reflecting boundary conditions for the Euler equations*. Computational Fluid Dynamics Laboratory, Department of Aeronautics and . . . , 1988.

[28] G. Gori, M. Zocca, G. Cammi, A. Spinelli, and A. Guardone. Experimental assessment of the open-source su2 cfd suite for orc applications. *Energy Procedia*, 129:256 – 263, 2017. 4th International Seminar on ORC Power Systems September 13-15th 2017.

[29] G. Gori, M. Zocca, G. Cammi, A. Spinelli, P. M. Congedo, and A. Guardone. Accuracy assessment of the non-ideal computational fluid dynamics model for siloxane MDM from the open-source SU2 suite. *European Journal of Mechanics - B/Fluids*, 79:109–120, January 2020. ISSN 0997-7546.

[30] B Grossman. Fundamental concepts of real gasdynamics. In *Technical Report*. Virginia Polytechnic Institute and State University, 2000.

[31] Gayathri Hariharan. Design of experiments and schlieren imaging of non-ideal compressible flows. Master's thesis, Delft University of Technology, 2021.

[32] A. Head, C. De Servi, E. Casati, M. Pini, and P. Colonna. Preliminary design of the ORCHID: A facility for studying non-ideal compressible fluid dynamics and testing ORC expanders. In *ASME Turbo Expo*, volume GT-2016, page 14, 2016.

[33] A. J. Head, S. Iyer, C. de Servi, and M. Pini. Towards the validation of a CFD solver for non-ideal compressible flows. *Energy Procedia*, 129(Supplement C):240 – 247, 2017. ISSN 1876-6102. 4th International Seminar on ORC Power Systems September 13-15th 2017. Pg.

[34] AJ Head. *Novel Experiments for the Investigation of Non-Ideal Compressible Fluid Dynamics: The ORCHID and First Results of Optical Measurements*. PhD thesis, Delft University of Technology, 2021.

[35] Richard G Hills. Model validation: model parameter and measurement uncertainty. *Journal of Heat Transfer*, 2006.

[36] Charles Hirsch. Advanced methods for cascade testing. *NASA STI/Recon Technical Report N*, 94:15119, 1993.

[37] Toshimitsu Homma and Andrea Saltelli. Importance measures in global sensitivity analysis of nonlinear models. *Reliability Engineering & System Safety*, 52(1):1–17, 1996.

[38] S. Iyer. Influence of thermodynamic property perturbations on nozzle design and non-ideal compressible flow phenomena. Master's thesis, Delft University of Technology, 2015.

[39] Antony Jameson, Wolfgang Schmidt, and Eli Turkel. Numerical solution of the euler equations by finite volume methods using runge kutta time stepping schemes. In *14th fluid and plasma dynamics conference*, page 1259, 1981.

[40] Rens Liebrand. Tip vortex modelling for cavitation noise applications: A verification and validation study in refresco. Master's thesis, Delft University of Technology, 2019.

[41] W Sutherland LII. The viscosity of gases and molecular force. *Lond. Edinb. Dublin Philos. Mag. J. Sci*, 36: 507–531, 1893.

[42] WF Luder. Ideal gas definition. *Journal of Chemical Education*, 45(5):351, 1968.

[43] MARIN. Refresco V&V tools, 2019. URL `https://www.refresco.org/verification-validation/utilitiesvv-tools/`.

[44] Dominika Matuszewska. Molecular complexity of working fluids dedicated to organic rankine cycle (orc). In *IOP Conference Series: Materials Science and Engineering*, volume 946, page 012008. IOP Publishing, 2020.

[45] Unmeel B Mehta, Dean R Eklund, Vicente J Romero, Jeffrey A Pearce, and Nicholas S Keim. Simulation credibility: Advances in verification, validation, and uncertainty quantification. *NTRS - NASA Technical Reports Server*, 2016.

[46] Florian R Menter. Two-equation eddy-viscosity turbulence models for engineering applications. *AIAA journal*, 32(8):1598–1605, 1994.

[47] F. Montomoli, M. Massini, S. Salvadori, M. Carnevale, and R. Ahlfeld. *Uncertainty Quantification in Computational Fluid Dynamics and Aircraft Engines*. Springer International Publishing AG, second edition, 2019.

[48] Leonid Moroz, Yuri Govoruschenko, and Petr Pagur. Axial turbine stage design: 1d/2d/3d simulation, experiment, optimization—design of single stage test air turbine models and validation of 1d/2d/3d aerodynamic computation results against test data. In *Turbo Expo: Power for Land, Sea, and Air*, volume 47306, pages 1137–1146, 2005.

[49] Joint Army Navy NASA and Air Force (JANNAF). Joint army navy nasa and air force database, 2014. URL `https://www.jannaf.org/products/databases`.

[50] Pim Nederstigt. Real gas thermodynamics: and the isentropic behavior of substances. Master's thesis, Delft University of Technology, 2017.

[51] W. L. Oberkampf and T. G. Trucano. Verification and Validation in Computational Fluid Dynamics. *Prog. in Aerosp. Sciences*, 38(3):209–272, 2002.

[52] Ding-yu Peng and Donald Robinson. New two-constant equation of state. *Industrial & Engineering Chemistry Fundamentals*, 15, 02 1976. doi: 10.1021/i160057a011.

[53] M. Pini, S. Vitale, P. Colonna, G. Gori, A. Guardone, T. Economon, J.J. Alonso, and F. Palacios. Su2: the open-source software for non-ideal compressible flows. *Journal of Physics: Conference Series*, 821, 2017.

[54] Kenneth S Pitzer, David Z Lippmann, RF Curl Jr, Charles M Huggins, and Donald E Petersen. The volumetric and thermodynamic properties of fluids. ii. compressibility factor, vapor pressure and entropy of vaporization. *Journal of the American Chemical Society*, 77(13):3433–3440, 1955.

[55] Bruce E Poling, John M Prausnitz, John P O'connell, et al. *The properties of gases and liquids*, volume 5. Mcgraw-hill New York, 2001.

[56] George Qian and Adam Mahdi. Sensitivity analysis methods in the biomedical sciences. *Mathematical biosciences*, 323:108306, 2020.

[57] Joachim Rix, Stefan Haas, and José Teixeira. *Virtual Prototyping - Virtual environments and the product design process*. Springer US, 1995. ISBN 9788578110796.

[58] Patrick J Roache. *Verification and validation in computational science and engineering*, volume 895. Hermosa Albuquerque, NM, 1998.

[59] Philip L Roe. Approximate riemann solvers, parameter vectors, and difference schemes. *Journal of computational physics*, 43(2):357–372, 1981.

[60] Vicente J Romero. The real-space model validation approach as a unifying? extended hybrid of the asme vv10 and vv20 approaches. Technical report, Sandia National Lab.(SNL-NM), Albuquerque, NM (United States), 2015.

[61] Clarence W Rowley, Tim Colonius, and Richard M Murray. Model reduction for compressible flows using pod and galerkin projection. *Physica D: Nonlinear Phenomena*, 189(1-2):115–129, 2004.

[62] RL Rowley, WV Wilding, JL Oscarson, Y Yang, NA Zundel, TE Daubert, and RP Danner. Dippr data compilation of pure chemical properties design institute for physical properties. *Provo, UT: Brigham Young University*, 2006.

[63] S.L. Seager and M.R. Slabaugh. *Chemistry for today: General, organic, and biochemistry*. Cengage Learning, 2013.

[64] John W Slater, Julianne C Dudek, and Kenneth E Tatum. The nparc alliance verification and validation archive. *Proceedings of ASME FEDSM00*, 2000.

[65] Ilya M Sobol. Global sensitivity indices for nonlinear mathematical models and their monte carlo estimates. *Mathematics and computers in simulation*, 55(1-3):271–280, 2001.

[66] R. Span. *Multiparameter Equations of State: An Accurate Source of Thermodynamic Property Data*. Engineering online library. Springer, 2000. ISBN 9783540673118. URL `https://books.google.nl/books?id=dd410GGw8wUC`.

[67] R Span and W Wagner. Equations of state for technical applications. i. simultaneously optimized functional forms for nonpolar and polar fluids. *International journal of thermophysics*, 24(1):1–39, 2003.

[68] Andrea Spinelli, Vincenzo Dossena, Paolo Gaetani, Carlo Osnaghi, and D Colombo. Design of a test rig for organic vapours. In *Turbo Expo: Power for Land, Sea, and Air*, volume 44007, pages 109–120, 2010.

[69] Andrea Spinelli, Fabio Cozzi, Vincenzo Dossena, Paolo Gaetani, Marta Zocca, and Alberto Guardone. Experimental investigation of a non-ideal expansion flow of siloxane vapor mdm. In *Turbo Expo: Power for Land, Sea, and Air*, volume 49743, page V003T25A010. American Society of Mechanical Engineers, 2016.

[70] Andrea Spinelli, Fabio Cozzi, Giorgia Cammi, MARTA Zocca, Paolo Gaetani, Vincenzo Dossena, and ALBERTO Guardone. Preliminary characterization of an expanding flow of siloxane vapor mdm. In *J Physics: Conference Series*, volume 821, page 012022, 2017.

[71] Andrea Spinelli, Giorgia Cammi, Camilla Cecilia Conti, Simone Gallarini, Marta Zocca, Fabio Cozzi, Paolo Gaetani, Vincenzo Dossena, and Alberto Guardone. Experimental observation and thermodynamic modeling of non-ideal expanding flows of siloxane mdm vapor for orc applications. *Energy*, 168: 285–294, 2019.

[72] Roman Stryjek and Juan Vera. Prsv - an improved peng-robinson equation of state for pure compounds and mixtures. *The Canadian Journal of Chemical Engineering*, 64:323 – 333, 04 1986.

[73] Monika Thol, Frithjof H Dubberke, Gabor Rutkai, Thorsten Windmann, Andreas Köster, Roland Span, and Jadran Vrabec. Fundamental equation of state correlation for hexamethyldisiloxane based on experimental and molecular simulation data. *Fluid Phase Equilibria*, 418:133–151, 2016.

[74] Philip A Thompson. A fundamental derivative in gasdynamics. *The Physics of Fluids*, 14(9):1843–1849, 1971.

[75] Francesco Tosto, Claudio Lettieri, Matteo Pini, and Piero Colonna. 1d modelling of some paradigmatic non-ideal compressible flows. In *5th International Seminar on ORC Power Systems*, 2019.

[76] T.P van der Stelt, N. R Nannan, and P Colonna. The iPRSV equation of state. *Fluid Phase Equilib.*, 330: 24–35, 2012.

[77] Bram Van Leer. Towards the ultimate conservative difference scheme. v. a second-order sequel to godunov's method. *Journal of computational Physics*, 32(1):101–136, 1979.

[78] S. Vitale, T. A. Albring, M. Pini, N. R. Gauger, and Colonna P. Fully turbulent discrete adjoint solver for non-ideal compressible flow applications. *J. Glob. Power Propuls. Soc.*, 1:252–270, 2017.